Enhanced Bilateral Teleoperation using Generalized Force/Position Mapping

ENHANCED BILATERAL TELEOPERATION USING GENERALIZED FORCE/POSITION MAPPING

BY

PAWEL MALYSZ, B.Eng.

A THESIS

SUBMITTED TO THE DEPARTMENT OF ELECTRICAL & COMPUTER ENGINEERING

AND THE SCHOOL OF GRADUATE STUDIES

OF MCMASTER UNIVERSITY

IN PARTIAL FULFILMENT OF THE REQUIREMENTS

FOR THE DEGREE OF

MASTER OF APPLIED SCIENCE

Master of Applied Science (2007) McMaster University

(Electrical & Computer Engineering) Hamilton, Ontario, Canada

TITLE: Enhanced Bilateral Teleoperation using Generalized Force/Position Mapping

AUTHOR: Pawel Malysz

B.Eng., (Engineering Physics)

McMaster University, Hamilton, Ontario, Canada

SUPERVISOR: Dr. Shahin Sirouspour

NUMBER OF PAGES: xiv, 144

To my family and Araksi

Abstract

The performance index in teleoperation, transparency, is often defined as linear scaling of force and position between the master/operator and slave/environment. Motivated by applications involving soft tissue manipulation such as robotic surgery, the transparency objective is generalized in this thesis to include static nonlinear and linear-time-invariant filter mappings between the master/slave position and force signals. Lyapunov-based adaptive motion/force controllers are proposed to achieve the generalized transparency objectives. Using Lyapunov stability theory the mapped position and force tracking errors are shown to converge in the presence of dynamic uncertainty in the master/slave robots and user/environment dynamics. Given a priori known bounds on unknown dynamic parameters, a framework for robust stability analysis is proposed that uses stability of Lur'e-Postinkov systems and Nyquist/Bode envelopes of interval plant systems. Methods for finding the required Nyquist/Bode envelopes are presented in this thesis.

A comprehensive stability analysis is performed under different sets of generalized mappings. For nonlinear mapping of either position or force, robust stability depends on stability of an equivalent Lur'e-Postinikov system. Stability results of such systems are discussed in this thesis. In particular, the on and off-axis circle theorems are utilized. Using these theorems, sufficient teleoperation stability

regions are obtained that are far less conservative than those obtained from passivity. In the special case of LTI filtered force and position mappings the exact robust stability regions are obtained by showing stability of the relevant closed-loop characteristic polynomial. The proposed robust stability test uses the phase values of a limited set of extremal polynomials.

To demonstrate the utility of the generalized performance measures, a stiffness discrimination tele-manipulation task is considered in which the user compares and contrasts the stiffness of soft environments via haptic exploration in the presence and absence of visual feedback. Using adaptive psychophysical perception experiments a nonlinear force mapping is shown to enhance stiffness discrimination thresholds. The design guidelines for this enhanced nonlinear force mapping are reported in this thesis. Generalized nonlinear and linear filtered mappings are achieved in experiments with a two-axis teleoperation system where the details of implementation are given.

Acknowledgements

My thanks and appreciation to my supervisor, Dr. Shahin Sirouspour, for his guidance, support and encouragement throughout my graduate program here at McMaster.

Sincere gratitude to my fellow colleagues in the Haptics, Telerobotics and Computational Vision Lab, Ali Shahdi, Mahyar Fotoohi, Mike Kinsner, Ivy Zhong, Insu Park, Brian Moody, Sina Niakosari, Bassma Ghali, Saba Moghimi, Ramin Mafi and Amin Abdossalami for making this a fun and enjoyable place to study as well as for their help in my research.

Special thanks to my family since they have made it possible for me to excel in my academic studies with their endless love and support throughout my life. My deepest love to Araksi, for her unwavering love, patience and support makes me feel anything is possible.

Contents

List of Figures

Chapter 1

Introduction

1.1 Motivation

Teleoperation allows one to extend his/her manipulation skills and intelligence to different environments through coordinated control of two robotic arms. With the aid of a master robotic arm, the user can control a slave manipulator to remotely perform a task. Fidelity of a teleoperation control system is often measured by its transparency, i.e. how closely it resembles direct interaction with the environment [6]. Applications of teleoperation systems are numerous ranging from space and deep-water explorations, handling of nuclear and hazardous materials, to robot-assisted surgery/telesurgery [7].

Increased interest in teleoperation-based robotic-assisted surgery has emerged since it can grant the surgeon super-human capabilities such as increased precision and/or enhanced sensitivity through haptic feedback and force/position mapping. Through the use of a surgical robot teleoperation gives the surgeon the possibility of overcoming some the physical limitations that are present in

conventional surgeries. For example it can grant the surgeon access to hard to reach locations and the use of robotics offers a degree of repeatability and precision that is far superior to direct hand manipulation. Among its other benefits are reduced patient trauma due to minimal invasiveness, and the possibility of performing remote surgery [8]. Current commercial robotic surgical systems lack haptic feedback hence surgeons using such systems rely heavily upon visual feedback [8]. This causes surgeon fatigue due to overloading of the visual sensory system and can also lead to unwanted tissue damage caused by application of excessive forces. Incorporating haptics into such robotic surgerical systems seeks to remedy such problems. Furthermore, the ability to reshape the surgeon's perception of the tissue in robotic surgery, gained through the introduction of a controllable interface between the surgeon and patient, has spurred increased research into soft-environment teleoperation [35, 36]. In particular, methods of distorting haptic feedback to increase human sensitivity and perceptual ability are being sought to improve the outcome of surgical procedures. This requires new task-specific design performance criteria to replace the conventional transparency measures. Also, new teleoperation controllers must be developed to achieve these performance objectives.

A teleoperation system consists of five basic elements which are shown in Fig. 1.1. The operator is typically a human being who uses his/her hands to manipulate a master device to control a slave robot which interacts with a remote environment. The master and slave elements include the controllers for each device. For a haptic enabled teleoperation system both visual and haptic feedback are presented to the human operator. Therefore flow of positions/velocities and forces occurs

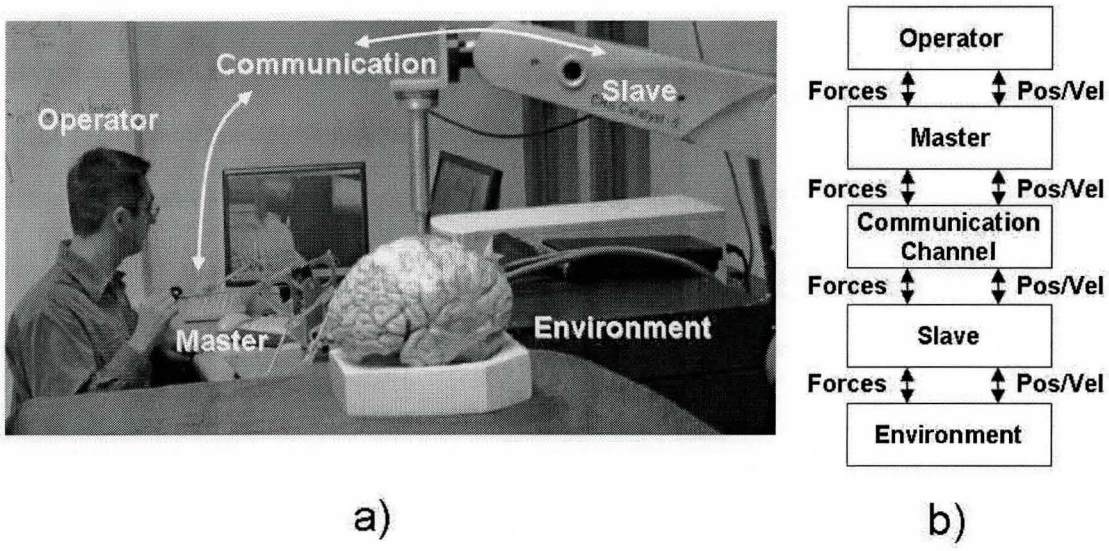

Figure 1.1: Teleoperation systems. a) Example system at McMaster University b) Basic system elements.

throughout the teleoperation system. This bidirectional flow results in a bilateral teleoperation system as opposed to a unilateral teleoperation system where communication between master and slave robots occurs in only one direction. The communication between the two robotic devices can be through optical/electrical cabling or even electromagnetic waves. The traditional goal in teleoperation is to give the human operator a sense of telepresence by making the system transparent. Conventionally this means that the master robot position and slave robot position track each other and that the forces the operator experiences are the same as the interaction forces with the remote environment. This transparency goal often conflicts with the robust stability constraint imposed on the controllers of the system. This is caused by dynamic uncertainty in the master/slave robots, uncertainty in operator/environement dynamics and time delay in the communication channel.

1.2 Problem Statement and Thesis Contributions

- **Problem 1**

  The traditional goal in teleoperation is to enforce linear mappings of force and position such that the master positions (x_m) and hand forces (F_h) correspond linearly to the slave positions (x_s) and environment forces (F_e), i.e.

$$x_m \leftrightarrow k_p x_s$$

$$F_h \leftrightarrow k_f F_e$$

  where k_f and k_p are constant gains. Such an approach does not utilize the full potential of a teleoperation system since the controllers can be designed to enforce more general transparency objectives. Furthermore the benefits of general transparency objectives must also be discussed and demonstrated.

- **Problem 2**

  Teleoperation controllers to solve Problem 1 must be designed to enforce more general transparency objectives. This design must also be robustly stable in the presence of unknown model parameters of the robots as well as unknown operator and environment dynamics.

The following solutions are proposed in this thesis to solve the stated problems.

- **Solution to Problem 1**

  A new more flexible transparency objective is proposed that has the potential to enhance perception/performance in a teleoperation task. This generalized

transparency objective would have ideal position and force mapping taking the following form.

$$H'_{xm}x_m = H'_{xs}k_p(x_s)$$
$$H_{fh}F_h - k_f(H_{fe}F_e) = H_{Zt}x_m$$

where $k_f(\cdot)$, $k_p(\cdot)$ are static non-linear functions, H'_{xm}, H'_{xs}, H_{fe} and H_{fh} are filters that can be represented as LTI transfer functions and H_{Zt} a virtual tool represented as a LTI transfer function that can be chosen to satisfy the performance/stability trade-off in the control design.

Assuming Weber's Law for force and stiffness discrimination, a non-linear force mapping can be used to enhance stiffness discrimination thresholds. The enhanced nonlinear force mapping design seeks to transmit greater relative differences in force toward the operator on the master side than are present at the environment on the slave side. Psychophysics experiments that find the discrimination threshold at a chosen performance level are performed to validate the effectiveness of the non-linear force mapping design. The proposed generalized transparency objective, non-linear enhanced force mapping design and corresponding psychophysics experiments are all contributions of this thesis.

- **Solution to Problem 2**

Lyapunov-based adaptive controllers to enforce the generalized transparency objectives are proposed. These controllers are based on ones found in literature where they have been substantially modified to enforce the proposed

generalized transparency objectives. Utilizing adaptive controllers can mitigate the transparency/stability trade-off by adapting for unknown dynamic parameters and linearizing the system dynamics. To deal with unwanted parameter drift that comes with adaptation the adaptive parameters can be bounded to ranges that can be chosen using a priori knowledge of the teleoperation robots and application. Lyapunov stability theory is used to show convergence of local position, velocity and force tracking errors. The controllers are developed in two stages, the first stage contains the local adaptive controllers and the second stage designs bilateral coordinating terms to facilitate teleoperation. The proposed teleoperation controllers are discussed in detail in Chapter 3.

The environment and operator dynamics can be assumed to be modeled as mass-spring-damper systems with parametric uncertainty. In this context a comprehensive teleoperation robust stability analysis is performed using different sets of generalized mappings. Assuming interval ranges on the parametric uncertainty sufficient robust stability regions are obtained using interval plant systems and stability of Lur'e-Postinikov problems. This is done by using Nyquist/Bode envelopes of interval plant systems in combination with passivity and the on/off axis circle theorems. For the special case of LTI filter mappings of position and force the exact robust stability regions are obtained. The necessary and sufficient stability test for this special case is obtained by analyzing the roots of the relevant closed-loop characteristic equation. The proposed controller and the robust teleoperation stability proof and analysis are all contributions of this thesis.

1.3 Organization of the Thesis

The rest of this thesis is organized as follows. Relevant literature pertaining to teleoperation, soft-tissue telemanipulation and haptic perception is presented in Chapter 2. The adaptive controllers that enforce the new generalized transparency objectives are shown in Chapter 3. Chapters 4 and 5 discuss Interval plant systems and stability of Lur'e-Postnikov systems where the theories presented are used in Chapter 6 to analyze teleoperation stability. Psychophysics perception experiments and enhanced mapping design are covered in Chapter 7. The results of teleoperation experiments using the proposed adaptive controllers on a two-axis system are provided in Chapter 8. The thesis is concluded in Chapter 9.

1.4 Related Publications

- P. Malysz and S. Sirouspour, "Stable Non-linear Force/Position Mapping for Enhanced Telemanipulation of Soft-Environments," in Proc. IEEE Int. Conf. on Robotics and Automation, April 2007, Roma, Italy, pp. 4307-4312.

- P. Malysz and S. Sirouspour, "Control Design and Experiments for Enhanced Detection of Stiffness Variation in Soft Tissue Telemanipulation," Accepted: IEEE Int. Conf. on Intelligent Robots and Systems , Oct 2007, San Diego, CA, USA.

- P. Malysz and S. Sirouspour, "Generalized Force/Position Mappings in Bilateral Teleoperation with Application to Enhanced Stiffness Discrimination," Submitted to: The IEEE Transactions on Robotics.

Chapter 2

Literature Review

This chapter is divided into three sections. The first section introduces the popular two-port network model of teleoperation and some of the various teleoperation control approaches that can be employed. These range from simple two-channel or four-channel fixed controllers to adaptive controllers that handle parametric uncertainty. The second section of this chapter deals with one application of teleoperation, that being telerobotic-surgery. Specifically relevant work related to soft-tissue telemanipulation is presented. The final section focuses on haptic pecerption that is applicable to force-feedback devices used in haptic-enabled teleoperation systems.

2.1 Teleoperation

2.1.1 Two-port Network Model

Early analysis approaches to teleoperation used two-port network models like the one shown in Fig. 2.1, where the environment/human operator are modeled as Thevenin equivalent loads that have a mechanical impedance and exogenous force source. The two-port network would represent the master/slave devices, the communication channel and the controllers. In such a representation forces and velocities could be chosen to be analogous to voltage and current in the circuit-like representation. Early works such as those by Hannaford used such a scheme and assuming linearity proposed that a hybrid matrix representation in (2.1) is suited for teleoperation analysis [9]. The transmitted impedance given in (2.2) is represented in terms of the hybrid matrix parameters [1, 10]. Admittance, impedance and inverse hybrid matrices are also possible [1].

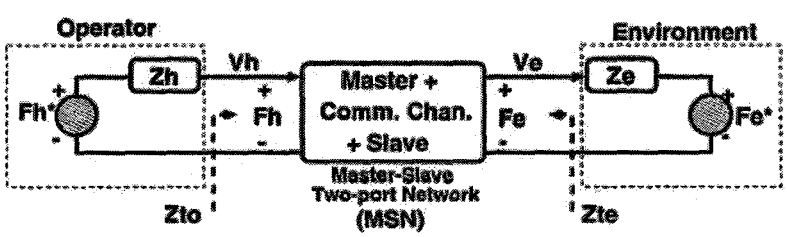

Figure 2.1: Teleoperation two port network model. Figure from [1].

$$\begin{bmatrix} F_h \\ -V_e \end{bmatrix} = \begin{bmatrix} h_{11} & h_{12} \\ h_{21} & h_{22} \end{bmatrix} \begin{bmatrix} V_h \\ F_e \end{bmatrix} \tag{2.1}$$

$$Z_{to} = \frac{h_{11} + (h_{11}h_{22} - h_{12}h_{21})Z_e}{1 + h_{22}Z_e} \tag{2.2}$$

Typical applications of teleoperation involve interaction with an environment where $F_e^* = 0$ in Fig. 2.1. Assuming this Lawrence suggested transparency is achieved when the transmitted impedance Z_{to} felt on the master side is equal to the environment impedance Z_e [10]. An ideal transparent response would correspond to (2.3) and (2.4). This is equivalent to requiring (2.4) with force tracking (2.5). This ideal transparency is achieved with the ideal hybrid matrix (2.6). This formulation is based on a velocity-force representation; a position-force representation would require position tracking instead of (2.4) and ideal transparency still results in (2.6).

$$Z_{to} = Z_e \tag{2.3}$$

$$V_h = V_e \tag{2.4}$$

$$F_h = F_e \tag{2.5}$$

$$\mathcal{H}_{ideal} = \begin{bmatrix} 0 & 1 \\ -1 & 0 \end{bmatrix} \tag{2.6}$$

A teleoperation block diagram in Fig. 2.2 can be formed by assuming the master device (Z_m), slave device (Z_s) and control parameters ($C_s, C_m, C_1, .., C_6$) can be represented as LTI mechanical impedances or transfer functions [1]. Furthermore the control actions are the forces F_{cm} and F_{cs} on the master and slave robots respectively, e^{-sTd} is channel delay of T_d seconds and $F_e^* = 0$ in the environment is utilized. Other block diagrams are possible by using admittances and assuming velocity is the control action on either the master or slave subsystems. These other representations are described in [1]. It is also possible to use position instead of velocity in the two-port network model and teleoperation block diagram

by appropriately modifying the LTI impedances and transfer functions. An advantage of using velocity is that for mass-spring-damper mechanical systems a velocity representation transforms directly to a capacitor-resistor-inductor electric network. The linear systems discussed here can be realized through the application of an appropriate linearizing controller on the non-linear robot dynamics.

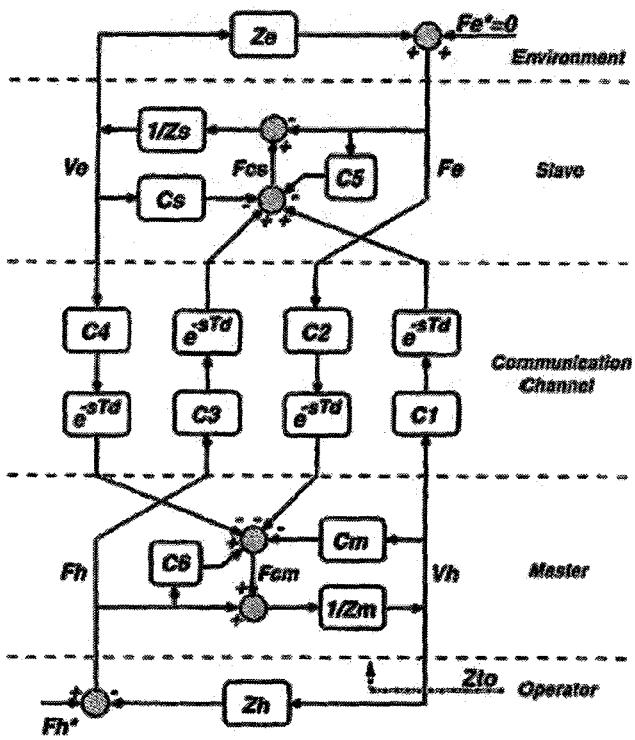

Figure 2.2: Teleoperation block diagram. Figure from [1].

By choosing which channels to use for the control forces, the hybrid matrix (2.1) can be found in terms of the control and dynamic parameters of the system. The performance measures would be based on (2.1) and (2.2) where (2.3)-(2.6) is desired. Teleoperation stability would reduce to closed-loop stability of Fig. 2.2

2.1.2 Teleoperation Control Approaches

A literature search reveals many possible control architectures to facilitate teleoperation. Two-channel approaches can be obtained by only using two of the four communication channels ($C_1, .., C_4$) shown in Fig. 2.2. A simple architecture that requires no force sensing is position-position control [11], where in reference to Fig. 2.2 $C_2 = C_3 = C_5 = C_6 = 0$ and position replaces velocity. Such an approach can in effect couple the end-effectors of the master and slave robots with a virtual spring-damper by using PD control where the master and slave controllers have the same gains. Fidelity and transparency is poor especially in contact with stiff environments and in the presence of communication time delays, however it is simple to apply and has good robust stability. A velocity-velocity approach, where master/slave velocities are matched, has an additional drawback of position drift errors. To improve fidelity the use of force sensors can better reflect the mechanical impedances in teleoperation. A force-force [12] architecture would only utilize the two force measurements however it also suffers from position drift errors. When only one force sensor is present a position-force [13] architecture can be used where the force sensor should be placed on the slave robot. For superior transparency and haptic fidelity all four communication channels should be utilized [10, 14]. Even when using a multi-channel approach, ideal transparency still relies on accurate acceleration measurement and good master/slave model knowledge to cancel out the dynamics of the master/slave robots. Acceleration type measurements can be obtained from force sensors and good model knowledge. However, sensitivity to modeling errors can easily result in negative mass/damping and instability as a result of eliminating the robot dynamics. Also, small zero-order-hold delays in

discrete-time implementation can lead to instability.

Yokokohjii and Yoshikawa discuss transparency in terms of the teleoperation system being able to act as a virtual tool between the operator and environment, where an ideal tool would have no mass, stiffness or damping [14]. Even with acceleration measurements a small amount of modeling error could give the virtual tool negative mass [14], hence Yokokohjii and Yoshikawa propose the virtual tool have some mechanical impedance to stabilize the system. Their transparency objectives are then generalized to (2.7) and position tracking (2.8) where m_t, b_t and k_t are the tool parameters.

$$F_h - F_e = m_t\ddot{x} + b_t\dot{x} + k_t x \tag{2.7}$$

$$x_s = x_m = x \tag{2.8}$$

To achieve robust stability in the presence of dynamic uncertainty and communication time delay, passivity based approaches can be utilized [15,16]. These approaches design controllers such that the two port network in Fig. 2.1 is a passive system. That is, the change in stored energy in the system over a given time is less than the input energy to the system. A critical assumption to the approach is passivity of the environment and user dynamics is required. This is because it utilizes the fact that the interconnection of a passive 2-port network with passive environment and user dynamics remain stable. One approach to show passivity of the two-port network is to look at power rates and ensure the network stores energy at a rate equal to or less than the energy supply rate. The power input/output rates can be obtained through the product of master/slave forces and velocities. A drawback of these approaches is that the fidelity of haptic feedback can be greatly

degraded.

For applications where the master and slave robots may be far apart, the issue of time delay may be problematic since the time lags introduced can cause instability [17]. There exists extensive works on the time-delay problem, some of which can be found in [16–18]. For more recent works one can refer to papers by Sirouspour and Shahdi [18–21]. In this thesis, time delay is assumed negligible since the immediate applications in mind are ones where the entire teleoperation system is in the same room.

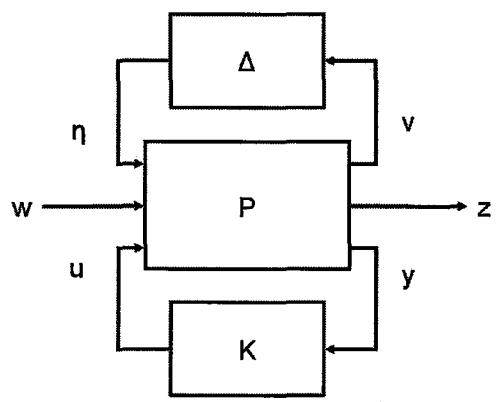

Figure 2.3: System for robust controller synthesis

Linear controllers based on the μ-synthesis and H_∞ theories have also been developed to achieve robust stability and transparency in the presence of uncertainties in the system dynamics [13, 22, 23]. These approaches transform the teleoperation system model, for example Fig. 2.2, to the standard form shown in Fig. 2.3 where K is the controller to be designed, Δ is the set of all possible uncertainty and P represents the plant dynamics. Furthermore, w is a vector signal including noises, disturbances and references signals, z is a vector of all controlled signals and tracking errors, η and ν the uncertainty interconnecting signals, u the control

signal and y the measurement. A fixed linear controller K is optimized such that gain from w to z is small with the constraint of system stability. For stability the small gain theorem is applied about the loop containing the uncertainty element where it is assumed the H_∞ norm of Δ is bounded.

An adaptive/nonlinear controller is proposed in [24] which employs nonlinear models of the master and slave robots to guarantee stability and transparency in the presence of dynamic uncertainty. This adaptive approach is a teleoperation extension of robotic adaptive control discussed by Slotine [25] and Sciavicco and Siciliano [26] and can be used to linearize the teleoperation system. The method is model-based since it requires models of both the master and slave systems to be utilized in a feed-forward term in the control signal. The unknown parameters of the master and slave systems are handled by adaptation. Convergence of the tracking errors and adaptation errors is shown using Lyapunov stability theory. This framework is used for the proposed controller in this thesis hence a detailed explaination on this adaptive controller is given in the next chapter.

2.2 Telesurgery and Soft-tissue Telemanipulation

Increased interest in telerobotic-robotic surgery is being driven by applications in minimally-invasive-robotic-surgery (MIRS) and robot assisted neurosurgery. MIRS is intended to replace conventional minimally-invasive surgery (MIS), where haptic fidelity is corrupted by surgical tool friction and non-intuitive motions pose challenges in training and performing the surgery. For example, Perrault et al.

have shown that the friction present in a typical MIS surgical tool degrades stiffness discrimination performance [27]. Researchers are exploring MIRS and computer assisted surgery to overcome the drawbacks of conventional MIS, a survey of the current technologies and approaches can be found in the paper by Dario et al. [8]. Tavakoli et al. outline some of the benefits of using haptic feedback in MIRS and present a novel end-effector capable of measuring interacting forces with tissue during teleoperation [28]. Deml et al. recruited 25 MIS surgeons to empirically investigate the importance of kinesthetic haptic feedback in MIRS and compare it to MIS [29]. They considered a dissection task for the surgeons to perform and confirmed that MIRS is suited for reducing unintentional injuries. Different levels of linearly-scaled force feedback were considered. The attitude among surgeons is that they prefer lower levels of force feedback, however their resulting performance in the dissection task showed no statistical differences. In neurosurgery the small spaces and need for precision pose challenges; the use of robotics can overcome these physical limitations through appropriate motion scaling and robot design. An overview of using robotics in neurosurgery is discussed by Zamorano et al. [30]. A haptic telerobotic system for neurosurgery is presented by Rossi et al. where the benefits of using such a system are discussed [31]. In any precise surgical procedure, surgeon hand tremor may be problematic. A study conducted with eye surgeons found unwanted tremor to be in the 8-12Hz range, while voluntary motions are typically below 2Hz [32]. Hence tremor suppression in teleoperation is another potential benefit that is being explored by researchers [33]. An overview of haptic telerobotics in robot-assisted surgery and its practical considerations can be found in [34].

In soft-tissue telemanipulation the design objectives must focus on the fidelity of the system. Traditional measures of transparency involve position and force tracking between master and slave such that the user would perceive the mechanical impedance of the task environment without distortion [10]. Such an approach could be restrictive particularly in fine tissue manipulation where human perception capabilities are limited. The work of Colgate in [22] is one of the early attempts at altering the operator's feel of the task through robust linear impedance shaping using a hybrid two-port network framework. In his work the impedance is shaped in the frequency domain where realistic shaping occurs only over a finite frequency range.

More recently, optimization of task-based fidelity measures have been proposed for soft-tissue telemanipulation assuming two-port hybrid network models [35,36]. Çavuşoğlu et al. have proposed a fidelity measure that optimizes differential environment impedance transmittance by explicitly formulating the goal of optimization to maximize worst case differential fidelity [35]. In their work the constraints of optimization were position tracking and stability where intervals of expected hand and environment impedance were assumed. The environments considered were those composed of spring and damper models where environment mass is neglected. De Gersem and Tendrick have also used an optimization based approach to improve teleoperation fidelity [36]. Their goal in optimization is to match transmitted impedance to scaled and mapped environment stiffness. The environments considered are those only of soft spring models. The same tracking and robust stability constraints were used in the optimization routine. The desired

impedance shaping is that the transmitted impedance increases differential sensitivity to environment stiffness assuming Weber's Law. In [37], Wang et al. have used an optimization based method, and have added a heuristic adaptive environment impedance estimation to improve system fidelity. However, the stability of this approach is not guaranteed. Moreover, all these methods ultimately result in linear scalings of position and force signals.

2.3 Haptic Perception

The haptic force feedback device is a critical component in any haptic enabled teleoperation system. Understanding how well humans interact with such devices and perceive haptics in general is important knowledge when one tries to design a haptic-enabled telerobotic system. General guidelines for haptic devices has been discussed by Hale and Stanney where both kinesthetic and tactile haptic receptors are discussed individually [5]. A general overview from a physiological standpoint as well as the frequency response ranges of both tactile and kinesthetic receptors is given. The tactile receptors are located in the skin and are responsible for skin sensations such as texture, roughness and vibration. The kinesthetic receptors are those related to body motion and muscle force are primarily located in the joints, ligaments and muscles. Procedures for experiments to focus on either kinesthetic or tactile cues using a tool or stylus have been presented by LaMotte where kinesthetic cues are shown to be important in stiffness perception [38].

The work surveyed by Hale and Stanney includes the extensive haptics experiments performed by O'malley and Goldfarb [39–42]. Their work focused on the effects of force saturation [41] and maximum surface stiffness [40, 42] on size and

shape identification experiments. The experiments were haptics only where vision feedback was not present. They concluded maximum force outputs in the range of 3-4 N [41] and surface stiffness of at least 300-400 N/m [40, 42] are sufficient to promote good haptic information transfer and levels above this do not significantly improve performance. When compared to real environments, the virtual haptic-limited environments had similar performance [39].

In haptic stiffness experiments including vision, it has been concluded that stiffness discrimination in both real and virtual environments follows Weber's Law [27, 43]. Wu et al. have compared discrimination in settings with and without vision and their results show vision feedback improves stiffness discrimination ability [44]. Srinivasan et al. have performed haptic experiments with distorted vision and have shown that it can have a negative impact on stiffness discrimination, hence it may be preferred in certain situations that vision feedback be ignored [45]. Barbagli et al. have investigated the impact of vision feedback in the context of force direction discrimination and found force direction discrimination for haptics with vision, haptic alone and haptics with incongruent vision to be 18.4°, 25.6° and 31.9° respectively [46].

Chapter 3

Lyapunov Based Adaptive Controllers

The dynamic models of the master and slave systems and their adaptive controllers are presented in this chapter. These include models of the master/slave robots as well as those of the hand and environment. A bilateral teleoperation control scheme is proposed where position and force feedback measurements are used locally and to facilitate teleoperation. Master/slave coordination is achieved through bilateral communication of position and force information. The control architecture is decentralized and the master and slave controllers employ an adaptive model-based component to allow convergence of tracking errors. Local stability is proved using Lyapunov stability theory. The adaptive controllers are based on those presented in [24] where they have been modified to accommodate the desired generalized non-linear and filtered force/position mappings.

3.1 Dynamics of Master/Slave Systems

The dynamics of the master ($\gamma = m$) and slave ($\gamma = s$) robots have the following general nonlinear form [26]:

$$D_\gamma(x_\gamma)\ddot{x}_\gamma + C_\gamma(x_\gamma, \dot{x}_\gamma)\dot{x}_\gamma + G_\gamma(x_\gamma) = F_\gamma - F_{ext,\gamma} \tag{3.1}$$

where x_γ is the workspace position vector, $D_\gamma(x_\gamma)$ is a positive definite mass matrix, $C_\gamma(x_\gamma, \dot{x}_\gamma)$ represents velocity dependent elements such as Coriolis and centrifugal effects, $G_\gamma(x_\gamma)$ corresponds to position-dependent forces such as gravity, F_γ is robot control force and $F_{ext,\gamma}$ represents external forces at the robot end-effector. The dynamic matrices posses the following properties [26],

$$D_\gamma(x_\gamma) = D_\gamma^T(x_\gamma) > 0 \tag{3.2}$$

$$x^T \left(\dot{D}_\gamma(y) - 2C_\gamma(y, z) \right) x = 0 \tag{3.3}$$

where the second property holds for $\forall x, y, z$ for a formulation based on the Christoffel symbols and only for $z = x$ otherwise. The external forces on the master and slave robots correspond to the hand and environment forces respectively. To simplify the design and analysis, the environment and operator dynamics are assumed to be second-order decoupled LTI models. Such models have been successfully used by other researchers [24]. Using such an approach the external master

robot forces are shown in (3.4) and for the slave robot in (3.5).

$$F_{ext,m} = -F_h = -\left(F_h^* - M_h\ddot{x}_m - B_h\dot{x}_m - K_h[x_m - x_{m0}]\right) \tag{3.4}$$

$$F_{ext,s} = F_e = M_e\ddot{x}_s + B_e\dot{x}_s + K_e[x_s - x_{s0}] \tag{3.5}$$

where M_e, M_h, B_e, B_h, K_e and K_h are positive diagonal matrices corresponding to mass, damping and stiffness, x_{s0} and x_{m0} represent the contact points of the environment and hand respectively, and F_h^* is the human exogenous input force subject to (3.6) where $\|\cdot\|_\infty$ denotes the L_∞ norm.

$$\|F_h^*\|_\infty \leq \alpha_h < +\infty, \quad \alpha_h > 0 \tag{3.6}$$

Using (3.1), (3.5) and (3.4), the dynamics of the master and slave systems can be represented by (3.7) and (3.8) respectively.

$$\mathcal{M}_m\ddot{x}_m + \mathcal{C}_m\dot{x}_m + \mathcal{G}_m = F_m + F_h^* \tag{3.7}$$

$$\mathcal{M}_m = D_m(x_m) + M_h$$

$$\mathcal{C}_m = C_m(\dot{x}_m, x_m) + B_h$$

$$\mathcal{G}_m = G_m(x_m) + K_h[x_m - x_{m0}]$$

$$\mathcal{M}_s\ddot{x}_s + \mathcal{C}_s\dot{x}_s + \mathcal{G}_s = F_s \tag{3.8}$$

$$\mathcal{M}_s = D_s(x_s) + M_e$$

$$\mathcal{C}_s = C_s(\dot{x}_s, x_s) + B_e$$

$$\mathcal{G}_s = G_s(x_s) + K_e[x_s - x_{s0}]$$

To facilitate the teleoperation control design, the slave dynamics are rewritten in mapped coordinates. By combining memoryless nonlinear monotonic mapping $\kappa_p(x_s)$ and its derivative (3.10) with the slave dynamics in (3.8), one obtains (3.12)

$$q_s = \kappa_p(x_s) \tag{3.9}$$

$$\dot{q}_s = \dot{\kappa}_p(x_s) = J\dot{x}_s \tag{3.10}$$

$$\ddot{q}_s = \ddot{\kappa}_p(x_s) = \dot{J}\dot{x}_s + J\ddot{x}_s \tag{3.11}$$

where $J = \frac{\partial \kappa(.)}{\partial x_s}$ is a configuration-dependent Jacobian matrix.

$$\mathcal{M}_s J^{-1} J\ddot{x}_s + \mathcal{C}_s J^{-1}\dot{q}_s + \mathcal{G}_s = F_s \tag{3.12}$$

By multiplying (3.12) by J^{-T} and employing (3.11) the new slave dynamics shown in (3.13) can be obtained.

$$\mathcal{M}'_s\ddot{q}_s + \mathcal{C}'_s\dot{q}_s + \mathcal{G}'_s = J^{-T}F_s \tag{3.13}$$

$$\mathcal{M}'_s = J^{-T}\mathcal{M}_s J^{-1}$$

$$\mathcal{C}'_s = J^{-T}[\mathcal{C}_s - \mathcal{M}_s J^{-1}\dot{J}]J^{-1}$$

$$\mathcal{G}'_s = J^{-T}\mathcal{G}_s$$

The skew-symmetry property of $\dot{\mathcal{M}}_s - 2\mathcal{C}_s$ is preserved under the above nonlinear coordinate transformation, i.e. $\dot{\mathcal{M}}'_s - 2\mathcal{C}'_s$ is also skew-symmetric, as long as J is nonsingular. This is seen by observing $\dot{J}^T\mathcal{M}'J - J^T\mathcal{M}'\dot{J}$ in (3.14) is skew-symmetric.

$$\dot{\mathcal{M}}_s - 2\mathcal{C} = \dot{J}^T\mathcal{M}'J - J^T\mathcal{M}'\dot{J} + J^T(\dot{\mathcal{M}}'_s - 2\mathcal{C}'_s)J \tag{3.14}$$

3.2 Control Design

The control design is divided into two subsections. The first subsection introduces the local adaptive controllers assuming some desired command vectors. It is shown that each local adaptive controller is stable via a suitable Lyapunov function. The second subsection gives the explicit form of the command vectors that facilitate the generalized force/position mappings.

3.2.1 Local Adaptive Controllers

The combined dynamics of operator/master and slave/environment are nonlinear and subject to uncertainty. Following a similar strategy to that in [24], local adaptive control laws are introduced for the master and slave robots in (3.15) and (3.16).

$$F_m = Y_m\hat{\Theta}_m + \mathcal{K}_m\rho_m - \alpha_h \text{sign}(\rho_m) \tag{3.15}$$

$$F_s = J^T[Y_s\hat{\Theta}_s + \mathcal{K}_s\rho_s] \tag{3.16}$$

$$\rho_m = v_{md} - H'_{xm}v_m + AH_{fh}F_h \tag{3.17}$$

$$\rho_s = v_{sd} - H'_{xs}\dot{\kappa}_p(x_s) - A\kappa_f(H_{fe}F_e) \tag{3.18}$$

$$H'_{xm} = 1 + H_{xm}, \qquad H'_{xs} = 1 + H_{xs} \tag{3.19}$$

where H_{xm}, H_{xs}, H_{fe} and H_{fh} are strictly proper stable LTI transfer functions, v_{md} and v_{sd} are master and slave command vectors to be introduced later, $\mathcal{K}_m$, $\mathcal{K}_s > 0$,

and $A > 0$ are diagonal matrices, and $\kappa_f(\cdot)$ is a monotonic nonlinear force mapping. In (3.15) and (3.16), $\hat{\Theta}_\gamma$ denotes the estimate of Θ_γ which contains all unknown parameters of the master ($\gamma = m$) or slave ($\gamma = s$). Furthermore, Y_m and Y_s are regressor matrices defined by

$$Y_m\Theta_m = \mathcal{M}_m\tfrac{d}{dt}[\rho_m + v_m] + \mathcal{C}_m[\rho_m + v_m] + \mathcal{G}_m \tag{3.20}$$

$$Y_s\Theta_s = \mathcal{M}'_s\tfrac{d}{dt}[\rho_s + \dot{\kappa}_p(x_s)] + \mathcal{C}'_s[\rho_s + \dot{\kappa}_p(x_s)] + \mathcal{G}'_s \tag{3.21}$$

The control laws (3.15) and (3.16) can each be split into two components, a feedback component $\mathcal{K}_\gamma\rho_\gamma$ and an adaptive model-based component $Y_\gamma\hat{\Theta}_\gamma$. The model-based components obey (3.22) where $\tilde{\Theta}_\gamma = \hat{\Theta}_\gamma - \Theta_\gamma$ represents a vector of parameter estimate errors.

$$Y_\gamma\hat{\Theta}_\gamma = Y_\gamma\tilde{\Theta}_\gamma + Y_\gamma\Theta_\gamma \tag{3.22}$$

The parameter adaptation laws are governed by

$$\dot{\hat{\Theta}}_{\gamma i} = \begin{cases} 0, & \hat{\Theta}_{\gamma i} \le \Theta^-_{\gamma i} \text{ and } Y^T_{\gamma i}\rho_\gamma \le 0 \\ 0, & \hat{\Theta}_{\gamma i} \ge \Theta^+_{\gamma i} \text{ and } Y^T_{\gamma i}\rho_\gamma \ge 0 \\ \Gamma_{\gamma i}Y^T_{\gamma i}\rho_\gamma, & \text{otherwise} \end{cases} \tag{3.23}$$

where γi denotes the ith parameter of either master ($\gamma = m$) or slave ($\gamma = s$), $\Gamma_{\gamma i} > 0$ represents a parameter update gain, $\Theta^-_{\gamma i}$ and $\Theta^+_{\gamma i}$ denote the minimum and maximum allowable values of $\Theta_{\gamma i}$. The update gain $\Gamma_{\gamma i}$ controls the speed of adaptation and the interval $[\Theta^-_{\gamma i}, \Theta^+_{\gamma i}]$ can be chosen based on knowledge of the master/slave robots and expected hand/environment impedances.

Combining master dynamics (3.7) with master control law (3.15) along with (3.20) and (3.22) yields system dynamics (3.24) for the master subsystem.

$$-Y_m\tilde{\Theta}_m = \mathcal{M}_m\dot{\rho}_m + \mathcal{C}_m\rho_m + \mathcal{K}_m\rho_m + F_h^* - \alpha_h \text{sign}(\rho_m) \tag{3.24}$$

The Lyapunov function (3.25) is chosen for master system dynamics (3.24).

$$V_m = \tfrac{1}{2}\rho_m^T\mathcal{M}_m\rho_m + \tfrac{1}{2}\tilde{\Theta}_m^T\Gamma_m^{-1}\tilde{\Theta}_m \geq 0 \tag{3.25}$$

where Γ_m is a constant diagonal matrix with diagonal elements equal to Γ_{mi}. Taking the derivative of V_m and using (3.24) yields

$$\begin{aligned}\dot{V}_m &= \tfrac{1}{2}\rho_m^T\dot{\mathcal{M}}_m\rho_m + \rho_m^T[-\mathcal{C}_m\rho_m - \mathcal{K}_m\rho_m - F_h^* + \alpha_h\text{sign}(\rho_m) - Y_m\tilde{\Theta}_m] + \dot{\tilde{\Theta}}_m^T\Gamma_m^{-1}\tilde{\Theta}_m \\ &= \tfrac{1}{2}\rho_m^T(\dot{\mathcal{M}}_m - 2\mathcal{C}_m)\rho_m + (\dot{\tilde{\Theta}}_m^T\Gamma_m^{-1} - \rho_m^TY_m)\tilde{\Theta}_m - \rho_m^T\mathcal{K}_m\rho_m + \rho_m^TF_h^* - \rho_m^T\alpha_h\text{sign}(\rho_m)\end{aligned} \tag{3.26}$$

Given the skew symmetry of $\dot{\mathcal{M}}_m - 2\mathcal{C}_m$, one finds $\frac{1}{2}\rho_m^T(\dot{\mathcal{M}}_m - 2\mathcal{C}_m)\rho_m = 0$. Assuming the true parameters Θ_m are constant, then $\dot{\tilde{\Theta}}_m = \dot{\hat{\Theta}}_m$ and using (3.23) results in $(\dot{\tilde{\Theta}}_m^T\Gamma_m^{-1} - \rho_m^TY_m)\tilde{\Theta}_m \leq 0$. Using (3.6) yields $\rho_m^TF_h^* \leq \rho_m^T\alpha_h\text{sign}(\rho_m)$. Therefore one obtains

$$\dot{V}_m \leq -\rho_m^T\mathcal{K}_m\rho_m \tag{3.27}$$

Since $\dot{V}_m \leq 0$, then V_m and ρ_m must have bounded maximum values meaning $\rho_m \in L_\infty$. Taking the integral of (3.27) one can show $\int_0^\infty \rho_m^T\mathcal{K}_m\rho_m\,dt < \infty$, hence $\rho_m \in L_2$. Hence the signal belongs to L_2 and L_∞, i.e.

$$\rho_m \in L_2 \cap L_\infty \tag{3.28}$$

Combining the mapped slave dynamics (3.13) with slave control law (3.16) along with (3.21) and (3.22) yields the following slave system dynamics

$$-Y_s\tilde{\Theta}_s = \mathcal{M}'_s\dot{\rho}_s + \mathcal{C}'_s\rho_s + \mathcal{K}_s\rho_s \tag{3.29}$$

The following Lyapunov function is then defined

$$V_s = \frac{1}{2}\rho_s^T\mathcal{M}'_s\rho_s + \frac{1}{2}\tilde{\Theta}_s^T\Gamma_s^{-1}\tilde{\Theta}_s \geq 0 \tag{3.30}$$

where Γ_s is a constant diagonal matrix with diagonal elements equal to Γ_{si}. Taking the derivative of V_s and using (3.29) one can obtain

$$\dot{V}_s = \frac{1}{2}\rho_s^T(\dot{\mathcal{M}}'_s - 2\mathcal{C}'_s)\rho_s + (\dot{\tilde{\Theta}}_s^T\Gamma_s^{-1} - \rho_s^TY_s)\tilde{\Theta}_s - \rho_s^T\mathcal{K}_s\rho_s \tag{3.31}$$

Since $\dot{\mathcal{M}}'_s - 2\mathcal{C}'_s$ is also skew symmetric, assuming $\dot{\tilde{\Theta}}_s = \dot{\hat{\Theta}}_s$ and employing (3.23) one obtains (3.32) and furthermore concludes (3.33).

$$\dot{V}_s \leq -\rho_s^T\mathcal{K}_s\rho_s \tag{3.32}$$

$$\rho_s \in L_2 \cap L_\infty \tag{3.33}$$

It should be noted that (3.20) and (3.21) contain the following

$$\rho_m + v_m = v_{md} - H_{xm}v_m + AH_{fh}F_h \tag{3.34}$$

$$\rho_s + \dot{\kappa}_p(x_s) = v_{sd} - H_{xs}\dot{\kappa}_p(x_s) - A\kappa_f(H_{fe}F_e) \tag{3.35}$$

Given the assumption on the strict properness of H_{xm}, H_{fh}, H_{xs} and H_{fe}, the terms $\ddot{x}_m$, $\dot{F}_h$, $\ddot{\kappa}_p(x_s)$ and $\dot{F}_e$ would not be required when taking the derivatives of (3.34) and (3.35). As will be seen in the next section, $\dot{v}_{md}$ and $\dot{v}_{sd}$ would also be free of these terms and therefore, acceleration and derivative of force are avoided in the implementation of the master controller (3.15) and slave controller (3.16).

3.2.2 Teleoperation

The new master and slave control commands v_{md} and v_{sd} in (3.17) and (3.18) must be designed to achieve the stated objectives of teleoperation, i.e. establishing nonlinear and filtered force/position mappings between the operator and the environment. To this end let

$$v_{md} = H'_{xs}\dot{\tilde{\kappa}}_p(x_s) - A\kappa_f(H_{fe}F_e) + \Lambda[H'_{xs}\tilde{\kappa}_p(x_s) - H'_{xm}x_m] \tag{3.36}$$

$$v_{sd} = H'_{xm}\tilde{v}_m + AH_{fh}F_h + \Lambda[H'_{xm}\tilde{x}_m - H'_{xs}\kappa_p(x_s)] \tag{3.37}$$

where $\Lambda > 0$ is diagonal. If $Q = x_m, v_m, \kappa_p(x_s), \dot{\kappa}_p(x_s)$, then $\tilde{Q}$ can be computed from the following filter

$$\dot{\tilde{Q}} + C\tilde{Q} = CQ \tag{3.38}$$

It is worth noticing that the choice of the coordinating controllers in (3.36) and (3.37) avoids acceleration and derivative of force measurements in $\dot{v}_{md}$ and $\dot{v}_{sd}$ which are needed in the local adaptive controllers.

Substituting (3.37) and (3.36) into (3.18) and (3.17) yield

$$\rho_m = [H'_{xs}\dot{\tilde{\kappa}}_p(x_s) - H'_{xm}v_m] + \Lambda[H'_{xs}\tilde{\kappa}_p(x_s) - H'_{xm}x_m] + A[H_{fh}F_h - \kappa_f(H_{fe}F_e)] \quad (3.39)$$

$$\rho_s = [H'_{xm}\tilde{v}_m - H'_{xs}\dot{\kappa}_p(x_s)] + \Lambda[H'_{xm}\tilde{x}_m - H'_{xs}\kappa_p(x_s)] + A[H_{fh}F_h - \kappa_f(H_{fe}F_e)] \quad (3.40)$$

Subtracting (3.40) and (3.39) gives

$$\begin{aligned} \rho_s - \rho_m &= H'_{xm}\tilde{v}_m - H'_{xs}\dot{\tilde{\kappa}}_p(x_s) + \Lambda[H'_{xm}\tilde{x}_m - H'_{xs}\tilde{\kappa}_p(x_s)] + \\ &\quad H'_{xm}v_m - H'_{xs}\dot{\kappa}_p(x_s) + \Lambda[H'_{xm}x_m - H'_{xs}\kappa_p(x_s)] \end{aligned} \quad (3.41)$$

which can be rewritten as

$$\underline{\tilde{\mathcal{X}}} + \underline{\mathcal{X}} = \rho_s - \rho_m \in L_2 \bigcap L_\infty \quad (3.42)$$

where

$$\underline{\mathcal{X}} = H'_{xm}v_m - H'_{xs}\dot{\kappa}_p(x_s) + \Lambda[H'_{xm}x_m - H'_{xs}\kappa_p(x_s)] \quad (3.43)$$

$$\dot{\underline{\tilde{\mathcal{X}}}} + C\underline{\tilde{\mathcal{X}}} = C\underline{\mathcal{X}} \quad (3.44)$$

The following result, Lemma 1 from [24], proves useful: Consider an equation $\dot{x} + cx = u$, where $c > 0$ is a positive constant and x is a differentiable function. If $u \in L_\infty$, then $\dot{x} \in L_\infty$ and $x \in L_\infty$; if $u \in L_2$, then $\dot{x} \in L_2$ and $x \in L_2$.

Substituting (3.44) into (3.42) and using Lemma 1 from [24] yields $\dot{\underline{\tilde{\mathcal{X}}}} \in L_2 \bigcap L_\infty$, $\underline{\tilde{\mathcal{X}}} \in L_2 \bigcap L_\infty$, and further

$$\underline{\mathcal{X}} \in L_2 \bigcap L_\infty \tag{3.45}$$

Applying Lemma 1 from [24] again with (3.43) and (3.45) it follows that

$$\rho_e = H'_{xm} x_m - H'_{xs} \kappa_p(x_s) \in L_2 \cap L_\infty \tag{3.46}$$

$$\rho_p = H'_{xm} v_m - H'_{xs} \dot{\kappa}_p(x_s) \in L_2 \cap L_\infty \tag{3.47}$$

This guarantees L_2 and L_∞ stability for both position and velocity tracking errors.

Adding (3.39) and (3.40) and exploiting $-C^{-1}\dot{\tilde{Q}} = \tilde{Q} - Q$ from (3.38) one obtains

$$\rho_s + \rho_m = 2A[H_{fh}F_h - \kappa_f(H_{fe}F_e)] - C^{-1}[H'_{xm}\dot{\tilde{v}}_m + H'_{xs}\ddot{\tilde{\kappa}}_p(x_s) + \Lambda H'_{xm}\dot{\tilde{x}}_m + \Lambda H'_{xs}\dot{\tilde{\kappa}}_p(x_s)] \tag{3.48}$$

Using (3.46) and (3.47), Eq. (3.48) can be rewritten as

$$H_{fh}F_h - \kappa_f(H_{fe}F_e) - \bar{\rho} = H_{Zt}x_m \tag{3.49}$$

with

$$\bar{\rho} = \tfrac{1}{2A}[\rho_s + \rho_m - C^{-1}(s+\Lambda)\tilde{\rho}_p] \in L_2 \cap L_\infty \tag{3.50}$$

$$H_{Zt} = H'_{xm}(\tfrac{C}{s+C})\mathcal{Z}_t \tag{3.51}$$

$$\mathcal{Z}_t = (AC)^{-1}s^2 + (AC)^{-1}\Lambda s \tag{3.52}$$

The proposed generalized transparency objectives are expressed in (3.46) and

(3.49). Nonlinear/filtered position tracking between master and slave is established in (3.46) where the nonlinear mapping $\kappa_p(\cdot)$ and the LTI filters H'_{xm} and H'_{xs} can be chosen arbitrarily, subject to stability constraints that will be discussed in later chapters. In the case of $H'_{xm} = H'_{xs} = 1$ and $\kappa_p(\cdot) = \kappa_p$, this would reduce to a standard linear position scaling between master and slave. The nonlinear/filtered force tracking between the user and environment, with an intervening virtual tool dynamics, is demonstrated in (3.49). Again, the strictly proper LTI filters H_{fh} and H_{fe} and the nonlinear mapping $\kappa_f(\cdot)$ can be arbitrarily selected subject to system stability. The dynamics of the virtual tool perceived by the operator are given by H_{Zt}/H_{fh} in (3.51) which are also adjustable by the control parameters. Under quasi-static conditions, the user's filtered hand force and nonlinearly mapped filtered environment force would track each other. In the case of $H'_{xm} = 1$ and $H_{fh} \approx 1$, the tool behaves as a mass-damper link for frequencies below C rad/s. If in addition $\kappa_f(\cdot) = \kappa_f$ and $H_{fe} \approx 1$, a conventional scaled force tracking with intervening mass-damper tool dynamics would result.

It must be noted that the stability of the local adaptive controllers, and the establishment of the generalized transparency objectives in (3.46) and (3.49) do not guarantee the stability of the overall system and this must be analyzed separately. The stability analysis can be simplified if the linear and nonlinear mappings are decoupled along the different axes of motion and if the user and environment dynamics are also assumed decoupled in these axes. Under such circumstances, using the proposed local adaptive and teleoperation control laws, the overall closed-loop dynamics are decoupled along the axes of motion. Therefore, without loss of generality, only motion in one axis is considered.

Using the following models for the hand and environment

$$F_h = F_h^* - \mathcal{Z}_h x_m \tag{3.53}$$

$$F_e = \mathcal{Z}_e x_s \tag{3.54}$$

and the generalized transparency equations in (3.49) and (3.46), the teleoperation block diagram in Fig. 3.1a) can be obtained. After some manipulations the teleoperation system can be reduced to the block diagram shown in Fig. 3.1b).

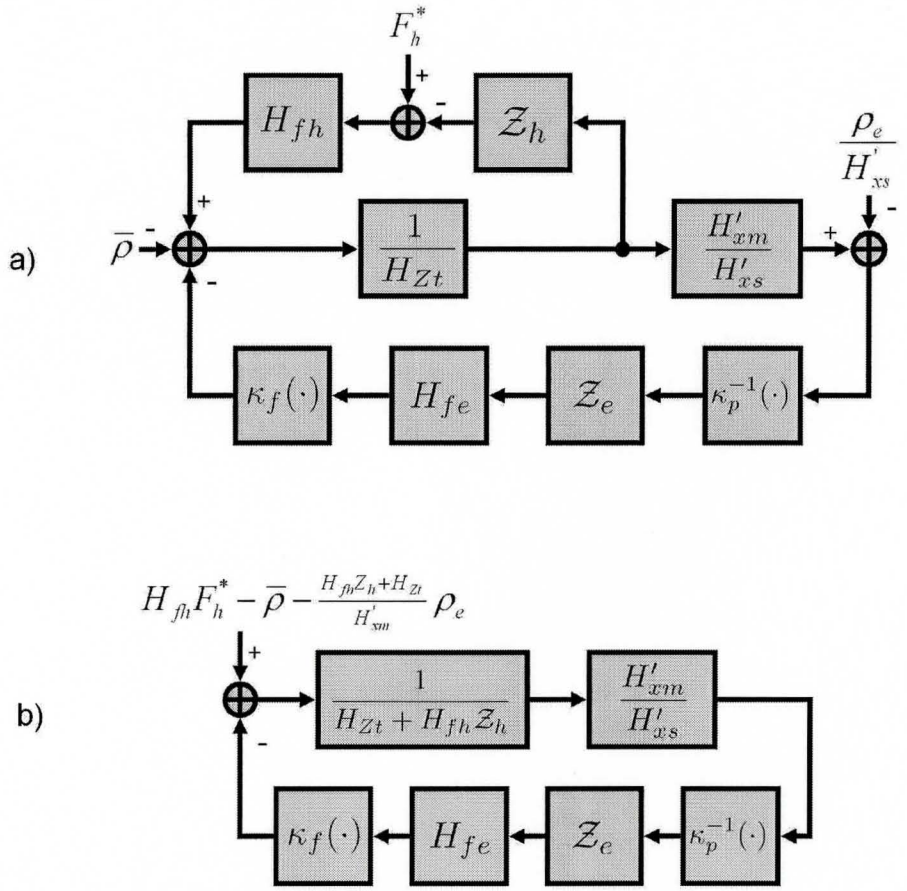

Figure 3.1: Teleoperation block diagrams.

It should be noted that the user and environment impedances $\mathcal{Z}_h$ and $\mathcal{Z}_e$ in Fig. 3.1 are usually unknown and subject to parametric uncertainty. Assuming $\kappa_p(\cdot)$, $\kappa_f(\cdot)$ are linear, $H'_{xm} = H'_{xs} = 1$ and $H_{fe} = H_{fh} = \frac{C}{s+C}$ leads to the guaranteed stability result obtained in [24], i.e.

$$\rho_m, \rho_s, \rho_e, \rho_p, \bar{\rho} \to 0 \tag{3.55}$$

$$v_m, v_s \in L_\infty \tag{3.56}$$

This stability result is valid for all mass-damper-spring type user and environment dynamics. In the general case of nonlinear and filtered force/position mappings, new conditions for robust stability must be derived. This will be discussed in later chapters. Specifically, interval plant systems theory presented in Chapter 4 and non-linear stability of Lur'e-Postnikov systems discussed in Chapter 5 are utilized and a stability analysis is shown in Chapter 6.

Chapter 4

Interval Plant Systems

Interval plant systems are families of plants that are parameterized by a set of intervals. Such systems are useful since a standard approach to show robust stability of a control system is to assume the plant transfer function is an interval plant system. Typically the coefficients of the transfer function polynomials are assumed to be some function of the interval parameters. In this chapter two special classes of interval plant systems are considered, Kharitonov plants and polytopic plants. In both cases it is assumed that the transfer functions for these plants have numerator and denominator polynomials whose parameters are independent of each other. The rest of this chapter will discuss some properties of these polynomials and present methods for finding the Bode and Nyquist envelopes of both plant systems. These methods are useful since they are used to show robust stability of the teleoperation block diagram in Fig. 3.1.

4.1 Interval Polynomials

Two special classes of interval polynomials are presented in this section. The first being polynomials with real independent interval coefficients, they are best analyzed using Kharitonov polynomials. The second are polynomials with real linearly dependent coefficients, referred to as polytopic polynomials.

4.1.1 Kharitonov Polynomials

Kharitonov polynomials are typically used to describe parametric polynomials of the following form

$$\mathcal{F}(s) = \delta_0 + \delta_1 s + \delta_2 s^2 + \delta_3 s^3 + ... \tag{4.1}$$

$$\delta_i^- \leq \delta_i \leq \delta_i^+$$

where δ_i are real, independent of each other and lie in the interval $[\delta_i^-, \delta_i^+]$. Substituting $s = j\omega$ into (4.1) and splitting it into its odd (imaginary) and even (real) parts yield

$$\mathcal{F}_{even}(\omega) = \delta_0 - \delta_2\omega^2 + \delta_4\omega^6 - \delta_6\omega^8 + ... \tag{4.2}$$

$$\frac{\mathcal{F}_{odd}(\omega)}{j\omega} = \delta_1 - \delta_3\omega^2 + \delta_5\omega^6 - \delta_7\omega^8 + ... \tag{4.3}$$

Knowing the coefficients lie in intervals it is straightforward to derive, for polynomial $\mathcal{F}(s)$, the four Kharitonov polynomials [47] shown below

$$\begin{aligned}
\mathcal{K}_{\mathcal{F}}^{1}(s) &= \mathcal{K}_{\mathcal{F}}^{even,min}(s) + \mathcal{K}_{\mathcal{F}}^{odd,min}(s) \\
&= \delta_0^- + \delta_1^- s + \delta_2^+ s^2 + \delta_3^+ s^3 + ... \\
\mathcal{K}_{\mathcal{F}}^{2}(s) &= \mathcal{K}_{\mathcal{F}}^{even,min}(s) + \mathcal{K}_{\mathcal{F}}^{odd,max}(s) \\
&= \delta_0^- + \delta_1^+ s + \delta_2^+ s^2 + \delta_3^- s^3 + ... \\
\mathcal{K}_{\mathcal{F}}^{3}(s) &= \mathcal{K}_{\mathcal{F}}^{even,max}(s) + \mathcal{K}_{\mathcal{F}}^{odd,min}(s) \\
&= \delta_0^+ + \delta_1^- s + \delta_2^- s^2 + \delta_3^+ s^3 + ... \\
\mathcal{K}_{\mathcal{F}}^{4}(s) &= \mathcal{K}_{\mathcal{F}}^{even,max}(s) + \mathcal{K}_{\mathcal{F}}^{odd,max}(s) \\
&= \delta_0^+ + \delta_1^+ s + \delta_2^- s^2 + \delta_3^- s^3 + ...
\end{aligned} \tag{4.4}$$

The Kharitonov polynomials define four extreme polynomials that can represent the entire interval polynomial family on the complex plane. This is best illustrated by plotting image sets of the polynomial family at different fixed values of $s = j\omega$. This is shown in Fig. 4.1 via an example where at each fixed ω a rectangle describes the entire family. The corners points are defined by the Kharitonov polynomials. This results since the independent coefficient polynomial family is easily separated into its real (even) and imaginary (odd) parts. Although the relative edge lengths may change the edge angles do not, meaning the normal vector to each edge remains unchanged.

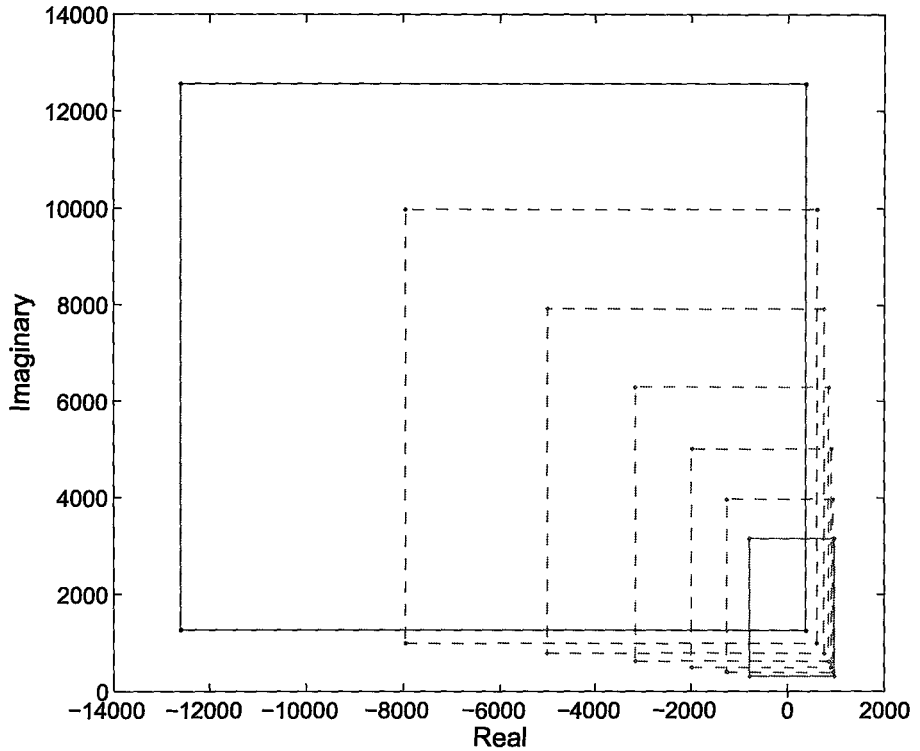

Figure 4.1: Image sets of $\mathcal{Z}_e = \delta_2 s^2 + \delta_1 s + \delta_0$ from $\omega = 63$ rad/s to 251 rad/s. Interval ranges: $\delta_2 \in [0.01, 0.2]$, $\delta_1 \in [5, 50]$ and $\delta_2 \in [10, 1000]$

Given the mentioned properties of Kharitonov polynomials, it is simple to derive a Hurwitz stability condition for real independent coefficient polynomial family. Assuming at least one member of the interval polynomial family is Hurwitz stable, i.e. one of the Kharitonov polynomials is Hurwitz, then the entire polynomial family is Hurwitz stable if and only if all four Kharitonov polynomials are Hurwitz [48].

Using the rectangular image set interpretation of the interval polynomial family, Hurwitz stability results if the origin is excluded from every rectangular image set at all frequencies of ω. Given that the roots of the polynomials change continuously and there exists at least one stable member, origin exclusion implies no

marginally stable roots on the $j\omega$ axis for the entire polynomial family. Origin exclusion of the image set can be shown to be equivalent to the four Kharitonov polynomials being Hurwitz stable [48]. One approach to show this is to use the contradiction argument given in section 5.4.2 of [48], where it is shown that in the limiting case the origin is on an edge entering the rectangle the monotonic phase property of one of the Hurwitz Kharitonov polynomials would be violated.

4.1.2 Polytopic Polynomials

Polynomials with real linearly dependent interval coefficients of the form (6.15) are considered to be polytopic polynomials.

$$C(s) = a_0(q) + a_1(q)s + ... + a_n(q)s^n \tag{4.5}$$

$$q = [\delta_0, \delta_1, ..., \delta_n]^T \tag{4.6}$$

$$\delta_i^- \leq \delta_i \leq \delta_i^+$$

The multidimensional variable q represents a (convex) hyper-rectangular uncertainty space and $a_i(q)$ a real polynomial coefficient that depends linearly/affinely on the elements of q. Linearly dependent interval coefficient polynomials have the polytopic property such that the image sets of $C(s)$ at fixed $s = jw$ define a bounded polytope or convex polygon [49] [2]. This is illustrated via an example in Fig. 4.2, where it is seen each image set is a convex polygon which can change shape and rotate and represents a different frequency ranging from 5 rad/s to 70 rad/s. Interval ranges: $\delta_5 \in [0.4, 0.7]$, $\delta_4 \in [0.01, 0.2]$, $\delta_3 \in [15, 115]$, $\delta_2 \in [5, 50]$, $\delta_1 \in [20, 1000]$, and $\delta_0 \in [10, 1000]$. A convex polygon is expected since linear/affine

transformations preserve set convexity [50]. Since convex polygons have straight edges the image set can be obtained from the convex hull of the vertex or extremal points. These points come from the vertex or extremal polynomials of the interval family at fixed $s = j\omega$. The Matlab convex hull algorithm *convhull* was used to draw the convex polygons in Fig. 4.2.

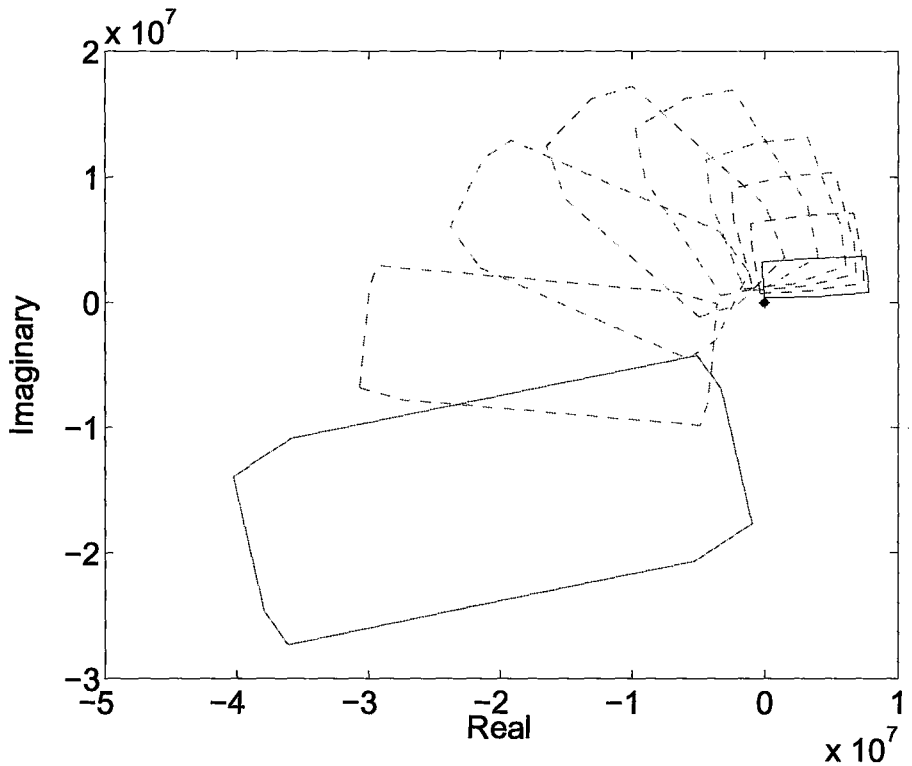

Figure 4.2: Image sets of example polytopic polynomial $C(s) = (s^2 + 19.87s + 3948)(\delta_4 s^2 + \delta_2 s + \delta_0) + (s^2 + 62.83s + 3948)(\delta_5 s^2 + \delta_3 s + \delta_1)$.

The vertex or extremal polynomials $C_{Vi}(s)$ of a polytopic family $C(s)$ can be found by using the extremal values of the uncertainty space q. Thus each vertex/extremal polynomial corresponds to a corner of the hyper-rectangle defined by q. If q has n elements, 2^n vertex/extremal polynomials can be defined for the interval family.

When dealing with polytopic polynomials one is typically interested in applying the Edge theorem [51] [48], where the edges of the hyper-rectangular parameter space q are checked. In particular a subset of these edges define the convex polygon image sets previously discussed. For a q of dimension n with 2^n vertices, $2^{n-1}(2^n - 1)$ interconnecting edges can be defined. These interconnecting edges connect all vertices to each other. The number of edges to be checked can be reduced to $2^{n-1}n$ by using only the outer exposed edges of the hyper-rectangle q [48]. An exposed edge is defined as being able to move from one vertex to another by only varying one dimension. This concept of varying along a dimension can be utilized to derive the exposed edge formula with the aid of Fig. 4.3 where $N_{ee}(n)$ denotes the number of exposed edges of an object with dimension n. It is seen the number of exposed edges follows a recursive pattern given by $N_{ee}(n) = 2N_{ee}(n-1) + 2^{n-1}$, solving this yields $N_{ee}(n) = 2^{n-1}n$.

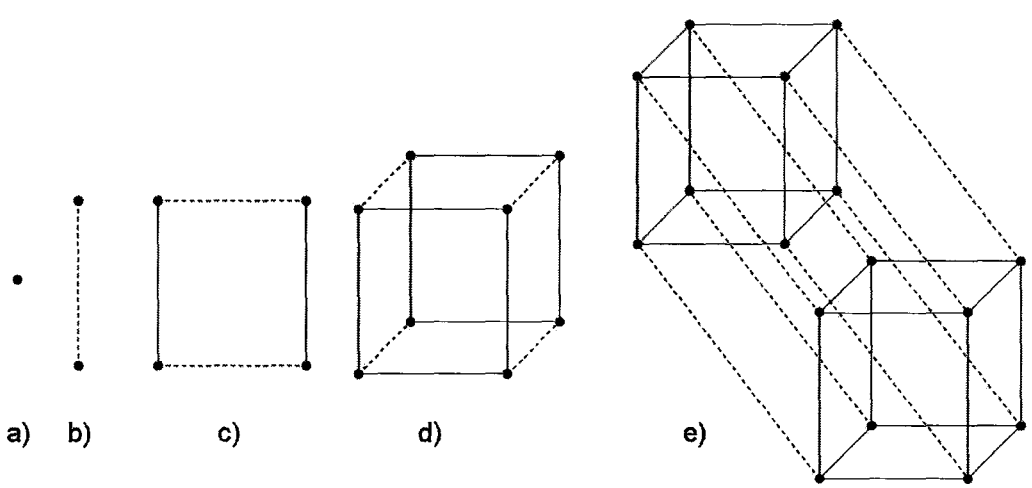

Figure 4.3: Number of exposed edges as a function of object dimension a) point $N_{ee}(0) = 0$ b) line $N_{ee}(1) = 1$ c) square $N_{ee}(2) = 4$ d) cube $N_{ee}(3) = 12$ e) tasseract (4-D hypercube) $N_{ee}(4) = 32$

The edges of the convex polygon image set at fixed $s = j\omega$ come from a subset of the outer exposed edges. In particular the polygon is composed of at most $2n$ edges and $2n$ vertices assuming q has dimension n [2]. The explanation of this is given as follows. The $2^{n-1}n$ exposed edges can be divided into n groups where in each group 2^{n-1} edges are parallel to each other when mapped to the complex plane image set. The mapped exposed edges in each group that, when extended, have the minimum and maximum intersections with the imaginary (or real) axis are the ones that compose two edges of the convex polygon. This is shown in Fig. 4.4 where the uncertainty space has dimension three.

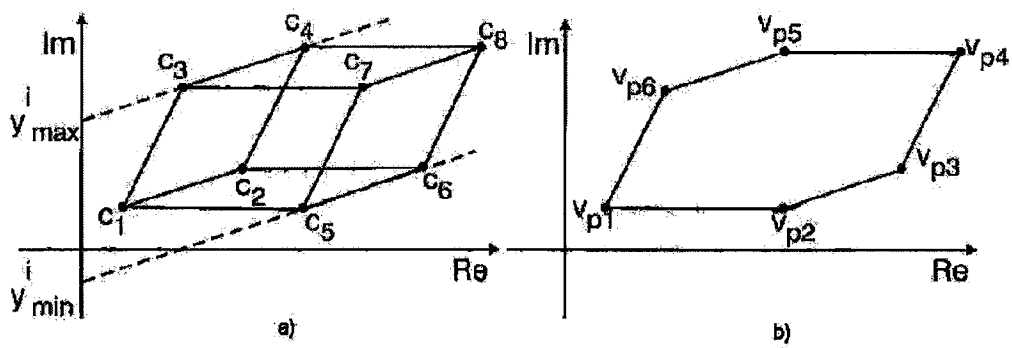

Figure 4.4: Image sets with uncertainty dimension $n = 3$ a) image of mapped exposed edges b) 2-n convex polygon. Figure modified from [2].

This reduction in the number of vertices and edges can greatly improve the computation efficiency of algorithms that utilize vertex and edge checking. It should be noted that this reduced set of vertices/edges may change as the variable $s = j\omega$ is varied, hence identifying the $2n$ edges/vertices is a non-trival matter. One approach is to use a convex hull finding algorithm, such as Matlab *convhull*, at each $s = j\omega$ to find this reduced set of vertices/edges.

Vertex and edge checking is desired when one would like to show an interval polytopic polynomial family of the form (6.15) is Hurwitz stable. As with the Kharitonov polynomial image sets, Hurwitz stability of the polytopic polynomial family is assured if and only if the origin is excluded from the $2n$ convex polygon image sets at every frequency ω. In contrast with Kharitonov polynomials Hurwitz stability of the vertex/extremal polynomials does *not* guarantee stability of the whole interval family [48]. Fortunately the polytopic property of the image sets still allows for a vertex only stability check that avoids computationally expensive edge checking [49].

A convex polygon can be shown to exclude the origin if and only if a line can be found that separates the vertices of the polygon from the origin. If such a line can be found at every frequency Hurwitz stablity follows since no marginally stable roots exist. The implementation of such a test may require an extra sweeping variable to find such a separating line, an idea central to the approach outlined in [49]. Since only Hurwitz stability is being considering the need for this line slope sweeping variable is avoided by utilizing the phase of the vertex/extremal polynomials of the polytopic polynomial family. For ease in implementation an offset phase value for each vertex polynomial has been developed as follows

$$\phi_{C_{Vi}}(\omega) = \text{Arg}(C_{Vi}(j\omega)) - \text{Arg}(C_{V^*}(j\omega)) + 2\pi k \tag{4.7}$$

where $C_{Vi}(s)$ is a vertex polynomial, C_{V^*} an arbitrary vertex polynomial, Arg$(\cdot)$ returns the principal argument of a complex number and an integer value of k is

chosen as

$$k = \begin{cases} -1, & \text{Arg}(C_{Vi}(j\omega)) - \text{Arg}(C_{V^*}(j\omega)) > \pi \\ 1, & \text{Arg}(C_{Vi}(j\omega)) - \text{Arg}(C_{V^*}(j\omega)) < -\pi \\ 0, & \text{otherwise} \end{cases} \tag{4.8}$$

so that (4.9) is satisfied.

$$-\pi \leq \quad \phi_{C_{Vi}}(\omega) \quad \leq \pi \tag{4.9}$$

Note the arbitrary vertex polynomial C_{V^*} need not be the same for all frequencies but must be the same for all $\phi_{C_{Vi}}(\omega)$ for a given fixed ω.

This phase offset transformation has the effect of rotating the convex hulls at each frequency so that they all intersect the positive real axis. The origin is excluded from the image sets of $C(j\omega)$ if and only if the maximum phase difference among $\phi_{C_{Vi}}(\omega)$ at every frequency ω is less than π. The proof of this is obvious using plane geometry. The stability condition can thus be written as (4.10).

$$\sup_{\omega \in \Re^+} [\max_i \phi_{C_{Vi}}(\omega) - \min_i \phi_{C_{Vi}}(\omega)] < \pi \tag{4.10}$$

The implementation of (4.10) in a stability analysis is simple since it only requires phase values between $-\pi$ and π of a limited set of known vertex polynomials.

4.2 Kharitonov Plants

Interval plant systems where the numerator and denominator polynomials are real independent coefficient polynomials are suited to be analyzed by Kharitonov plants. For a transfer function $T(s) = \frac{\mathcal{N}(s)}{\mathcal{D}(s)}$ with independent interval coefficients, sixteen Kharitonov plants can be defined as follows

$$T_K(s) = \left\{ \frac{\mathcal{K}_{\mathcal{N}}^i(s)}{\mathcal{K}_{\mathcal{D}}^k(s)} : i,k \in \{1,2,3,4\} \right\} \tag{4.11}$$

where the Kharitonov polynomials have been defined in (4.4). The rest of this section will describe methods of constructing Bode and Nyquist envelopes of independent coefficient interval plant systems.

4.2.1 Bode Envelope

A Bode envelope for an independent coefficient interval plant tranfer function $T(s) = \frac{\mathcal{N}(s)}{\mathcal{D}(s)}$ can be constructed with the aid of Kharitonov plants (4.11) and Kharitonov polynomials (4.4). The minimum/maximum phase of $T(j\omega)$ can be found from the minimum/maximum phase of the sixteen Kharitonov plants $T_K(j\omega)$ [48]. This follows since at a given frequency ω the extreme phase values of both numerator and denominator polynomials of $T(j\omega)$ occur at one of its Kharitonov polynomials via the rectangular image set argument. This is illustrated is Fig. 4.5. For the case where the origin may potentially go through the image set phase continuity of the Kharitonov polynomials is used to show the phase envelope still results from the Kharitonov polynomials.

For a gain envelope the minimum/maximum gain of the numerator and denominator polynomials must be obtained. From Fig. 4.5 the maximum gain of an independent coefficient polynomial also occurs at one of the image set corners hence one of the Kharitonov polynomials. However the minimum polynomial gain may occur at a vertex, an edge or even be zero. Regardless, the minimum gain can still be easily obtained using the vertex points given by the Kharitonov polynomials.

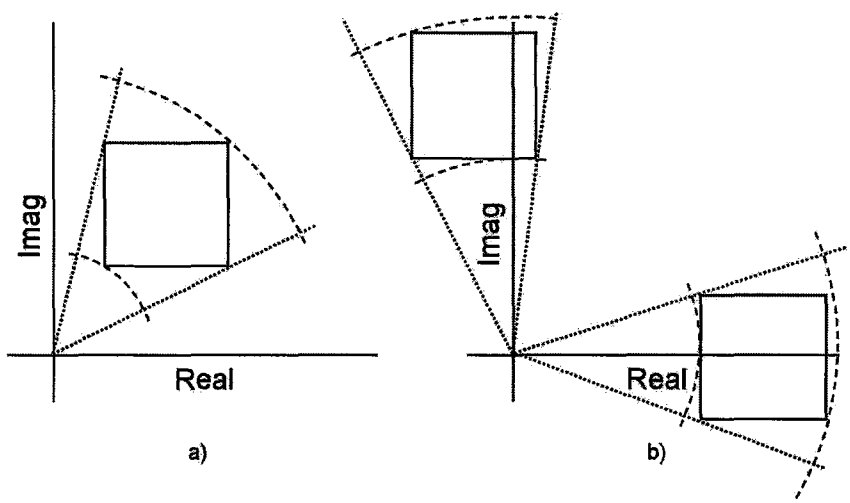

Figure 4.5: Minimum/maximum gain/phase of recangular image set a) strictly in one quadrant b) intersecting real or imaginary axis.

For minimum gain to be non-zero the origin must be excluded from the image set. This can be shown by using for example the line separating test discussed in the previous section with the Kharitonov polynomial vertex points. For image sets that are only in one quadrant, see Fig. 4.5a), the minimum gain occurs at a vertex hence at a Kharitonov polynomial. This condition is easily checked using the vertex co-ordinates. For image sets that intersect the real (imaginary) axis the minimum gain is the minimum absolute value of the real (imaginary) part of the

vertex points as in Fig. 4.5b). Hence the minimum gain of real independent interval coefficient polynomial $\mathcal{F}(j\omega)$ at fixed frequency ω is given by

$$\min|\mathcal{F}(j\omega)|=\begin{cases} 0, & \text{origin included} \\ \min_i|\mathrm{Re}[\mathcal{K}^i_{\mathcal{F}}(j\omega)]|, & \min_i \mathrm{Im}[\mathcal{K}^i_{\mathcal{F}}(j\omega)] < 0 < \max_i \mathrm{Im}[\mathcal{K}^i_{\mathcal{F}}(j\omega)] \\ \min_i|\mathrm{Im}[\mathcal{K}^i_{\mathcal{F}}(j\omega)]|, & \min_i \mathrm{Re}[\mathcal{K}^i_{\mathcal{F}}(j\omega)] < 0 < \max_i \mathrm{Re}[\mathcal{K}^i_{\mathcal{F}}(j\omega)] \\ \min_i|\mathcal{K}^i_{\mathcal{F}}(j\omega)|, & \text{otherwise} \end{cases} \tag{4.12}$$

Given that the maximum gain and phase extremes occur at the Kharitonov polynomials and using the minimum gain relation in (4.12), the bode envelope of independent coefficient interval transfer function $T(s) = \frac{\mathcal{N}(s)}{\mathcal{D}(s)}$ can be found using (4.13)-(4.16).

$$\min|T(j\omega)| = = \frac{\min|\mathcal{N}(j\omega)|}{\max_i|\mathcal{K}^i_{\mathcal{D}}(j\omega)|} \tag{4.13}$$

$$\max|T(j\omega)| = = \frac{\max_i|\mathcal{K}^i_{\mathcal{N}}(j\omega)|}{\min|\mathcal{D}(j\omega)|} \tag{4.14}$$

$$\min\arg(T(j\omega)) = \min_i \arg(\mathcal{K}^i_{\mathcal{N}}(j\omega)) - \max_i \arg(\mathcal{K}^i_{\mathcal{D}}(j\omega)) \tag{4.15}$$

$$\max\arg(T(j\omega)) = \max_i \arg(\mathcal{K}^i_{\mathcal{N}}(j\omega)) - \min_i \arg(\mathcal{K}^i_{\mathcal{D}}(j\omega)) \tag{4.16}$$

4.2.2 Nyquist Envelope

It may desired to obtain a Nyquist envelope of the interval plant system $T(s) = \frac{\mathcal{N}(s)}{\mathcal{D}(s)}$, where $\mathcal{N}(s)$ and $\mathcal{D}(s)$ are real independent coefficient interval polynomials.

The result of Hollot and Tempo [3] prove useful where it is shown the *outer* Nyquist envelope is obtained from the union of the sixteen Kharitonov plants (4.11).

The following theorem from [3] is used to prove this result. Let $z_0 \in T_K^{i,k}(j\omega)$ for some $i, k = 1, 2, 3, 4$. Then z_0 is contained in the Nyquist envelope of $T(j\omega)$ if

i) There exists a $z_1 \in \mathcal{C}$ such that $\mathcal{K}_{\mathcal{N}}^i(s) - z_1\mathcal{K}_{\mathcal{D}}^k(s)$ is Hurwitz for $i, k = 1, 2, 3, 4$

ii) there exists a connected path $\Gamma \subset \mathcal{C}\backslash 0$ with endpoints z_0 and z_1, having no other point in common with $T_K^{i,k}(j\omega)$, $i, k = 1, 2, 3, 4$.

The proof of this theorem is given in appendix A of [3] where it is shown that, assuming conditions i) and ii) hold, the point z_0 is part of and connected to the Nyquist envelope of $T(j\omega)$ and z_0 is on the boundary of the envelope where it can reach points not part of the envelope. A key point to understanding the proof is that Hurwitz stability of $\mathcal{K}_{\mathcal{N}}^i(s) - z\mathcal{K}_{\mathcal{D}}^k(s)$ implies Hurwitz stability of the family $\mathcal{N}(s) - z\mathcal{D}(s)$. Note z_0 results in marginally stable $\mathcal{K}_{\mathcal{N}}^i(s) - z_0\mathcal{K}_{\mathcal{D}}^k(s)$. Using a continuity of roots argument, a point z_1 chosen to be outside the envelope one can deduce the points z_0 will yield the outer Nyquist envelope since one can always find a path from z_1 to z_0.

An illustrative example from [3] using the tranfer function (4.17) shows how an outer envelope in Fig. 4.6b) can be obtained using the union of the Nyquist plots of the Kharitonov plants in Fig. 4.6a).

$$G(s) = \frac{39060(r_3s^3 + r_2s^2 + r_1s + r_0)}{s^7 + q_6s^6 + q_5s^5 + q_4s^4 + q_3s^3 + q_2s^2 + q_1s + q_0} \tag{4.17}$$

where

$r_3 \in [0.8, 8]$ $r_2 \in [3.28, 32.8]$ $r_1 \in [3.52, 35.2]$

$r_2 \in [0.32, 3.2]$ $q_6 \in [81.32, 81.92]$ $q_5 \in [3910.38, 3960.94]$

$q_4 \in [61412.23, 63897.28]$ $q_3 \in [343379.7, 386727.7]$ $q_2 \in [620977.75, 915287.75]$

$q_1 \in [1324350, 1978350]$ $q_0 \in [126562.5, 189062.5]$

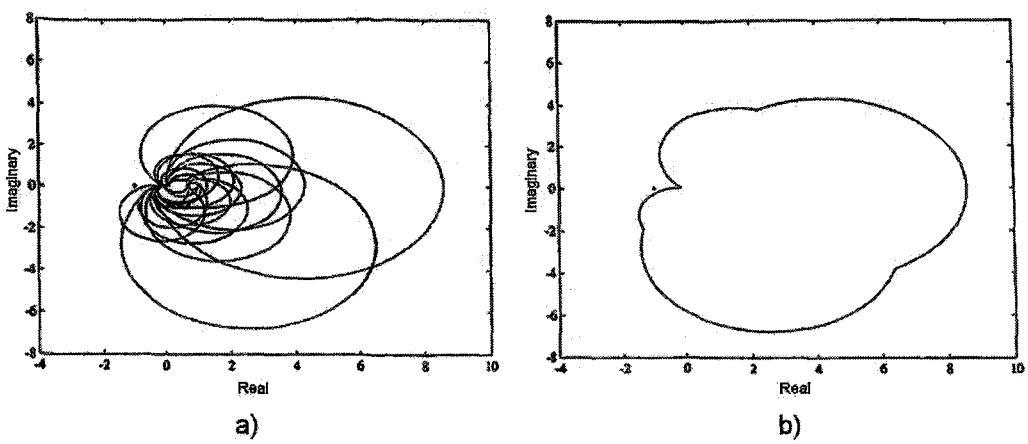

Figure 4.6: Figures from [3] a) Nyquist plots of Kharitonov plants b) Nyquist envelope

In many practical robust control problems the outer Nyquist is sufficient, however if the inner envelope is needed it cannot be obtained entirely from the sixteen Kharitonov plants. Although large portions of the *inner* Nyquist envelope may be obtained from the Kharitonov plants some portions may require edge checking to obtain a complete inner Nyquist envelope [3]. It is also noted that an alternate version of the outer Nyquist envelope proof can be found in [52] where the Hermite-Biehler theorem has been used.

4.3 Polytopic Plants

Assuming an interval plant transfer function contains polynomials with linearly dependent coefficients is far less restrictive than an independent coefficient approach suited for Kharitonov polynomials. This section presents methods for obtaining Bode and Nyquist envelopes for polytopic plants of the form (4.18) whose numerator and denominator polynomials are polytopic polynomials whose interval parameters are independent of each other. The methods described here are those that are found in [2].

$$P(s) = \frac{N(s)}{D(s)} = \frac{a_0(q) + a_1(q)s + ... + a_n(q)s^n}{b_0(r) + b_1(r)s + ... + b_m(r)s^m} \tag{4.18}$$

$$q = [\delta_0, \delta_1, ..., \delta_n]^T, \quad r = [\vartheta_0, \vartheta_1, ..., \vartheta_m]^T$$

$$\delta_i^- \leq \delta_i \leq \delta_i^+, \quad \vartheta_i^- \leq \vartheta_i \leq \vartheta_i^+$$

4.3.1 Bode Envelope

Since it is assumed the numerator and denominator polynomials are independent of each other, the Bode envelope of polytopic plant $P(s)$ is found by finding the phase and gain envelopes of $N(j\omega)$ and $D(j\omega)$.

As was stated before, polytopic polynomials have image sets that are convex polygons whose vertices from a subset of the vertex polynomials. Like rectangular image sets, convex polygon image sets have their extreme phase values and maximum gain at the vertices, e.g. see Fig. 4.7. Minimum gain can potentially occur at

an edge or be zero. To test for zero gain the origin exclusion ideas discussed before can be applied. To handle minimum gain potentially occurring on an edge the methods described in [2] are utilized to find minimum gain using only the vertices.

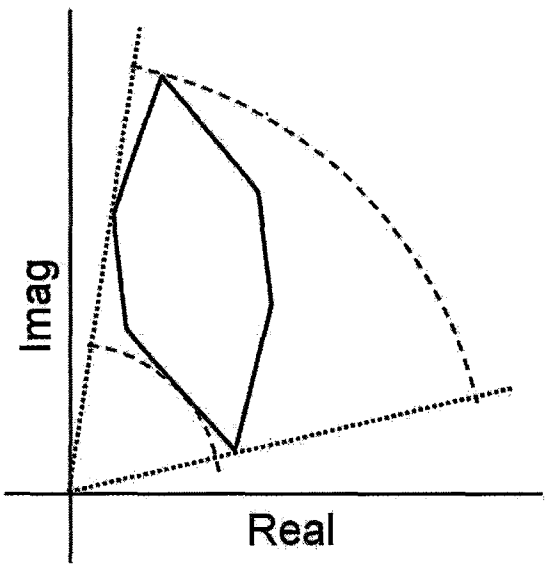

Figure 4.7: Minimum/maximum gain/phase of convex polygon image set

The minimum gain of polytopic polynomials $C(s)$ at fixed $s = j\omega$ assuming non-zero minimum gain is given by (4.19) [2]

$$\min |C(j\omega)| = \begin{cases} |v_i|, & |v_i| < |k_1| \text{ and } |v_i| < |k_2| \\ l_1 & |k_1| < |v_i| \text{ and } |k_2| >= |v_i| \\ l_2 & |k_2| < |v_i| \text{ and } |k_1| >= |v_i| \\ \min(l_1, l_2) & |k_1| < |v_i| \text{ and } |k_2| < |v_i| \end{cases} \tag{4.19}$$

where v_i is the vertex closest to the origin and v_1 and v_2 are edge adjacent vertices as shown in Fig. 4.8. Points k_1 and k_2 are close to v_i specified by equation (4.20) where λ is a small number typically about 10^{-6}. Scalars l_1 and l_2 are distances from

the line equations defined by the edges adjacent to v_i whose exact values are given by (4.21) and (4.22).

$$k_{1,2} = v_i(1-\lambda) + \lambda v_{1,2} \tag{4.20}$$

$$l_{1,2} = \frac{\sqrt{(2|v_i|\rho_{1,2})^2 - (|v_i|^2 - |v_{1,2}|^2 + \rho_{1,2}^2)^2}}{2\rho_{1,2}} \tag{4.21}$$

$$\rho_{1,2} = \sqrt{(\mathrm{Re}[v_{1,2}] - \mathrm{Re}[v_i])^2 + (\mathrm{Im}[v_{1,2}] - \mathrm{Im}[v_i])^2} \tag{4.22}$$

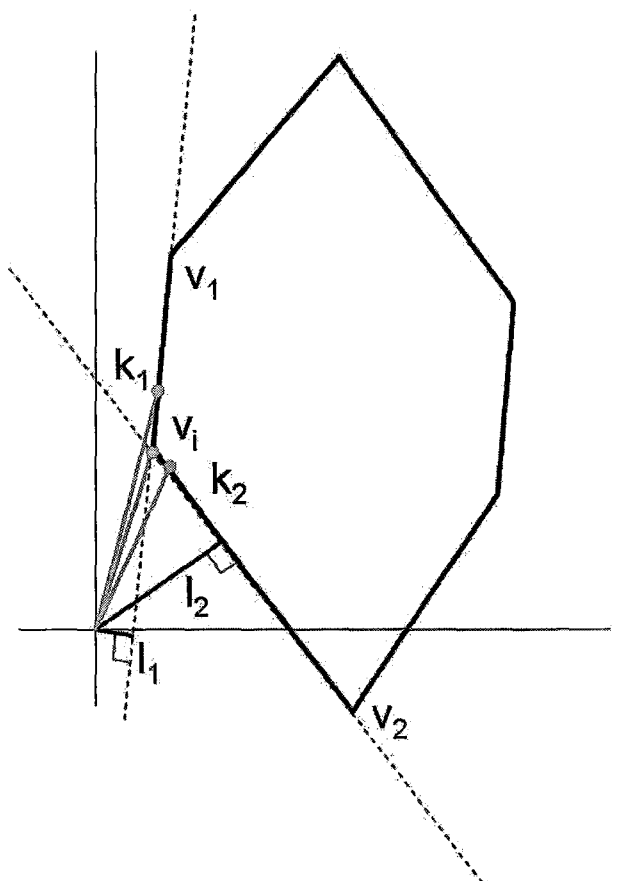

Figure 4.8: Minimum gain of convex polygon image set.

One approach to find v_i, v_1 and v_2 is to use a convex hull algorithm (Matlab *convhull*) which returns the vertices in order such that two successive vertices define an exposed edge. It should also be noted that the fourth condition in (4.19) is not mentioned in [2] but it is needed to avoid calculating an erroneous minimum gain. For example consider the convex shape in Fig. 4.9 where the fourth condition will correctly pick between the two edges distances.

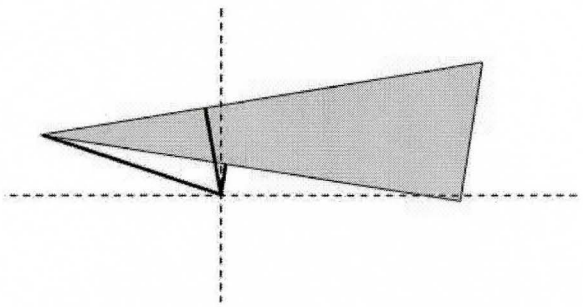

Figure 4.9: Example where the closest vertex is farther than its two adjacent edges.

The bode envelope of polytopic interval transfer function $P(s) = \frac{N(s)}{D(s)}$ can be obtained using the minimum gain relation (4.19), the vertex polynomials $N_{Vi}(j\omega)$ and $D_{Vi}(j\omega)$ with equations (4.23)-(4.26).

$$\min |P(j\omega)| = = \frac{\min |N(j\omega)|}{\max_i |D_{Vi}(j\omega)|} \tag{4.23}$$

$$\max |P(j\omega)| = = \frac{\max_i |N_{Vi}(j\omega)|}{\min |D(j\omega)|} \tag{4.24}$$

$$\min \arg(P(j\omega)) = \min_i \arg(N_{Vi}(j\omega)) - \max_i \arg(D_{Vi}j\omega)) \tag{4.25}$$

$$\max \arg(P(j\omega)) = \max_i \arg(N_{Vi}(j\omega)) - \min_i \arg(D_{Vi}(j\omega)) \tag{4.26}$$

4.3.2 Nyquist Envelope

The Nyquist envelope of polytopic plants of the form (4.18) cannot, in general, be formed from the union of special extremal plants [2] [48]. An application of the Edge theorem [51] is necessary to determine the Nyquist envelope of (4.18). Specifically the method described in [2] is used where the exposed edges/vertices of the convex polygon image sets of $N(j\omega)$ and $D(j\omega)$ are utilized as minimal sets of vertices and edges to be used in forming the required Nyquist envelope. This approach reduces the number of edges from $2^{n-1}n$ uncertainty box outer exposed edges to $2n$ and reduces the number of vertices from 2^n to $2n$; here n represents the number of unknown interval parameters in polynomial $N(s)$ or $D(s)$ [2].

To identify the reduced set of vertices and edges a convex hull algorithm, such as Matlab *convhull*, can be utilized with the vertex points given by vertex polynomials $N_{Vi}(j\omega)$ and $D_{Vi}(j\omega)$ at fixed frequency ω. The convex hull algorithm should return the convex hull vertices in an order such that two successive vertices define an exposed edge of the convex polygon image set of $N(j\omega)$ or $D(j\omega)$. Once this reduced set of vertices and edges have been identified the boundary of the Nyquist envelope of $P(j\omega)$ at fixed ω is given by [2]

$$\delta P(j\omega) \subset \frac{S_{N_V}}{S_{D_E}} \cup \frac{S_{N_E}}{S_{D_V}} \tag{4.27}$$

$$S_{N_V} = \{v_1^N, v_2^N, ..., v_p^N\} \tag{4.28}$$

$$\begin{aligned} S_{N_E} = \{&(1-\lambda)v_1^N + \lambda v_2^N, (1-\lambda)v_2^N + \lambda v_3^N, \\ &..., (1-\lambda)v_p^N + \lambda v_1^N\}, \lambda \in [0,1] \end{aligned} \tag{4.29}$$

$$S_{D_V} = \{v_1^D, v_2^D, ..., v_r^D\} \tag{4.30}$$

$$S_{D_E} = \{(1-\lambda)v_1^D + \lambda v_2^D, (1-\lambda)v_2^D + \lambda v_3^D, ..., (1-\lambda)v_r^D + \lambda v_1^D\}, \lambda \in [0,1] \tag{4.31}$$

where δ denotes the boundary. Sets S_{N_E}, S_{N_V} define the edge and vertex sets of complex convex polygon $N(j\omega)$ with p number of exposed vertices/edges; S_{D_E}, S_{D_V} define the edge and vertex sets of complex convex polygon $D(j\omega)$ with r number of exposed vertices/edges. Both edge sets utilize an edge sweeping variable λ. An example application of (4.27) is shown in Fig. 4.10 where a Nyquist template is plotted using the interval plant (4.32). The curved arcs in this example are due to S_{N_V}/S_{D_E} and the straight lines come from S_{N_E}/S_{D_V}.

$$G(s) = \frac{(s^2 + 19.87s + 3948)(\delta_2 s^2 + \delta_1 s + \delta_0)}{(s^2 + 62.83s + 3948)(\vartheta_2 s^2 + \vartheta_1 s + \vartheta_0)} \tag{4.32}$$

where $\delta_2 \in [0.01, 0.2]$, $\delta_1 \in [5, 50]$, $\delta_0 \in [10, 1000]$, $\vartheta_2 \in [0.4, 0.7]$, $\vartheta_1 \in [15, 115]$, and $\vartheta_0 \in [20, 1000]$.

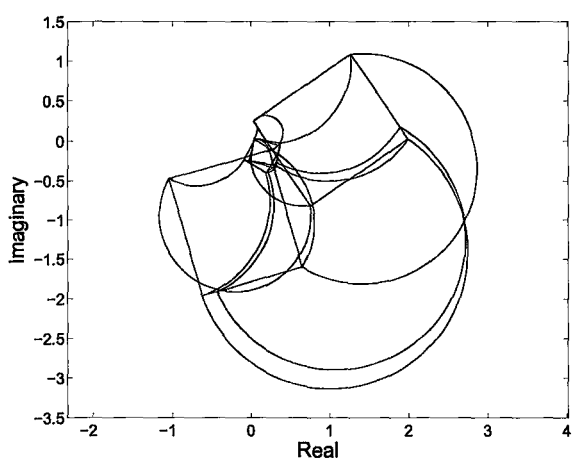

Figure 4.10: Nyquist template of $G(j\omega)$ at $\omega = 30$ rad/s

A Nyquist envelope of polytopic plant (4.32) can be obtained by applying (4.27) at every frequency. This is shown in Fig. 4.11 where for comparison the 64 extremal plants $G_V^{i,k}(s) = \frac{N_{Vi}(s)}{D_{Vk}(s)}$, $i,k = \{1,2,..,2^3\}$, are also shown. From Fig. 4.11b) the necessity of edge checking is shown since portions of the envelope are not covered by the extremal plants.

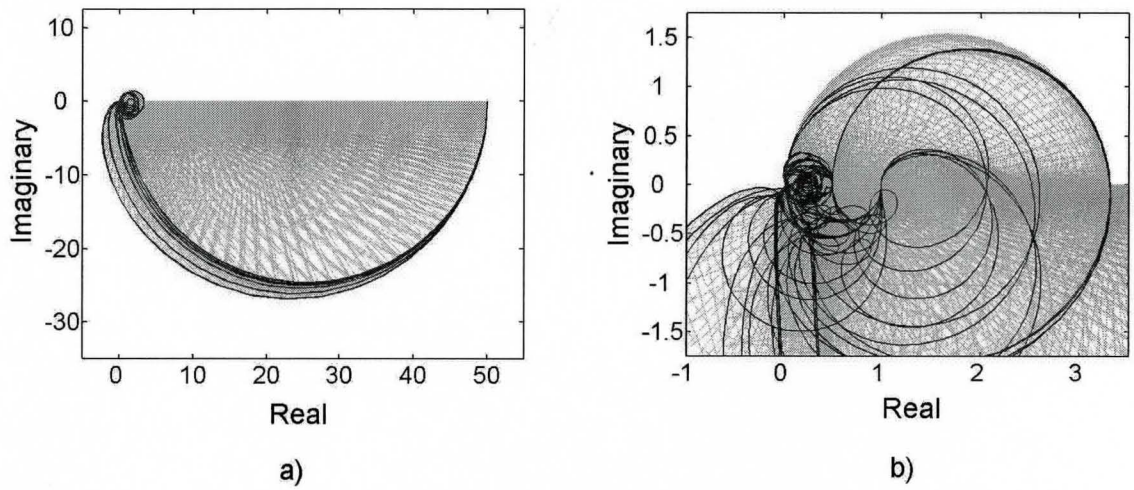

Figure 4.11: Nyquist envelope of of $G(j\omega)$ and Nyquists of $G_V^{i,k}(j\omega)$ a) entire envelope b) zoom-in. Note: the dark lines are the extremal plants.

This chapter is concluded by remarking that although only systems with real coefficient interval polynomials have been discussed many of the concepts can be extended and generalized to include complex coefficient interval polynomials. The reader is referred to [48] for a book length treatment on interval systems.

Chapter 5

Stability of Lur'e-Postnikov Systems

The Lur'e-Postnikov problem, known more simply as the Lur'e problem, is a classical control problem first formulated in 1944 [53]. It is concerned with the stability of closed-loop systems composed of a linear plant following by a non-linear feedback element. A Single-Input-Single-Output (SISO) example of such a system is shown in Fig. 5.1 where $G(s)$ is a LTI plant and $\Phi(\cdot)$ a nonlinear feedback element. An attractive approach to deduce stability of such closed-loop systems is to make assumptions on the non-linear element and then analyze the linear part $G(s)$ using classical linear system methods.

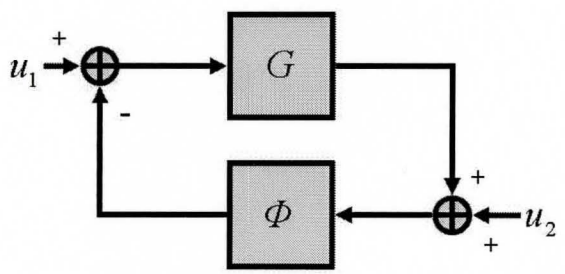

Figure 5.1: Lur'e-Postnikov block diagram

One of the early attempts to deduce stability of Lur'e systems was Aizerman's conjecture in 1949. It is first noted that a non-linear element $\Phi(\cdot)$ belongs to **sector** $[a, b]$, if the following holds:

$$a \leq \frac{\Phi(x,t)}{x} \leq b \tag{5.1}$$

Aizerman's conjecture was that if the feedback system is globally asymptotically stable for all constant linear feedback gains of the form $\Phi(x,t) = kx$ with $k \in [a, b]$, then the non-linear Lur'e-Postnikov system is stable for *all* time invariant nonlinear elements $\Phi(\cdot)$ in sector $[a, b]$. Unfortunately this conjecture is false in general.

In 1957 another conjecture was made by Kalman. Suppose $\Phi(\cdot)$ is a memoryless time-invariant and continuously differentiable nonlinearly that belongs to an **incremental sector** $[a, b]$, i.e.

$$\begin{aligned} &(i) \quad \Phi(0) = 0 \\ &(ii) \quad a \leq \frac{\Phi(x_1) - \Phi(x_2)}{x_1 - x_2} \leq b \end{aligned} \tag{5.2}$$

Kalman's conjecture is similiar to Aizerman's conjecture with the exception that the non-linear element $\Phi(\cdot)$ is memoryless and belongs to an incremental sector $[a, b]$. However, this conjecture is also false in general.

Although both conjectures are false, the notion of assuming sector or incremental sector restrictions on the nonlinear element are still useful for deriving stability conditions for Lur'e-Postnikov systems. The rest of the chapter will focus on various *sufficient* stability conditions assuming different restrictions on the non-linear feedback element.

5.1 Input-Output Passivity

Assuming the nonlinear feedback element $\Phi(x,t)$ is a first-third quadrant nonlinearity, i.e. belonging to sector $[0,\infty]$, input-output passivity theory can be used to show stability of the closed-loop system in Fig. 5.1. Before the relevant stability condition is stated some preliminaries on passivity theory will be discussed.

5.1.1 Passive and Strictly Passive Systems

The general idea behind input-output passivity is concerned with showing that the increase in stored energy in a system is less than or equal to the input energy, where the input energy can be defined by the input and output signals.

Consider a system with input u, output y, internal states x and non-negative energy function V that satisfies (5.3), where y^*u denotes external power. Such a system can only store, release or consume energy, it cannot produce it.

$$V(x(T)) - V(x(0)) \leq \int_0^T y^* u \, dt \tag{5.3}$$

Assuming $V(x(0)) = 0$ in (5.3) the following definitions can be realized for a system S with input u and output y [54] [55]:

The system S is **passive** from u to y if for all u and all $T > 0$:

$$\langle y, u \rangle_T \geq 0 \tag{5.4}$$

where

$$\langle y, u \rangle_T = \int_0^T y^* u \, dt \tag{5.5}$$

The system S is **strictly passive** from u to y if there exists $\epsilon > 0$ such that for all u and all $T > 0$:

$$\langle y, u\rangle_T \geq \epsilon(\langle y, y\rangle_T + \langle u, u\rangle_T) \tag{5.6}$$

A resistor is an example of a strictly passive component since it only consumes energy. Capacitors and inductors are examples of passive components since they only store and release energy.

A strictly passive system also has the property that it has finite L_2-gain, i.e. for a system with input u and output y, $\sup_{u\in L_2} \|y\|_2/\|u\|_2$ is finite [54].

Proof: Using (5.6), the Cauchy-Schwartz inequality $\langle y, u\rangle_T^2 \leq \langle y, y\rangle_T\langle u, u\rangle_T$ and $\|y\|_2 = \lim_{T\to\infty}\sqrt{\langle y, y\rangle_T}$ the following can be obtained

$$\epsilon(\langle y, y\rangle_T + \langle u, u\rangle_T) \leq \langle y, u\rangle_T \leq \sqrt{\langle y, y\rangle_T}\sqrt{\langle u, u\rangle_T} \leq \|y\|_2\|u\|_2 \tag{5.7}$$

Hence $\epsilon\langle y, y\rangle_T \leq \|y\|_2\|u\|_2$, letting $T \to \infty$ gives

$$\|y\|_2 \leq \frac{1}{\epsilon}\|u\|_2 \tag{5.8}$$

5.1.2 Passivity Stability Theorem

A feedback system, like the one illustrated in Fig. 5.2, that can be decomposed into two elements is closed-loop BIBO stable from $u = [u_1 \;\; u_2]^T$ to $y = [y_1 \;\; y_2]^T$ provided one element (eg. S_1) is strictly passive and the other (eg. S_2) is passive [56].

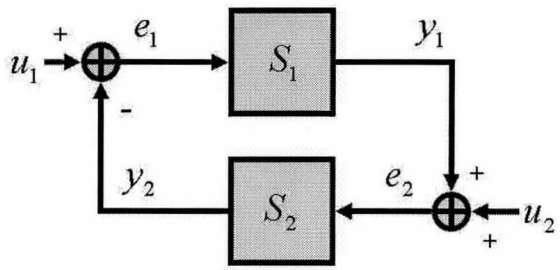

Figure 5.2: Passivity theorem block diagram.

Proof:S_1 strictly passive and S_2 passive give:

$$\epsilon(\langle y_1, y_1\rangle_T + \langle e_1, e_1\rangle_T) \leq \langle y, u\rangle_T \tag{5.9}$$

where

$$\begin{aligned} \langle y, u\rangle_T &= \langle y_1, u_1\rangle_T + \langle y_2, u_2\rangle_T \\ &= \langle y_1, u_1 - y_2\rangle_T + \langle y_2, u_2 + y_1\rangle_T \\ &= \langle y_1, e_1\rangle_T + \langle y_2, e_2\rangle_T \end{aligned} \tag{5.10}$$

Substituting $e_1 = u_1 - y_2$ in (5.9) yields

$$\langle y_1, y_1\rangle_T + \langle y_2, y_2\rangle_T + \langle u_1, u_1\rangle_T \leq 2\langle y_2, u_2\rangle_T + \frac{1}{\epsilon}\langle y, u\rangle_T \tag{5.11}$$

Using Cauchy Schwartz inequality and $\langle y_2, y_2\rangle\langle u_2, u_2\rangle \leq \langle y, y\rangle\langle u, u\rangle$ leads to

$$\langle y, y\rangle_T \leq 2\langle y_2, u_2\rangle_T + \frac{1}{\epsilon}\langle y, u\rangle_T \leq \left(2 + \frac{1}{\epsilon}\right)\sqrt{\langle y, y\rangle_T}\sqrt{\langle u, u\rangle_T} \tag{5.12}$$

Finally letting $T \to \infty$ gives $\|y\|_2 \leq \left(2 + \frac{1}{\epsilon}\right)\|u\|_2$ and the theorem is proven.

Returning to the Lur'e-Postnikov problem in Fig. 5.1, a first-third quadrant non-linear feedback element in sector $[0, \infty]$ is passive since $x\Phi(x,t) \geq 0$. Stability is thus achieved provided the linear part $G(s)$ is a strictly passive system. Note this is only a *sufficient* stability condition.

5.1.3 Passivity of Linear Systems

A stable linear transfer function $G(s)$ is passive if and only if it is **positive real** (PR) [25] i.e.

$$\text{Re}[G(j\omega)] \geq 0, \quad \forall\omega > 0 \tag{5.13}$$

This is equivalent to stating that phase of $G(s)$ is in the range of $-\pi/2$ and $\pi/2$.

Proof: Assuming $G(s)$ is passive its output is y , its input is u where $u(t) = 0$ when $t \notin [0, T]$ the following is obtained using Parseval's Theorem.

$$0 \leq \int_0^T y(t)u(t)\,dt = \int_\infty^\infty y(t)u(t)\,dt = \frac{1}{2\pi}\int_\infty^\infty Y(j\omega)U^*(j\omega)\,d\omega \tag{5.14}$$

Since $Y(j\omega) = G(j\omega)U(j\omega)$ and $G(s)$ is a transfer function of a real system it follows that

$$0 \leq \frac{1}{\pi}\int_0^\infty \text{Re}[G(j\omega)]|U(j\omega)|^2\,d\omega \tag{5.15}$$

This equality holds provided that $\text{Re}[G(j\omega)] \geq 0$, which is both a necessary and sufficient condition.

A stable linear transfer function $G(s)$ is strictly passive or dissipative if and only if it is **strictly positive real** (SPR) [25] i.e.

$$\text{Re}[G(j\omega)] > 0, \quad \forall\omega > 0 \tag{5.16}$$

The proof is similar to the previous case where the strict passivity property of $\epsilon \int_0^T u(t)u(t)\,dt \leq \int_0^T y(t)u(t)\,dt$ with $\epsilon > 0$ replaces the leftmost inequality in (5.14).

Using the theorem stated in the previous section with stable linear systems leads to a small phase condition. That is a combination of a passive linear system with a strictly passive one have combined phase that is always between $\pm\pi$, hence stability is assured.

5.2 On-Axis Circle Theorem

By placing finite sector restrictions on the nonlinear feedback element $\Phi(x,t)$ an application of the small gain theorem can lead to stability conditions on $G(s)$ that are more relaxed than strict passivity of $G(s)$.

5.2.1 Small Gain Approach

Consider $\Phi(x,t)$ to be in sector $[-r,r]$ and $G(s)$ a stable transfer function, then stability of Fig. 5.1 via the small gain theorem is assured if [55]

$$\sup_{\omega\in\Re} |G(j\omega)| < \tfrac{1}{r} \tag{5.17}$$

The condition in (5.17) is satisfies if the Nyquist plot of $G(s)$ is inside a circle with centre at the origin that has radius $\frac{1}{r}$. More useful conditions can be obtained by allowing arbitrary sectors on $\Phi(x,t)$. Using a loop transformation discussed in the next section leads to the well known on-axis circle criterion [55] [57].

5.2.2 Loop transformation

Assume $\Phi(x,t)$ lies in an arbitrary sector $[a,b]$, where $b > a$ and define

$$K = \frac{a+b}{2}, \quad R = \frac{b-a}{2} \tag{5.18}$$

The loop transformation shown in Fig. 5.3a) allows the small gain theorem to be used on the system shown in Fig. 5.3b) where the inputs retain their boundedness and the feedback element $[\Phi(x,t) - K]$ is in sector $[-R, R]$.

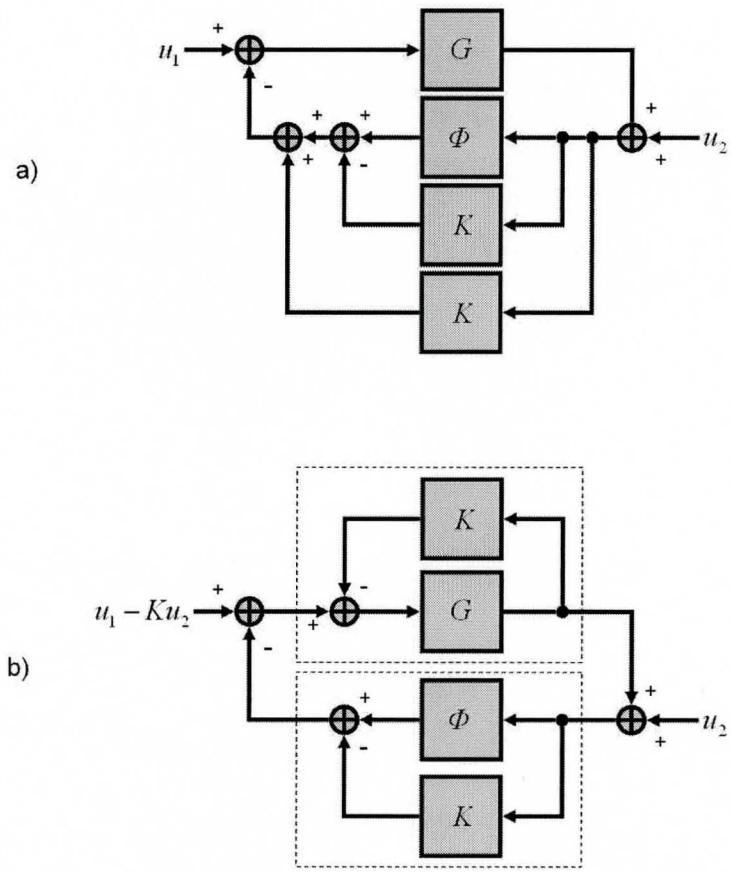

Figure 5.3: On-axis circle theorem loop transformation.

Applying the small gain theorem to Fig. 5.3b) stability is assured if $\frac{G(s)}{1+KG(s)}$ is stable and

$$\sup_{\omega\in\Re} |\frac{G(j\omega)}{1+KG(j\omega)}| < \frac{1}{R} \tag{5.19}$$

Expression (5.19) is equivalent to

$$R < \inf_{\omega\in\Re} |\frac{1}{G(j\omega)} + K| \tag{5.20}$$

Which is geometrically equivalent to the Nyquist plot of $\frac{1}{G(j\omega)}$ being bound away from a circle defined by $\{z \in C : |z+K| \leq R\}$. Transforming (5.20) through $z \mapsto 1/z$ yields that the Nyquist plot of $G(j\omega)$, for $ab > 0$, must be bounded away from the circle $\{z \in C : |z+\frac{b+a}{2ab}| \leq \frac{b-a}{2ab}\}$ which intersects the real axis at $-1/a$ and $-1/b$. This transformation is illustrated in Fig. 5.4. For $a < 0 < b$ the Nyquist plot of $G(j\omega)$ must be contained in the circle $\{z \in C : |z+\frac{b+a}{2ab}| \leq \frac{b-a}{2ab}\}$. Assuming $0 = a < b$ yields $\inf_{\omega\in\Re} \mathrm{Re}[G(j\omega)] > -\frac{1}{b}$ as the stability condition which is less restrictive than (5.16). In all cases $-1/K$ is also bounded away from $G(j\omega)$ thus $\frac{G(j\omega)}{1+KG(j\omega)}$ is stable if $G(s)$ is stable. Although it has been stated that $G(s)$ is open-loop stable the circle theorem can be extended to handle unstable plants, e.g. the reader is referred to [55].

Using the results of this section the on-axis circle theorem can be stated as follows. For open-loop stable $G(s)$ with non-linear dynamic feedback $\Phi(x,t)$ in sector $[a,b]$, $b > a > 0$, closed loop stability is assured if the Nyquist plot of $G(j\omega)$ is bounded away and does not encircle a disk that is centered on the real axis and intersects it at $-1/a$ and $-1/b$ [55].

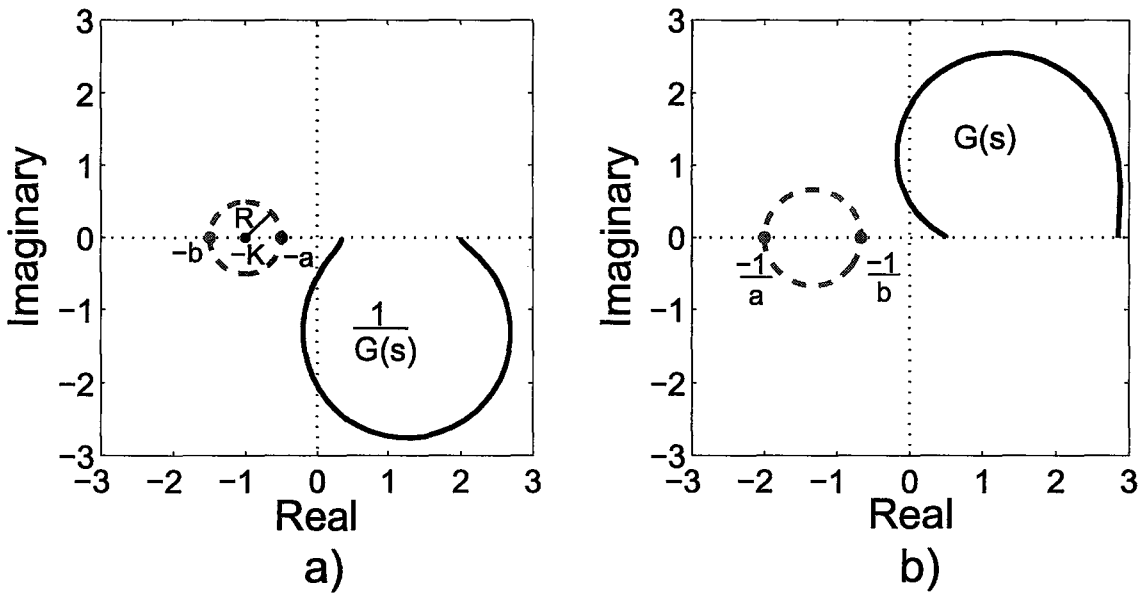

Figure 5.4: On-axis circle theorem test a) graphical interpretation of equation (5.20) b) transformed through $z \mapsto 1/z$. Here $G(s) = \frac{s^2+6s+100}{0.35s^2+8s+200}$, $a = 0.5$ and $b = 1.5$.

5.3 Off-Axis Circle Theorem

The stability conditions on $G(s)$ can be further relaxed if the non-linear feedback element $\Phi(\cdot)$ is assumed to be memoryless, continuous and in an incremental sector $[k_1, k_2]$, meaning it is a static non-linearity with a bounded derivative. By revisiting passivity theory with the aid of a multiplier concept, the off-axis circle theorem [58] can be derived. This theorem applies to static non-linear elements that lie in an arbitrary incremental sector $[k_1, k_2]$, where $k_2 > k_1$. If $k_2 > k_1 > 0$ the non-linear element becomes monotonic.

5.3.1 Passivity with Multipliers

The multiplier approach transforms the Lur'e-Postnikov problem to the form shown in either Fig. 5.5a) or b). Stability is then shown, via passivity stability theorem, by ensuring $G(s)Z(s)$ is strictly passive and either ΦZ^{-1} or $Z^{-1}\Phi$ is passive. Since the inverse of a passive operator is passive, $Z^{-1}\Phi$ and $\Phi^{-1}Z$ are equivalently passive. To ensure boundedness of inputs Zu_2 and $Z^{-1}u_1$ the multiplier $Z(s)$ is typically chosen to be a transfer function where the order of the numerator is the same as the denominator.

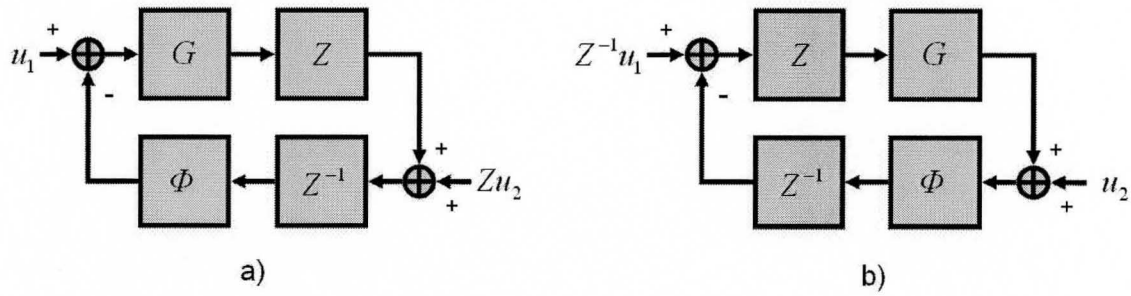

Figure 5.5: Lur'e-Postnikov problem with multipliers

In deriving the off-axis circle theorem the multiplier $Z(s)$ is chosen to have the following form [58]

$$Z(s) = \prod_{n=0}^{N} \frac{s + \alpha_n}{s + \beta_b} \tag{5.21}$$

where

$$0 < \alpha_0 < \beta_0 < \alpha_1 < \beta_1 < \ldots \tag{5.22}$$

or

$$0 < \beta_0 < \alpha_0 < \beta_1 < \alpha_1 < \ldots \tag{5.23}$$

The multiplier given in (5.21) is composed of alternating poles and zeros on the negative real axis. If (5.22) holds then $Z(s)$ is said to be in RL, that is it can be made up of a network of resistors and inductors [59]. An RC network results for $Z(s)$ if (5.23) holds [59]. Note if $Z(s)$ in RC then $Z^{-1}(s)$ in RL and vice versa [59]. The notation Z_{RL} and Z_{RC} will be utilized to denote whether $Z(s)$ is in RL or RC.

Consider a memoryless non-linearity $\Phi(\cdot)$ that belongs to the incremental sector $[0, \infty]$, i.e. a monotonic static incrementally positive function. If $G(s)Z(s)$ is SPR, where $Z(s)$ is defined in (5.21) and assuming either (5.22) or (5.23) then the feedback system is stable.

Proof:

Note the following proof has been developed by the thesis author since it is not explicitly given in [58].

Case a) $0 < \alpha_0 < \beta_0 < \alpha_1 < \beta_1 < ...$

Here $Z \in Z_{RL}$ and $Z^{-1} \in Z_{RC}$ and using Fig. 5.5a) passivity of ΦZ^{-1} assures stability. To show passivity of ΦZ^{-1}, the multiplier Z^{-1} must first be rewritten in its RC Foster expansion form [59]. This is done by performing a partial fractions expansion on the inverse of (5.21)

$$Z^{-1}(s) = 1 + \sum_{n=0}^{N} \frac{\lambda_n}{s + \sigma_n}, \quad \lambda_n \geq 0, \sigma_n > 0 \tag{5.24}$$

It can be shown that (5.24) followed by an incrementally positive $\Phi(\cdot)$ yields passive ΦZ^{-1}. The proof is lengthy and technical thus the reader is referred to Lemma 3a of [57].

Case b) $0 < \beta_0 < \alpha_0 < \beta_1 < \alpha_1 < ...$

Here $Z \in Z_{RC}$ and $Z^{-1} \in Z_{RL}$ and using Fig. 5.5b) passivity of $Z^{-1}\Phi$ assures

stability. Since $Z^{-1}\Phi$ and $\Phi^{-1}Z$ are equivalently passive, $\Phi(\cdot)^{-1}$ also incrementally positive, and $Z(s)$ able to take the form shown in (5.24), Lemma 3a of [57] is again utilized to show passivity of $\Phi^{-1}Z$ and futhermore system stability.

Alternatively using Fig. 5.5a) it can also be shown that a combination of a Z_{RL} operator followed by an incrementally positive operator $\Phi(\cdot)$ is also passive [60].

The previously stated theorem is useful if it is easy to show that for a given $G(s)$, a multiplier $Z(s)$ of the form (5.21) exists such that $G(s)Z(s)$ is SPR. Such a multiplier of the form (5.21) has been proven to exist provided the Nyquist plot of $G(j\omega)$ is to the right of a line that passes through the origin [58]. For a detailed explanation of the proof see [58]. A heuristic explanation is given as follows.

Assume the Nyquist plot of $G(j\omega)$ is to the right of a line that passes through the origin making an angle θ with the imaginary axis, therefore the following inequality is obtained.

$$-\frac{\pi}{2} - \theta < \arg(G(j\omega)) < \frac{\pi}{2} - \theta \tag{5.25}$$

For a given frequency range $\omega \in [\omega_a, \omega_b]$, positive constants ϵ_1 and ϵ_2 exist such that

$$-\frac{\pi}{2} + \epsilon_1 < \arg(G(j\omega)) + \theta < \frac{\pi}{2} - \epsilon_2 \tag{5.26}$$

Using Lemma 1 of [58] yields a $Z \in Z_{RL}$, for $0 < \theta < \frac{\pi}{2}$, or a $Z \in Z_{RC}$, for $-\frac{\pi}{2} < \theta < 0$, such that

$$|\arg(Z(j\omega)) - \theta| \leq \epsilon, \quad \omega \in [\omega_a, \omega_b] \tag{5.27}$$

where $0 < \epsilon < \min(\epsilon_1, \epsilon_2)$. Combining (5.26) and (5.27) yields (5.28) and futhermore

strict-passivity of $G(s)Z(s)$.

$$-\frac{\pi}{2} < -\frac{\pi}{2} + \epsilon_1 - \epsilon \leq \arg(G(j\omega)Z(j\omega)) \leq \frac{\pi}{2} - \epsilon_2 + \epsilon < \frac{\pi}{2}. \tag{5.28}$$

The multiplier acts by providing the necessary phase lead ($Z \in Z_{RL}$) or lag ($Z \in Z_{RL}$) in the frequency range $\omega \in [\omega_a, \omega_b]$ to ensure $G(s)Z(s)$ is SPR.

Using the results of this section one is able to conclude the following about a Lur'e-Postinikov problem. If $\Phi(\cdot)$ is a memoryless monotonic non-linearity in incremental sector $[0, \infty]$ and the Nyquist plot of $G(s)$ is to the right of a line that passes through the origin, then the closed loop feedback system is stable.

The theorem can be extended to arbitrary incremental sectors by performing the loop transformations shown in the next section.

5.3.2 Loop Transformations

Assume the feedback element $\Phi(\cdot)$ lies in incremental sector $[0, k_2]$, $k_2 > 0$, and the Nyquist plot of $G(s)$ is to the right of a line that passes through the point $-\frac{1}{k_2}$. The loop transformation in Fig. 5.6a) yields a new feedback system in Fig. 5.6b) with bounded inputs, plant $G_b(s) = G(s) + \frac{1}{k_2}$ and feedback $\Phi_b(\cdot)$ denoted by the dashed box. Looking at the *output-to-input* relationship of $\Phi_b(\cdot)$, $\Phi^{-1}(\cdot)$ is in incremental sector $[-\frac{1}{k_2}, \infty]$, thus $\Phi_b^{-1}(\cdot)$ and $\Phi_b(\cdot)$ are both in incremental sectors $[0, \infty]$. Since the Nyquist plot of $G_b(j\omega)$ is to the right of a line that passes through the origin the results of the previous section show stability.

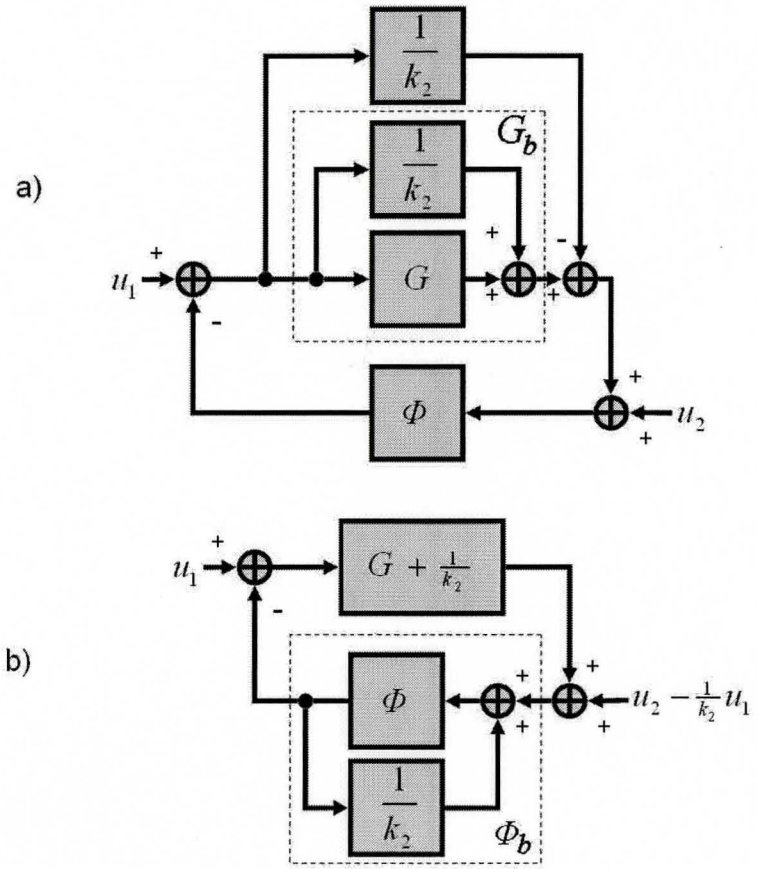

Figure 5.6: Incremental sector $[0, k_2]$ loop transformation.

For an arbitrary incremental sector $[k_1, k_2]$, $k_2 > k_1$, an additional loop transformation shown in Fig. 5.7a) is performed to yield the bounded input system in Fig. 5.7b). Here $\Phi_b(\cdot)$ is denoted by the dashed box in Fig. 5.7a), in Fig. 5.7b) $\Phi_c(\cdot)$ represents the lower dashed box and $G_c(s)$ represents the upper dashed box. Since $\Phi^{-1}(\cdot)$ is in incremental sector $[\frac{1}{k_2}, \frac{1}{k_1}]$, $\Phi_b(\cdot)$ can be shown to be in incremental sector $[\frac{k_1 k_2}{k_2 - k_1}, \infty]$ and furthermore $\Phi_c(\cdot)$ in incremental sector $[0, \infty]$.

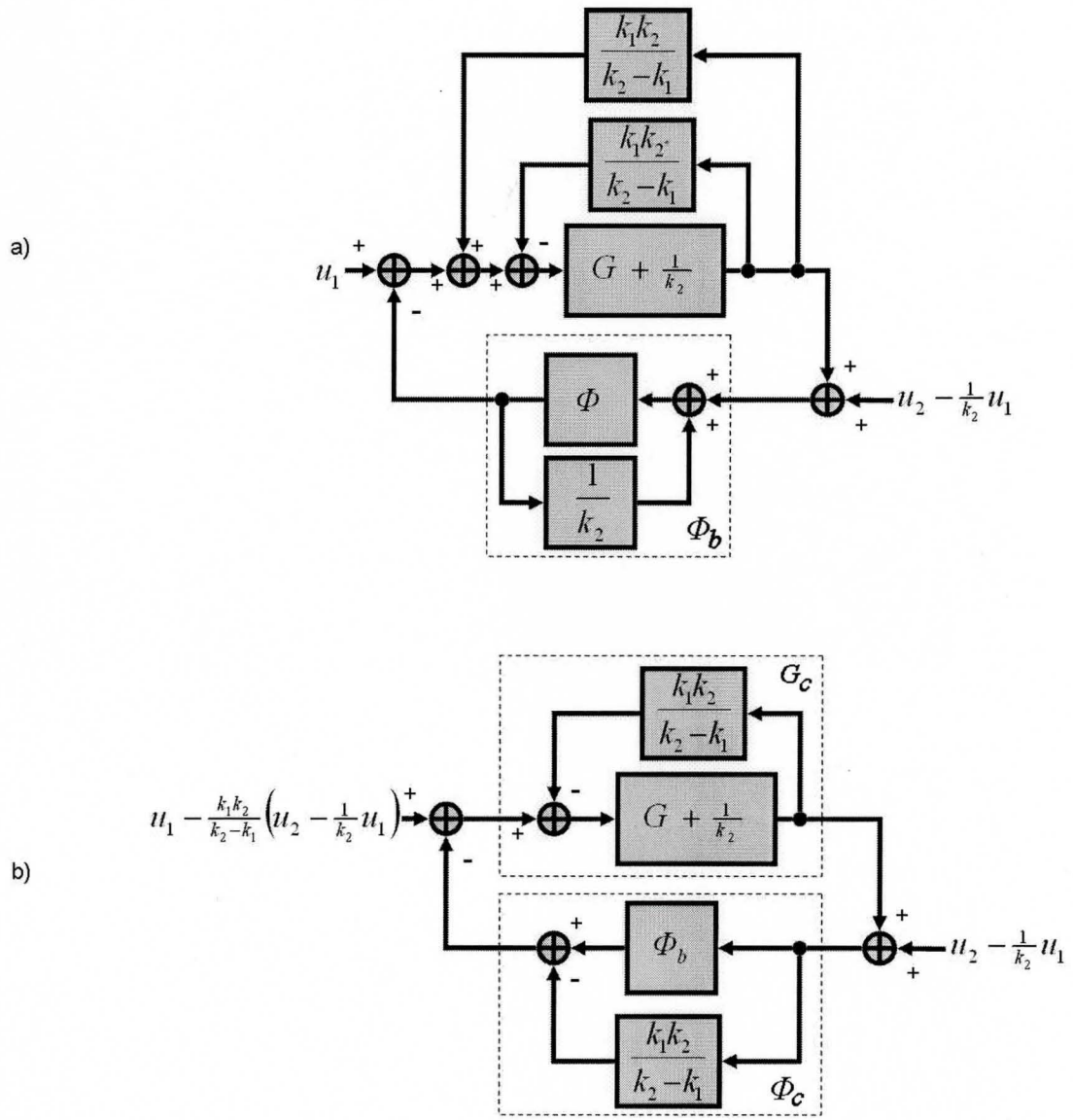

Figure 5.7: Incremental sector $[k_1, k_2]$ loop transformation.

Note that $G_c(s)$ can be represented as

$$G_c(s) = \frac{k_2 - k_1}{k_2^2} \cdot \frac{k_2 G(s) + 1}{k_1 G(s) + 1} = \frac{k_2}{1 + k_2 G(s)} + \frac{k_1 k_2}{k_2 - k_1} \tag{5.29}$$

The transformation defined in (5.29) operates such that, for $k_1 < 0 < k_2$, a Nyquist plot of $G(j\omega)$ that is contained in an off-axis circle touching the real axis at $-\frac{1}{k_1}$ and $-\frac{1}{k_1}$ results in the Nyquist plot of $G_c(s)$ to be to the right of a line intersecting the origin [58]. For $0 < k_1 < k_2$, the Nyquist plot of $G(s)$ must be bounded away from the off-axis circle. Like before, stability is proven using the arguments of the previous section. Since the centre of the off-axis circle is not restricted, infinitely many different off-axis circles can be formed given a specific k_1 and k_2.

Finally one can conclude the needed off-axis circle theorem for the nonlinear Lur'e-Postinikov problem. For open-loop stable $G(s)$ with memoryless non-linear feedback $\Phi(\cdot)$ belonging to incremental sector $[k_1, k_2]$, closed-loop stability is assured provided, for $0 < k_1 < k_2$, the Nyquist plot of $G(j\omega)$ is bounded away and does not encircle an off-axis circle that intersects the real axis at $-\frac{1}{k_1}$ and $-\frac{1}{k_1}$ [58]. A graphical example is shown in Fig. 6.1

5.4 Other Methods

Researching Lur'e-Postinikov problems one finds the scientific literature is rich in content. Therefore this chapter is concluded by briefly mentioning other potentially useful methods.

The well known Popov criterion [55] is suited for showing stability with memoryless time-invariant nonlinearities belonging to sector $[0, b]$. It is based on a passivity with multipliers approach and has a corresponding graphical test to show stability for a given $G(s)$. The graphical test is based on the Popov plot, a graph of $\mathrm{Re}(G(j\omega))$ versus $\omega\mathrm{Im}(G(j\omega))$. Stability is shown when the Popov plot is to the right of a line intersecting $-\frac{1}{b}$. The nonlinearity $\Phi(\cdot)$ need not be monotonic, however it must has lower sector equal to zero. Another limitation is that the Popov criterion is limited to strictly proper plants for $G(s)$ and also requires the derivative of the input to be bounded.

Another result obtained by Narendra and Cho applies to static odd-monotonic nonlinearities [61]. It is also a passivity with multipliers approach where it is shown that a specific multiplier $Z_{odd}(s)$ preserves passivity when combined with a static odd-monotonic function in incremental sector $[0, \infty]$. However there is no graphical test or systematic way to show that for a specific plant $G(s)$, there exists a $Z_{odd}(s)$ such that $G(s)Z_{odd}(s)$ is SPR hence the theorem is difficult to apply in practice.

More recently Materassi et al. have proposed that the on-axis circle criterion can be relaxed to include static hyperbolic type sector non-linearities [62]. Stability is shown using a Lyapunov-based argument to show the closed-loop system is globally bounded. However strict properness of the linear part $G(s)$ is required.

Finally it is noted that the stability conditions presented in this chapter are only sufficient and not necessary.

Chapter 6

Teleoperation Stability Analysis

The theory presented in the previous two chapters will be utilized to perform a stability analysis on the teleoperation block diagram that concluded chapter three. Different types of generalized tranparency objectives are considered in this chapter. The first section presents stability conditions assuming simple first-order force filtering with static non-linear scaling of either force or position. Stability is analyzed using a combination of an off-axis circle criterion with the Nyquist envelope of interval plants systems obtained by using Kharitonov plants [63]. The second section focuses on LTI filtered mappings of position and force where the exact stability regions are obtained by analyzing the closed-loop characteristic equation. The third section considers combinations of mixed non-linear/LTI filtered mappings where stability is shown utilizing the off-axis circle criterion with the Nyquist envelope of interval polytopic plants. The final section shows that reformulating the off-axis circle criterion to be utilized with bode envelopes as explained in [64] is a more conservative approach when compared to using Nyquist envelopes.

6.1 Static Nonlinear Feedback

It is possible to convert the teleoperation block diagram in Fig. 3.1b) to a nonlinear Lur'e-Postnikov type problem shown in Fig. 5.1 by assuming that one of the two mappings is linear, i.e. by considering linear position/nonlinear force or nonlinear position/linear force scaling combinations. Furthermore, assuming force filters $H_{fh} = H_{fe} = \frac{C}{s+C}$ and position filters $H'_{xm} = H'_{xs} = 1$, the linear part would reduce to

$$G(s) = \frac{m_1 s^2 + b_1 s + k_1}{m_2 s^2 + b_2 s + k_2} = \frac{\mathcal{Z}_e}{\mathcal{Z}_h + \mathcal{Z}_t} \tag{6.1}$$

with the nonlinear feedback element

$$\Phi(\cdot) = \begin{cases} \kappa_f(\cdot)\kappa_p^{-1} & \kappa_p(\cdot) \text{ linear} \\ \kappa_p^{-1}(\cdot)\kappa_f & \kappa_f(\cdot) \text{ linear} \end{cases} \tag{6.2}$$

and an exogenous inputs $u_2 = 0$ and $u_1 \in L_\infty$ defined as

$$u_1 = \begin{cases} \tilde{F}_h^* - \bar{\rho} - \frac{\mathcal{Z}_h + \mathcal{Z}_t}{1+C^{-1}s}\rho_e & , \kappa_p(\cdot) \text{ linear} \\ \frac{-F_h^*}{\kappa_f \mathcal{Z}_e} + \frac{1+C^{-1}s}{\kappa_f \mathcal{Z}_e}\bar{\rho} + \frac{\mathcal{Z}_h + \mathcal{Z}_t}{\kappa_f \mathcal{Z}_e}\rho_e & , \kappa_f(\cdot) \text{ linear} \end{cases} \tag{6.3}$$

where $m_1 \geq 0$, $b_1 \geq 0$, $k_1 \geq 0$ represent environment impedance parameters and $m_2 = m_h + m_t > 0$, $b_2 = b_h + b_t > 0$, $k_2 \geq 0$ represent the combined impedance parameters of the hand and virtual tool.

6.1.1 Passivity approach

Assuming the non-linear element $\Phi(\cdot)$ is passive, for example first-third quadrant non-linearities which satisfy $x\Phi(x) \geq 0$, the passivity theorem presented in section

5.1.2 can be used. This leads to a sufficient stability condition of strict positive realness of the linear part (6.1), i.e.

$$\inf_{\omega \in \Re} \mathrm{Re}\left(\frac{-m_1\omega^2 + b_1 j\omega + k_1}{-m_2\omega^2 + b_2 j\omega + k_2}\right) > 0 \tag{6.4}$$

The condition in (6.4) is shown in Appendix A.1 to be equivalent to

$$b_1 b_2 > \left(\sqrt{m_1 k_2} - \sqrt{m_2 k_1}\right)^2 \tag{6.5}$$

which must be satisfied for all possible combinations of hand and environment parameters. In practice, allowing all possible environment and hand impedances results in large perturbations in $G(s)$ making stability, if possible, challenging to guarantee. However, it is reasonable to limit the parameters to some known ranges that can be determined based on the application. In Table 6.1, a hypothetical example of such bounds for soft-tissue telemanipulation is given. The ranges in Table 6.1 are comparable to those found in [35] and [36].

Table 6.1: Parameter Ranges for Hand and Environment

	Mass (kg)	Damping (Nsm^{-1})	Stiffness (Nm^{-1})
$\mathcal{Z}_e$	0.01–0.2	5–50	10-1000
$\mathcal{Z}_h$	0-0.3	0–100	20-1000

Using (6.5) and (6.1) with a desired hypothetical virtual tool mass of $m_t = 0.4$ kg, and the data in Table 6.1, the minimum level of virtual tool damping needed for $G(s)$ to be SPR is $b_t > \frac{1}{5}\left(\sqrt{0.01(20)} - \sqrt{0.7(1000)}\right)^2 = 135\ Nsm^{-1}$. Assuming negligible tool mass, $m_t \approx 0$, yields $b_t > 57\ Nsm^{-1}$. Clearly such levels of

tool damping can result in extremely sluggish system response and degrade the fidelity of soft-tissue telemanipulation. Due to the rather excessive conservatism of the passivity-based condition, alternative stability conditions must be considered.

6.1.2 Circle criterions with Nyquist envelope

The on/off axis circle criterions [55,58] presented in the previous chapter can produce a far less conservative sufficient stability condition at the expense of more restriction on the nonlinear element. The on-axis criterion assumes that the nonlinear mapping $\Phi(\cdot)$ belongs to a *sector*, see (5.1), whereas the off-axis criterion assumes $\Phi(\cdot)$ belongs to an *incremental sector*, see (5.2). Note that if $\Phi(\cdot)$ lies in incremental sector $[a, b]$ it lies in sector $[k_1, k_2]$, where $k_1 \geq a$ and $k_2 \leq b$, hence the on-axis criterion can also be applied to incremental sector nonlinearities. Assuming incremental sector $[a, b]$ with $b > a > 0$ yields $\Phi(\cdot)$ to be monotonic. Both circle criterions conclude stability if the Nyquist plot of the linear part is outside of a circle which intersects the negative real axis at $-\frac{1}{a}$ and $-\frac{1}{b}$. Since the on-axis test requires the circle to have its centre on the real axis, the off-axis criterion yields a larger incremental sector range $[a, b]$, as shown in Fig. 6.1.

Using a transformation that maps an off-axis circle to the imaginary axis a numerical stability test can be obtained. Using the following transformation

$$\begin{aligned} H(s) &= \frac{G(s) + \frac{1}{2}(\frac{1}{a} + \frac{1}{b}) - dj - r}{G(s) + \frac{1}{2}(\frac{1}{a} + \frac{1}{b}) - dj + r} \\ r &= \sqrt{d^2 + \frac{1}{4}\left(\frac{1}{a} - \frac{1}{b}\right)^2}, d \in \Re \end{aligned} \tag{6.6}$$

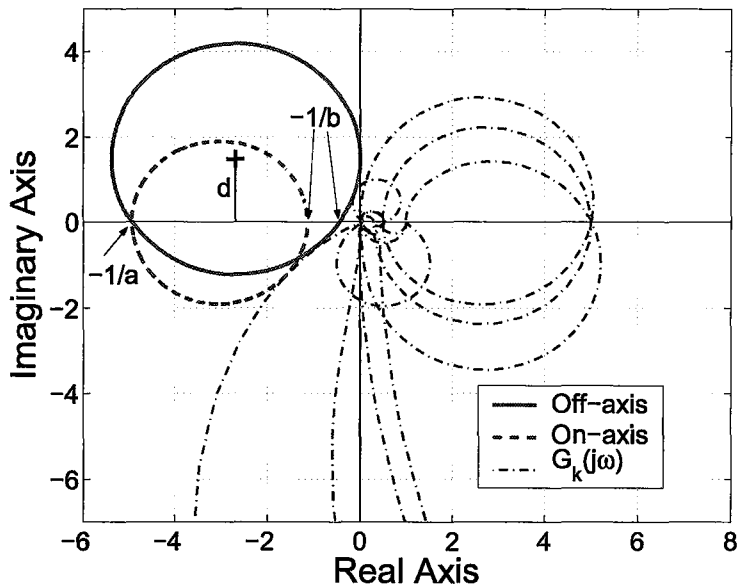

Figure 6.1: The off-axis vs. on-axis circle criterion test for a family of transfer functions.

where a, b and d specify a circle as in Fig. 6.1, the stability test can be restated as

$$\inf_{\omega \in \Re^+} \mathrm{Re}\,(H(j\omega)) > 0 \tag{6.7}$$

The condition in (6.7) states that the Nyquist plot of $G(s)$ does not enter a circle whose centre has imaginary component equal to d and intersects the real axis at $-\frac{1}{a}$ and $-\frac{1}{b}$, if and only if the real part of $H(j\omega)$ is positive for $\forall\omega \in \Re^+$. For this numerical test one only needs to find at least one value of d that satisfies (6.7) to show stability for a given a and b. For $d = 0$, (6.7) would reduce to the on-axis circle criterion which does not require monotonicity of $\Phi(\cdot)$ [55].

Notice that $G(s)$ in (6.1) is not a single transfer function but rather a family of transfer functions with independent real interval coefficients; thus $G(s)$ represents an interval plant system which can be represented by its Kharitonov plants $G_K(s)$

defined in (4.11) [3]. $H(s)$ in (6.6) is also an interval plant system whose coefficients may be complex and depend linearly on the coefficients of $G(s)$. To determine if (6.7) is satisfied for the interval system $H(s)$, it is sufficient to check if (6.7) is satisfied for the 16 Kharitonov plants $G_K(s)$. The proof of this lies in the fact that for $\omega \in \Re^+$ the outer Nyquist envelope of the interval system $G(s)$ can be found from the union of the Nyquist plots of $G_K(s)$, e.g. see section 4.2.2 [3]. Therefore if the Nyquist envelope of $G(s)$ lies outside the circle specified by a, b and d, then $\text{Re}(H(j\omega)) > 0$ for $\forall\omega \in \Re^+$. The benefit of using (6.7) is in that it is no longer a graphical test as is shown in Fig 6.1.

Given a, an upper value of b, $b \geq a$, can be found by searching through the two dimensional space of $b \in \Re^+$ and $d \in \Re$ using (6.7) as a stability constraint. This has been done using both the on-axis and off-axis circle criterions with the intervals specified in Table 6.1. Fig. 6.2 shows the results of such an analysis with the virtual tool parameters of $m_t = 0.4$ kg and $b_t = 10\ Nsm^{-1}$. Among the design parameters, the virtual tool damping has the biggest impact on the closed-loop stability. This can be observed in Fig. 6.3 where the stability margins derived from the off-axis circle criterion have increased at the expense of a higher tool damping.

It is observed in Fig 6.2 and Fig. 6.3 that for small values of lower incremental sector a, the upper incremental sector b plateaus. This corresponds to the case where the Nyquist envelope of (6.1) is to the right of a line that intersects the negative-real axis. For larger values of a, there a exists a critical value of a such that the Nyquist envelope of (6.1) is outside a circle that touches the origin. This case in turn corresponds to the Nyquist plot of $1/G(j\omega)$ being to the right of a line intersecting the negative real axis.

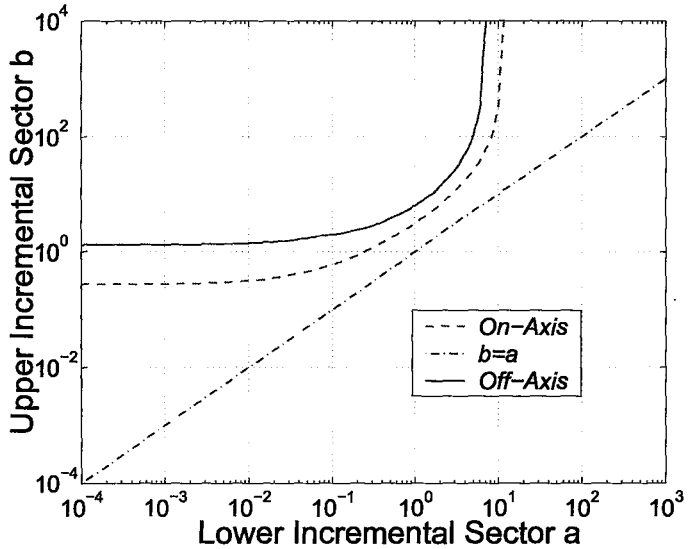

Figure 6.2: Off-axis vs. on-axis circle criterion: the stable region is between the straight and curved lines.

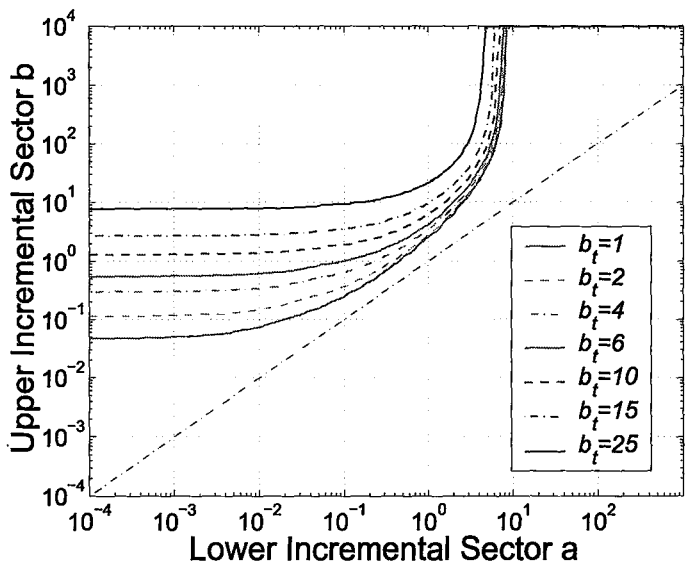

Figure 6.3: Stability regions obtained from the off-axis circle criterion for different values of virtual tool damping b_t.

When applying the test (6.7) for on-axis circles, where $d = 0$ in (6.6), the coefficients in $H(s)$ are all real. Therefore a stability analysis can be made more computationally efficient by using condition (6.5) with the sixteen transformed $H(s)$ plants. This eliminates the need of explicitly finding the Nyquist plots of $G_K(s)$. The off-axis stability analysis can be made more computationally efficient by using the results of an on-axis analysis as starting points for a maximum upper incremental sector search. One may also exploit monotonicity of the upper sector b curves to further increase computational efficiency. Monotonicity is expected since by fixing b and increasing a one makes the circle in Fig. 6.1 smaller.

6.2 LTI Filtered Mappings

Assuming linear scalings of force $\kappa_f(\cdot) = \kappa_f$ and position $\kappa_p(\cdot) = \kappa_p$, the teleoperation block diagram in Fig.3.1b) reduces to a linear system with plant (6.8) and unity feedback. Note $H_{Zt} = H'_{xm}(\frac{C}{s+C})\mathcal{Z}_t$.

$$G(s) = \frac{H'_{xm}}{H'_{xs}} \cdot \frac{H_{fe}\frac{k_f}{k_p}\mathcal{Z}_e}{H'_{xm}\frac{C}{s+C}\mathcal{Z}_t + H_{fh}\mathcal{Z}_h} \tag{6.8}$$

Furthermore the filters are assumed to be represented as LTI transfer functions with fixed numerator and denominator polynomials taking the form

$$H_{\sim}(s) = \frac{H^{\mathcal{N}}_{\sim}(s)}{H^{\mathcal{D}}_{\sim}(s)} \tag{6.9}$$

Thus the linear plant (6.8) is rewritten as

$$G(s) = \frac{H_{xm}^{\prime\mathcal{N}} H_{xs}^{\prime\mathcal{D}}}{H_{xm}^{\prime\mathcal{D}} H_{xs}^{\prime\mathcal{N}}} \cdot \frac{H_{xm}^{\prime\mathcal{D}} H_{fh}^{\mathcal{D}} H_{fe}^{\mathcal{N}} (C^{-1}s+1)\frac{k_f}{k_p}\mathcal{Z}_e}{H_{fh}^{\mathcal{D}} H_{fe}^{\mathcal{D}} H_{xm}^{\prime\mathcal{N}} \mathcal{Z}_t + H_{xm}^{\prime\mathcal{D}} H_{fe}^{\mathcal{D}} H_{fh}^{\mathcal{N}} (C^{-1}s+1)\mathcal{Z}_h} \tag{6.10}$$

The closed loop characteristic polynomial of $G(s)/[1+G(s)]$ is the following

$$C(s) = P_{Ze}(s)\frac{\kappa_f}{\kappa_p}\mathcal{Z}_e + P_{Zh}(s)\mathcal{Z}_h + P_{Zt}(s)\mathcal{Z}_t \tag{6.11}$$

$$P_{Ze}(s) = H_{fe}^{\mathcal{N}}(s) H_{fh}^{\mathcal{D}}(s) H_{xs}^{\prime\mathcal{D}}(s) H_{xm}^{\prime\mathcal{N}}(s)(C^{-1}s+1) \tag{6.12}$$

$$P_{Zh}(s) = H_{fe}^{\mathcal{D}}(s) H_{fh}^{\mathcal{N}}(s) H_{xs}^{\prime\mathcal{N}}(s) H_{xm}^{\prime\mathcal{D}}(s)(C^{-1}s+1) \tag{6.13}$$

$$P_{Zt}(s) = H_{fe}^{\mathcal{D}}(s) H_{fh}^{\mathcal{D}}(s) H_{xs}^{\prime\mathcal{N}}(s) H_{xm}^{\prime\mathcal{N}}(s) \tag{6.14}$$

The characteristic polynomial (6.11) can be rewritten to take the form below

$$C(s) = a_0(q) + a_1(q)s + \ldots + a_n(q)s^n \tag{6.15}$$

$$q = [m_e, b_e, k_e, m_h, b_h, k_h, m_t, b_t]^T \tag{6.16}$$

where the coefficients $a_i(q)$ depend linearly on q; the mass, spring, and damper parameters of $\mathcal{Z}_e$, $\mathcal{Z}_h$ and $\mathcal{Z}_t$. Assuming intervals on q results in (6.11) being a polytopic polynomial. Stability can then be shown using the origin exclusion tests described in section 4.1.2. Specifically the phase stability condition (4.10) can be utilized. A stability analysis was performed using three different sets of force/position filters with the intervals in Table 6.1, virtual tool mass of 0.4 kg, various fixed values of virtual tool damping and assuming force/position scaling such that $\frac{\kappa_f}{\kappa_p} = 1$.

Stability regions have been obtained by searching through the parameter space of the filters and obtaining binary images that show stable or potentially unstable regions. The potentially unstable regions involve at least one element in the interval family such that the teleoperation system would become unstable or marginally stable. By choosing various fixed values of virtual tool parameters only 2^6 vertex polynomials were required to perform the analysis. However the virtual tool parameters could also be chosen to lie in intervals, therefore 2^8 vertex polynomials would be required in such an analysis. It is also noted that when performing the computational analysis one must take care when discretizing the frequencies ω, since a coarse discretization may yield false stability regions. This occurs since an origin exclusion test between two frequency steps that would show potential instability is not performed. These false stability regions can manifiest themselves as jagged edges or ridges near the stable/potentially unstable boundary where a smooth continuous boundary may otherwise be expected.

6.2.1 Additional force filtering

The first set of filters used for stability analysis was additional second-order filtering of the force signals. This may be desired to remove unwanted sensor noise. The corresponding filters are

$$H'_{xm} = H'_{xs} = 1 \tag{6.17}$$

$$H_{fe} = H_{fh} = \frac{C}{s+C} \cdot \frac{\omega_n^2}{s^2+2\zeta\omega_n s+\omega_n^2} \tag{6.18}$$

The characteristic polynomial that determines stability in this cases is given by

$$C(s) = (\frac{1}{\omega_n^2}s^2 + 2\frac{\zeta}{\omega_n}s + 1)\mathcal{Z}_t + \mathcal{Z}_h + \mathcal{Z}_e \tag{6.19}$$

from which it is evident that the additional force filtering gives the virtual tool higher order dynamics. Stability regions have been graphed in Fig. 6.4 for various values of virtual tool damping and filter parameters. It should also be noted that assuming fixed virtual tool parameters results in the independence of the coefficients of the characteristic polynomial (6.19). Hence the stability can be investigated considering only the four Kharitonov polynomials given in (4.4).

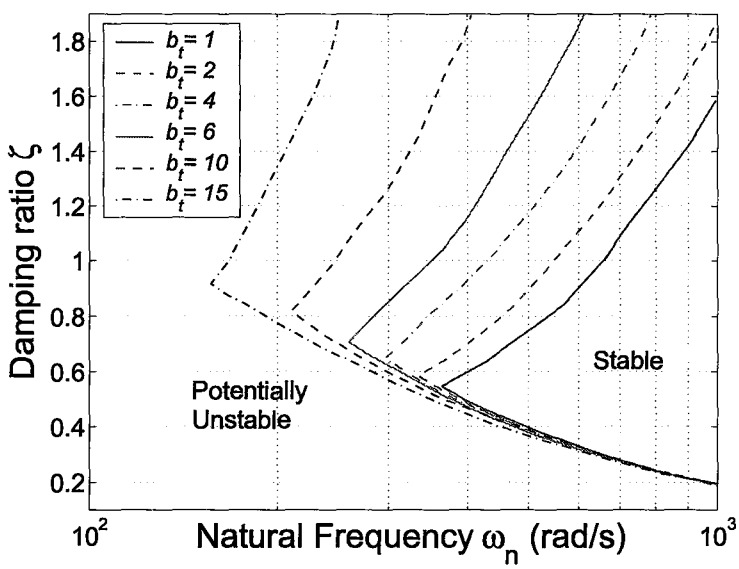

Figure 6.4: Additional second-order force filtering stability regions at different levels of virtual tool damping b_t.

6.2.2 Force compensator mapping

The second set of filters analyzed are

$$H'_{xm} = H'_{xs} = 1 \tag{6.20}$$

$$H_{fh} = \frac{C}{s+C} \tag{6.21}$$

$$H_{fe} = \frac{C}{s+C} \cdot \frac{\tau_1 s+1}{\tau_2 s+1} \tag{6.22}$$

where a force compensator mapping is used that amplifies or attenuates higher frequency environment forces, depending on the values of τ_1 and τ_2. The corresponding characteristic polynomial is given by

$$C(s) = (\tau_1 s + 1)\mathcal{Z}_e + (\tau_2 s + 1)(\mathcal{Z}_h + \mathcal{Z}_t) \tag{6.23}$$

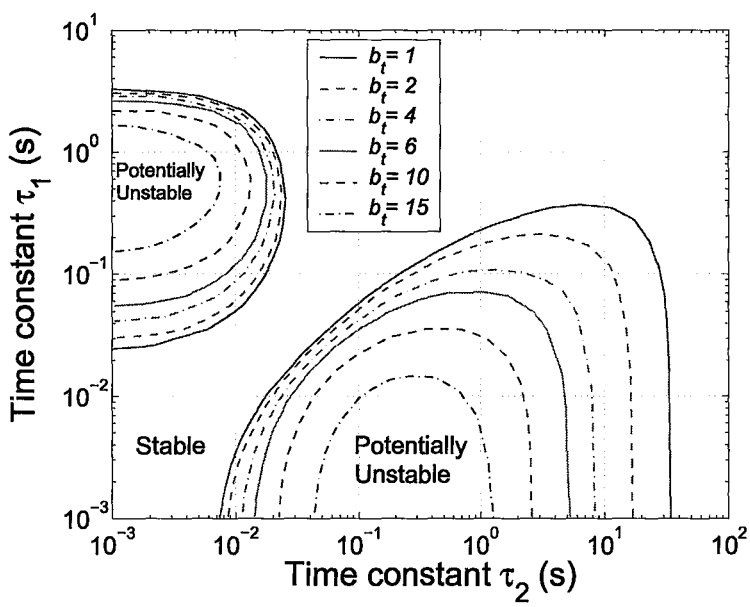

Figure 6.5: Force compensator filter stability regions at different levels of virtual tool damping b_t.

Stability regions are graphed in Fig. 6.5 where the area above the line $\tau_1 = \tau_2$ exhibits high pass behavior and the area below it has low pass behavior. The line $\tau_1 = \tau_2$ is guaranteed to be stable provided there exists damping in $\mathcal{Z}_e$, $\mathcal{Z}_h$ or $\mathcal{Z}_t$.

6.2.3 Hand tremor position filter

The last set of filters used for stability analysis are given by

$$H'_{xm} = 1 \tag{6.24}$$

$$H'_{xs} = 1 + \frac{(\frac{\omega_n}{Q_1} - \frac{\omega_n}{Q_2})s}{s^2 + \frac{\omega_n}{Q_2}s + \omega_n^2} = \frac{s^2 + \frac{\omega_n}{Q_1}s + \omega_n^2}{s^2 + \frac{\omega_n}{Q_2}s + \omega_n^2} \tag{6.25}$$

$$H_{fe} = H_{fh} = \frac{C}{s+C} \tag{6.26}$$

where a position notch type filter is used on the slave position. This type of filter can eliminate hand tremor without additional filtering of the virtual tool dynamics. This can be achieved by having the filter gain $\frac{Q_2}{Q_1} > 1$ at the tremor frequency ω_n. The magnitudes of Q_1 and Q_2 determine bandwidth of the filter as shown in Fig. 6.6. A smaller value of Q_1 results in larger filter bandwidth.

The resulting characteristic polynomial is

$$C(s) = (s^2 + \frac{\omega_n}{Q_2}s + \omega_n^2)\mathcal{Z}_e + (s^2 + \frac{\omega_n}{Q_1}s + \omega_n^2)(\mathcal{Z}_h + \mathcal{Z}_t) \tag{6.27}$$

Stability regions using this set of filters are plotted in Fig. 6.7 assuming $\omega_n = 20\pi$ rad/s. It should be noted that stability is expected when $Q_2 = Q_1$.

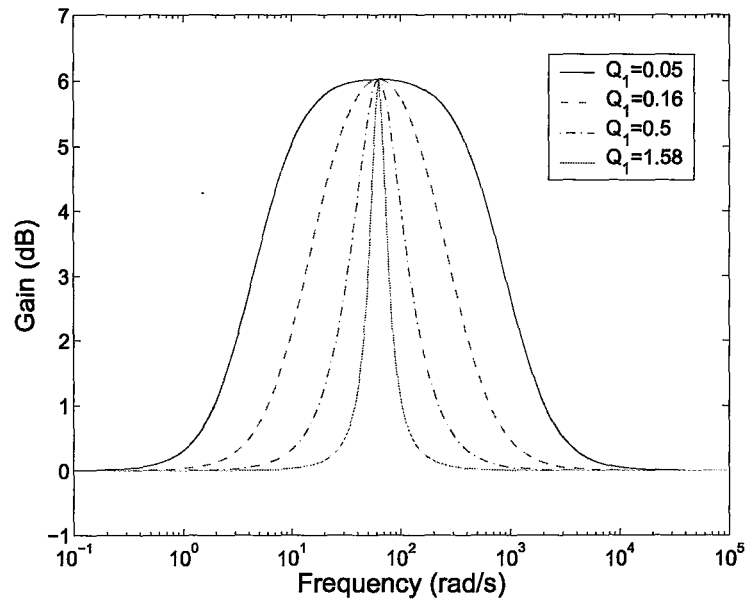

Figure 6.6: Position filter $H'_{xs} = (s^2 + \frac{\omega_n}{Q_1}s + \omega_n^2)/(s^2 + \frac{\omega_n}{Q_2}s + \omega_n^2)$ with $\omega_n = 20\pi$ rad/s, $Q_2 = 2Q_1$ at different values of Q_1.

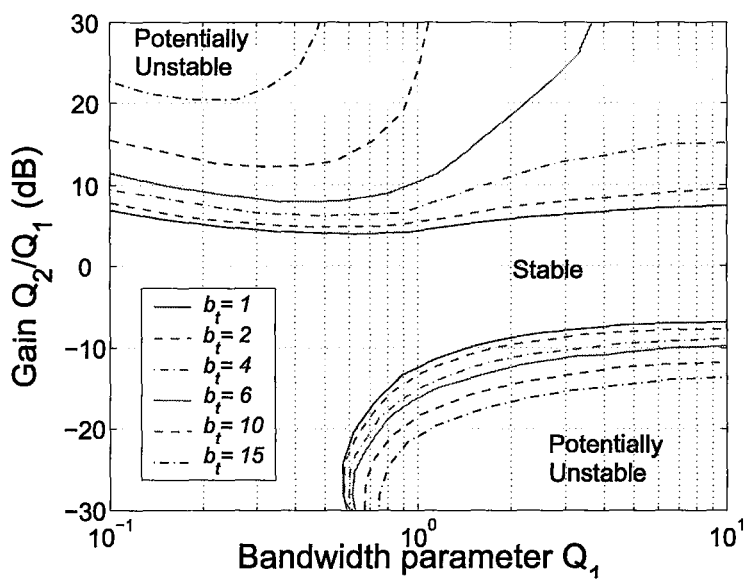

Figure 6.7: Notch position filter stability regions with $\omega_n = 20\pi$ rad/s at different levels of virtual tool damping b_t.

6.3 Mixed Non-Linear/LTI Filtered Mappings

Using LTI filtered mappings with either nonlinear force or nonlinear position scaling the teleoperation block in Fig. 3.1b) can once again be converted to a Lur'e type problem shown previously in Fig. 5.1. This is achieved by defining $G(s)$ to be

$$G(s) = \frac{G^{\mathcal{N}}(s)}{G^{\mathcal{D}}(s)} = \frac{P_{Ze}(s)\mathcal{Z}_e}{P_{Zh}(s)\mathcal{Z}_h + P_{Zt}(s)\mathcal{Z}_t} \tag{6.28}$$

$\Phi(\cdot)$ to be (6.2) as before and the exogenous inputs $u_2 = 0$ and $u_1 \in L_\infty$ to be

$$u_1 = \begin{cases} H_{fh}F_h^* - \bar{\rho} - \frac{H_{fh}\mathcal{Z}_h + H_{Zt}}{H'_{xm}}\rho_e & , \kappa_p(\cdot) \text{ linear} \\ \frac{-H_{fh}F_h^*}{\kappa_f H_{fe}\mathcal{Z}_e} + \frac{\kappa_f^{-1}\bar{\rho}}{H_{fe}\mathcal{Z}_e} + \frac{(H_{fh}\mathcal{Z}_h + H_{Zt})\rho_e}{\kappa_f H'_{xm}H_{fe}\mathcal{Z}_e} & , \kappa_f(\cdot) \text{ linear} \end{cases} \tag{6.29}$$

where $P_{Ze}(s)$, $P_{Zh}(s)$, and $P_{Zt}(s)$ have been defined previously in (6.12), (6.13) and (6.14). Robust stability can once again be investigated using the *sufficient* conditions of the off-axis circle theorem with nonlinear feedback element $\Phi(\cdot)$ and the Nyquist envelope of the interval plant system (6.28). Since the linear plant $G(s)$ contains independent polytopic polynomials $G^{\mathcal{N}}(s)$ and $G^{\mathcal{D}}(s)$, the Nyquist envelope of such a polytopic plant can be found using the method discussed in section 4.3.2 where edge checking must be performed [2].

Once a Nyquist envelope of the linear plant (6.28) is obtained an analogous graphical test to that of Fig. 6.1 can be used to show that an off-circle circle is outside the Nyquist envelope of $G(s)$ to conclude nonlinear stability. When a numerical stability test is desired, the transformation defined previously in (6.6) can be applied to the points that make up the Nyquist envelope of (6.28) to yield stability

condition (6.7). The necessity of edge checking results in a computationally expensive procedure when compared to the Kharitonov polynomials approach used for independent coefficient interval polynomials.

As an example, stability analysis is performed for teleoperation system involving the LTI filters defined in (6.24)-(6.26), the interval ranges in Table. 6.1 with nonlinear force scaling $\kappa_f(\cdot)$ and linear position scaling κ_p. This can reveal potential trade-offs between hand-tremor filtering specifications and nonlinear enhanced force mapping specifications. The results of such an analysis are shown in Fig. 6.8 where nonlinear sector stability regions are found for various values of position filtering bandwidth using a virtual tool impedance of $\mathcal{Z}_t = 0.4s^2 + 15s$. The guaranteed stability region is between the straight line $b = a$ and the curves obtained for each Q value.

The application of position filtering introduces the potential for instability even for linear scalings of force and position, hence disconnected nonlinear sector stability regions can result as shown in Fig. 6.8. These unstable linear gains are easily found by observing where the Nyquist envelope of (6.28) intersects the negative real axis. The analysis in Fig. 6.8 shows that for a certain notch position filter bandwidth a minimum incremental sector stability region can exist, for example by choosing lower sector $a = 1$.

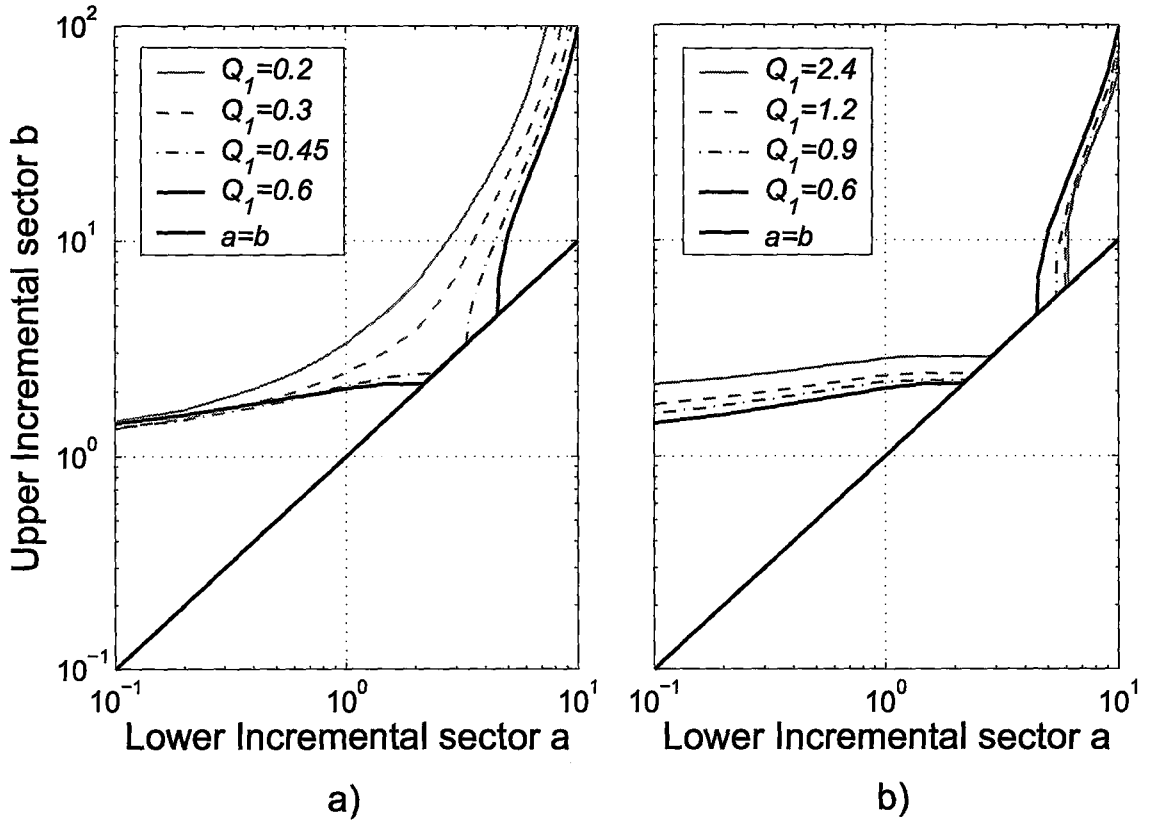

Figure 6.8: Stability regions from off-axis circle criterion with notch position filtering at $\omega_n = 18\pi$ rad/s with gain $\frac{Q_2}{Q_1} = 5$ and varying bandwidth. a) $0.2 \leq Q_1 \leq 0.6$ b) $0.6 \leq Q_1 \leq 2.4$.

6.4 Conservatism of using Bode envelopes

Tan and Atherton have transformed the off-axis circle theorem to be used with Bode envelopes of the linear plant $G(s)$ [64]. In their approach, the non-linear feedback element $\Phi(\cdot)$ is represented by a range of complex gains that lie inside a circle on the gain plane. To obtain this gain plane circle, the off-axis circle on the Nyquist plane is mapped through $z \mapsto -1/z$. For stability the equation $\Phi G(j\omega) + 1 = 0$

is investigated. The gain-phase relationship of the gain-plane circle describing Φ is used in combination with the Bode envelope of $G(s)$ to show stability. For an open-loop stable plant $G(s)$ this is done by ensuring for all gain/phase ranges of Φ in combination with $G(s)$ have combined gain less than one when the combined phase is $-180°$. For more details on the application of this approach the reader should consult [64].

The approach in [64] is equivalent to using the original off-axis circle criterion with a Nyquist envelope that is obtained from a Bode envelope. Hence the Nyquist templates at each frequency are overbounded since they are assumed to have a sector shape. An example of this is shown in Fig. 6.9a) using example (4.32) from section 4.3.2. Complete Nyquist envelopes are also shown in Fig. 6.9b). Applying the off-axis circle theorem to the overbounded Nyquist envelope would result in smaller incremental sector stability ranges since smaller off-axis circles are allowed. Despite this conservatism an advantage of using this approach is that it is less computationally expensive. As was discussed in section 4.3, obtaining a Bode envelope of a polytopic plant only requires the use of its vertex polynomials, thus expensive edge checking is not needed. Another advantage is that stability can potentially be shown for open-loop unstable plants since it may be possible to keep track of the number of encirclements when using a Bode envelope [64]. Ultimately, since the Bode envelope approach is more conservative, an extensive teleoperation stability analysis was not explored for nonlinear feedback stability.

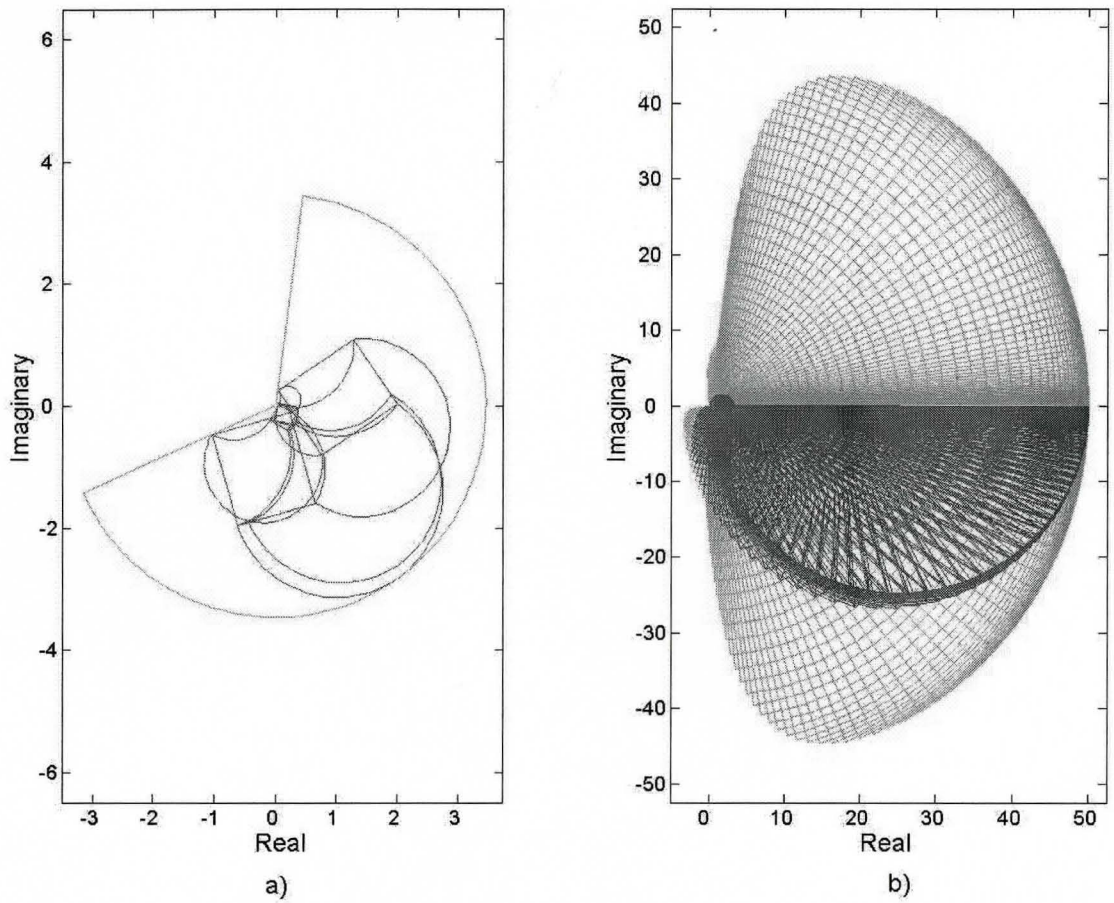

Figure 6.9: Nyquist overbounding a) Nyquist template at $\omega = 30$ rad/s b) Nyquist envelopes. The overbounded Bode envelope approach is in lighter (green) colour whereas the true Nyquist envelope is in darker (red) colour.

Chapter 7

Psychophysics

To design any enhanced generalized mapping one typically should apply psychophysical theory and methods to validate that the mapping actually enhances performance/perception. The first section of this chapter will cover some basic psychophysical theory and methods that can be applied in many types of human factors studies. The second section discusses generalized mapping design and specifically gives design criteria for a nonlinear perception enhancing force mapping. The third section presents psychophysical experiments used to validate the enhanced nonlinear force mapping design.

7.1 Psychophysics Theory and Methods

7.1.1 Theory

Psychophysics is a science that deals with human perception that uses aspects of the physical sciences and as well as psychology. Central to psychophysics is the concept of a sensory threshold. Two different thresholds can be defined: absolute thresholds (RL for the German Reiz Limen) define the smallest amount of stimulus that can be detected, whereas differential thresholds (DL for German Differenz Limen) define the smallest perceivable difference between two stimuli [4]. The DL is sometimes referred to as the *just-noticeable-difference* (jnd) between two stimuli. The stimulus (ϕ) refers to a quantity that is measured in the physical domain. The sensation (ψ) refers to the psychological quantity the observer experiences [4]. *Psychophysical laws* describe the relationship between stimulus (ϕ) and sensation (ψ) [4]. Different senses would have different $\psi - \phi$ relationship since the physical mechanisms of each sense are different. A review of the physical capabilities of different human senses is given in Chapter 2 of [4]. A classical mathematical relationship between sensation and stimuli is Fechner's law (7.1) which first appeared in his 1860 publication *Elements of Psychophysics*. It was not until the 1950's that alternative $\psi - \phi$ relationships were explored. Steven's power law (7.2) [65] has become another popular mathematical representation. The constants k and a would be specific to the sensory modality and stimulus conditions.

$$\text{Fechner's Law} \quad \psi = k \ln \phi \tag{7.1}$$

$$\text{Steven's Power Law} \quad \psi = k\phi^a \tag{7.2}$$

Any experiment to measure sensation typically involves human responses, therefore *sensory response laws* describe the relationship between sensation and the sensory response given by the observer. An ideal sensation-sensory response relationship would be linear with unity gain, in which case the human is able to ideally give a response about their sensation magnitude without distortion. When considering groups of people, on average the sensation-sensory response relationship is linear with unity [4]. In the context of this thesis an ideal sensory response law is assumed. The assumed two-stage sensory theory is thus shown in Fig. 7.1.

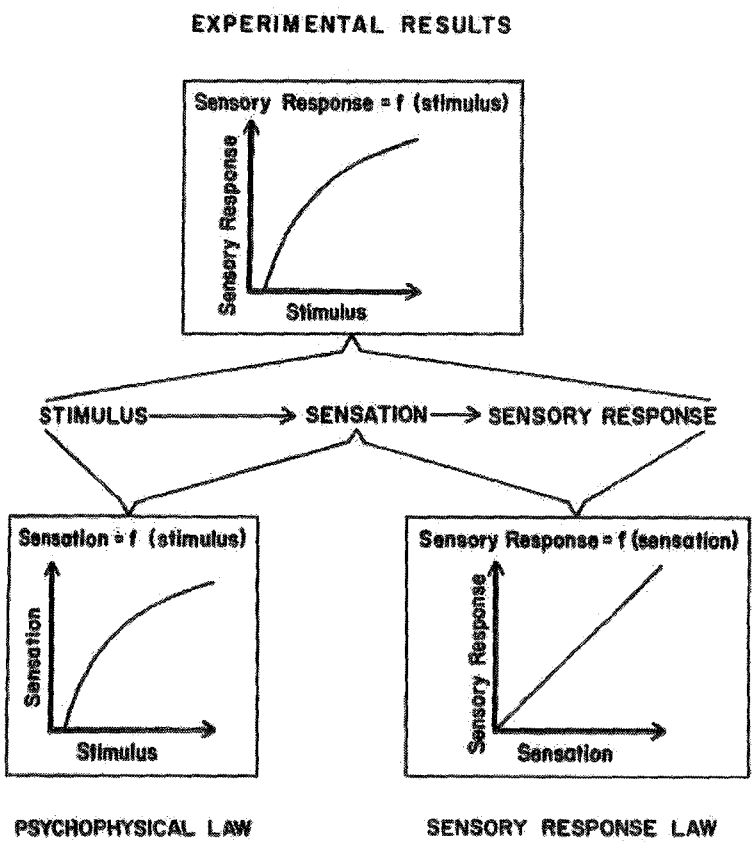

Figure 7.1: Assumed two-stage sensory theory showing how the psychophysical and sensory response laws intervene, figure from [4].

Classical psychophysical threshold theory defines the sensory threshold (both RL and DL) to be a step function that fluctuates over time and under different stimulus conditions. In this theory a momentary step-threshold is assumed to exist at the point of observervation. This fluctuation smooths out the step function into a sigmoidal curve. Thus experimental results would expect to resemble that of Fig. 7.2, where a yes indicates the observer has perceived the stimulus. A popular model of this sigmoidal curve is that it is the integral of a Gaussian distribution that varies among individuals and depends on the sensory modality and stimulus conditions. This response curve is referred to as the psychometric function and describes the subject's performance under different stimulus intensities. This function and its range are task-dependent. For example it is possible to obtain a psychometric function with ranges other than 0-100%. Examples of this will be explained in the next section.

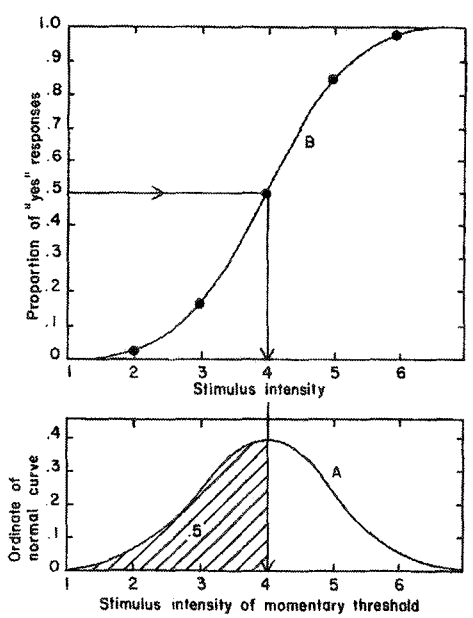

Figure 7.2: Psychometric function from classical threshold theory, figure from [4].

It must be noted that this classical threshold theory does not fully explain the sensory response process since it does not take into account the psychological nature and expectations of the human observer. Improved theories such as that of the Theory of Signal Detection (TSD) are more prevalent in the psychophysics literature today. An overview of TSD in psychophysics can be found in Chapters 5-8 in [4]. Ultimately TSD also results in sigmoidal psychometric functions that take into account the expectations and criteria of the observer [4]. These other theories and theories that explain the relationships between the psychometric function and psychophysical laws are beyond the scope of work in this thesis. The important point is that these theories use the concept of a psychometric function. This psychometric function quantifies the sensory threshold and describes the probability of a response under different stimuli conditions. By choosing a point on the psychometric function one chooses a DL or RL point with an associated probability.

7.1.2 Methods

Psychophysics experiments are typically performed to obtain data about the psychometric function. Ideally it is desirable for different stimuli to be presented at the same place, time and for the same duration to remove space and temporal bias errors. This is usually impossible, especially in the case of measuring differential thresholds. For stimuli presented in different places, spatial counterbalancing where stimuli are equally distributed among the different places is used to reduce spatial bias errors. Additionally order bias caused from predictable stimuli can also be problematic, hence random ordering is typically used. Any experimental method must minimize these and other unwanted bias errors.

The method of constant stimuli or method of constants is a classical experimental technique [4]. This method seeks to obtain the entire psychometric function by presenting repeated stimuli where a wide range of stimuli is chosen. The range covers stimuli from levels that are almost never detected to levels that are almost always detected. An associated probability value is found experimentally on many points on the psychometric function through repeated measurements. Typically curve fitting techniques are used to obtain the psychometric function. For absolute thresholds the 50% level (RL_{50}) is typically chosen as the threshold value since the experimental psychometric function typically resembles that of Fig. 7.2.

For differential thresholds a comparison stimulus can be compared to a standard stimulus. The standard stimulus is always known to the observer and is of fixed value. The varying comparison stimulus is judged to be either of greater or lesser intensity. A hypothetical psychometric function for such a differentiation discrimination experiment is shown in Fig. 7.3.

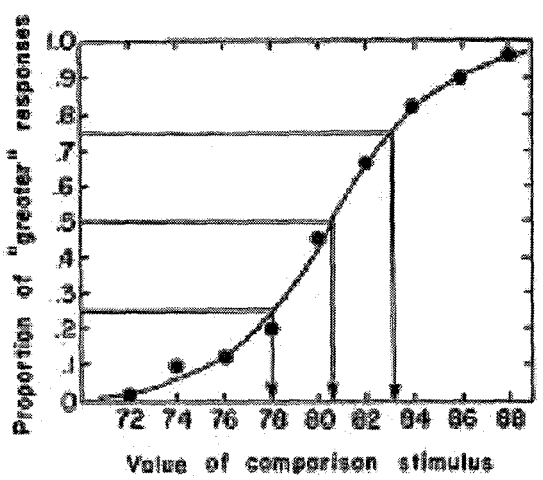

Figure 7.3: Hypothetical psychometric function obtained from method of constants for a discrimination task with a known standard, figure from [4].

In this case the 50% level corresponds to the Point of Subjective Equality (PSE) where no discrimination is expected due to guessing. An experimental PSE that deviates greatly from the standard stimulus value is indicative of unwanted bias errors. Two differential thresholds are defined, an upper threshold, typically $DL_u = P_{75} - PSE$ and a lower threshold usually $DL_l = PSE - P_{25}$. Both correspond to a correct identification performance level of 75%, note when comparing only two stimuli guessing performance is at worst 50%. Typically the upper and lower threshold are averaged, i.e. $DL_{75} = \frac{1}{2}(DL_l + DL_u)$.

The method of constants can also be used with a forced choice paradigm [4]. Instead of yes/no or greater/less responses at each trial, multiple stimuli are presented where the observer has to identify which interval contains the stimulus. For RL experiments only one interval has the stimulus, for DL experiments only one interval contains the comparison and the rest have intensity equal to the standard. Note in DL experiments the observer does not know which stimulus is the standard. The worst case performance is the inverse of the number of intervals, i.e. a two alternative forced choiced task (2AFC) has a psychometric function with performance ranging from 50-100%. A hypothetical example is shown in Fig. 7.4.

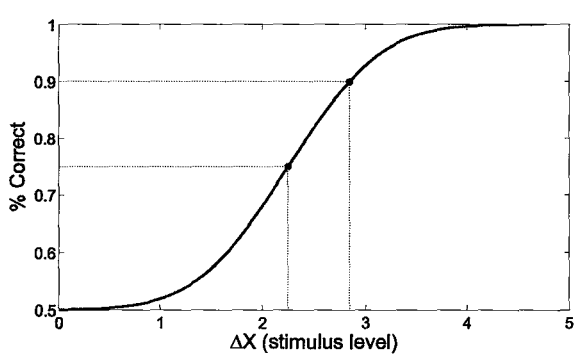

Figure 7.4: Hypothetical psychometric function for a 2AFC discrimination task. Two thresholds (at 75% and 90%) for ΔX can be defined as shown.

The method of Limits is another classical method that is considered to be more efficient that the method of constant stimuli [4]. It seeks to give a single threshold measurement instead of the entire psychometric function. Unfortunately this technique is considered unreliable since subject bias exists and the method does not target a fixed performance level, hence this method will not be discussed in detail.

In many cases the entire psychometric function is not needed since a single representative point may suffice. In such cases adaptive up-down methods are more efficient since they concentrate the stimulus level around a chosen point on the psychometric function [66]. The method is adaptive since future stimulus values are based on the responses of the observer. Typically correct responses results in stimulus intensity (or difference for DL experiments) to decrease or step down (S_{down}) and incorrect responses lead to an increase or step up (S_{up}). The classical Békésy threshold tracking method has symmetric step sizes ($S_{down} = S_{up}$) for incorrect/correct responses and a step is made after each response [67]. This would target an equilibrium point with a performance level of 50%, since the probabilities of moving up and down are equal at the 50% level. For discrimination tasks with only one standard and only one comparison, the classical up-down method is not useful since it converges to the PSE.

A Transformed Up-Down Method (TUDM) proposed by Levitt allows convergence to the 70.7% performance level [66]. Symmetric step sizes are assumed ($S_{up} = S_{down}$) however the rules for when steps are taken have been transformed. The TUDM looks at sequences of responses after a step has been made. A sequence of two consecutive correct responses (++) results in a step-down. An incorrect response (−) or a sequence of correct and incorrect (+−) leads to a step-up. The

TUDM has equilibrium level at 70.7% performance since the probability of moving up is $0.707^2 = 0.5$ and moving down is $0.293 + 0.707 \cdot 0.293 = 0.5$. Additional rules for other performance levels using TUDM are shown in Table. 7.1 [68].

Table 7.1: Transformed Up-Down Method Rules [68]

Entry	Sequence Up	Sequence Down	Equilibrium Performance
1	−	+	50%
2	−+−− or +− or −−	−+−+ or −++ or ++	55%
3	+−− or −	+−+ or ++	59.7%
4	++− or +− or −−	+++ or −+	64.8%
5	+− or −	++	70.7%
6	++−+− or ++−− or +− or −	++−++ or +++	74.9%
7	++− or +− or −	+++	79.4%
8	+++− or ++− or +− or −	++++	84.1%
9	+++++− or ++++− or +++− or ++− or +− or −	++++++	89.1%

An adaptive up-down method that allows arbitrary performance levels and is less complicated than the TUDM is the Weighted Up-Down Method (WUDM) proposed by Kaernbach [69]. Asymmetric steps are used ($S_{down} \neq S_{up}$) instead

of response sequences. Steps are made after single responses and convergence to performance percentage level p is achieved provided the steps satisfy equilibrium equation (7.3).

$$S_{up}(1-p) = S_{down}p \tag{7.3}$$

For example choosing $p = 0.75$ results in $S_{up}/S_{down} = 3$, hence for a correct response a step down of one unit is taken and for an incorrect response a three unit step-up is taken. It has also been shown the WUDM has a small advantage over TUDM in terms of efficiency and faster convergence [70] [69].

All up-down methods obtain their data by plotting stimulus intensity versus trial number. Threshold measurements at the chosen performance level are obtained by taking the midpoint value of each run. The midpoint value gives an single estimate of the threshold with reduced variability. A run is a set of increasing or decreasing steps. Either increasing or decreasing runs are chosen to ensure independence of the data. The midpoints of the runs yield mean and variance measurements of the sensory threshold of interest. The starting point can bias the first few runs, hence they are typically ignored. *A priori* knowledge and preliminary experiments can yield good starting points for the up-down methods; even so the first run should always be ignored. Hypothetical data using the WUDM are shown in Fig. 7.3. The choice of step size influences both the speed of convergence and the variability of the data. Large steps have faster convergence but greater variability, smaller steps have the opposite. An optimal step size that balances the two should be chosen. Strategies such as initially taking large steps followed by smaller steps can also easily be employed.

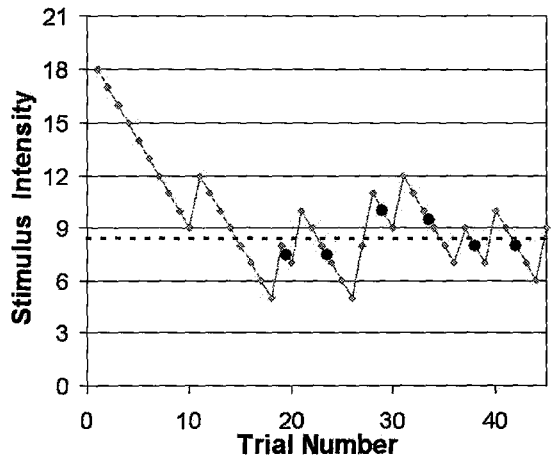

Figure 7.5: Hypothetical data from WUDM with $S_{up}/S_{down} = 3$. The dark circles are threshold measurements and the dotted line their average.

7.2 Enhanced Mapping Design

7.2.1 Nonlinear force mapping

The design of any non-linear force mapping will be a task-dependent procedure. In soft-environment telemanipulation it might be desired to improve performance in a stiffness or softness discrimination task. Force and stiffness discrimination has been shown experimentally to obey Weber's Law [43], [4]. Weber's Law states that the just-noticeable difference (*jnd*) in stimulus intensity ($\Delta\phi$) is linearly proportional to the starting intensity (ϕ) by a constant factor c:

$$\Delta\phi = c\phi \text{ or } \frac{\Delta\phi}{\phi} = c \tag{7.4}$$

The Weber constant c can therefore be used as a measure of differential sensitivity. Assuming *jnd* increments are equally spaced in the sensation domain (ψ), Fechner's Law (7.1) can be derived from Weber's Law. To show this one takes the derivative of (7.1) to yield the expression $\Delta\phi = \frac{\phi}{k}\Delta\psi$. Substituting this expressing into (7.4) yields $\Delta\psi = ck$ which is constant. Weber's original work dealt with the discrimination ability of lifted weights. Fechner, aware of this work sought a mathematical relationship between sensation (ψ) and stimulus (ϕ) and proposed (7.1) to be consistent with Weber's results.

A force mapping can be used to modify the transmitted forces to improve the perceptual ability of an individual. For enhanced differential sensitivity the mapping (7.5) should satisfy (7.6).

$$F_h = k_f(F_e) \tag{7.5}$$

$$\frac{\Delta F_h}{F_h} > \frac{\Delta F_e}{F_e} \text{ or } \frac{\delta F_h}{\delta F_e} > \frac{F_h}{F_e} \tag{7.6}$$

Using (7.5), (7.6) can be rewritten as (7.7), where $'$ denotes the derivative:

$$\frac{F_e k_f'(F_e)}{k_f(F_e)} > 1 \text{ or } \frac{k_f^{-1}(F_h)}{F_h(k_f^{-1}(F_h))'} > 1 \tag{7.7}$$

For linear mappings of force, (7.7) can only hold with equality and differential sensitivity cannot be enhanced. Condition (7.7) can be used to enhance sensitivity over a specified range of environment or hand forces. In particular, force mappings of the form (7.8) with $\beta > 1$ satisfy (7.7) and yield enhanced sensitivity under Weber's Law. Diminished sensitivity occurs when $\beta < 1$.

$$F_h = \alpha|F_e|^\beta \cdot \text{sign}(F_e) \tag{7.8}$$

7.2.2 Nonlinear Spatial and Filtered Mappings

Nonlinear position mappings can be used to better manage workspace in the teleoperation system. For example an area of high precision can be defined by having an appropriate position scaling in that region. This can be achieved through piecewise continuous line segments in the position mapping from master to slave. Each line segment can have a different slope, the connecting regions can also be chosen to have continuous derivatives to improve continuity.

For controllers that enforce velocity tracking, as opposed to enforcing position tracking, an appropriate nonlinear velocity mapping can also potentially increase precision. This can be done by having slow hand velocities scaled less than fast hand velocities. The proposed controller in this thesis can be made to work in velocity mode by eliminating virtual tool damping. However, doing so is done at the expense of teleoperation system stability. Therefore this velocity generalized mapping would require an improved controller.

Filtered mappings can improve teleoperation performance by filtering unwanted system noise. For example, filtering force sensor signals can improve system performance by not conveying those disturbances to the operator. Surgeon hand tremor frequencies have been measured to be in the 8-12Hz range [32]. Using simple low-pass filters produce an undesirable sluggish response, hence frequency band notch type filters like those presented in section 6.2.3 can be utilized to preserve high frequency content. Reducing hand tremor can potentially improve human performance in fine telemanipulation. Further research is required to determine the types of filtered force mappings that can improve human perception. However some insight can be gained by studying the frequency responses of the

different haptic sensors in the skin. These responses are shown in Fig. 7.6 which has been obtained from [5]. Further psychophysics research and human factors experiments are required to determine more specific design criteria for enhanced nonlinear spatial and filtered mappings.

This section is concluded by commenting that the issue of human adaptation and learning to any enhanced mapping design should be addressed. Also in a practical implementation it may be desirable to switch between different enhanced mappings on-the-fly based on the desired task to be performed. This switching has potential negative implications on perception, performance and practical ease of use. All these issues require further human factors studies to effectively use enhanced generalized mappings.

	Mechanoreceptors				
Haptic Features	**Pacinian Corpuscles**	**Ruffini Endings**	**Meissner Corpuscles**	**Merkel Disks**	**Hair Follicles**
Skin Type	Glabrous and hairy	Glabrous and hairy	Glabrous	Glabrous	Hairy
Stimulation Objective (physical parameters to be sensed)	Vibration, acceleration, roughness	Skin stretch, lateral force, motion direction, static force	Velocity, flutter, slip, grip control	Skin curvature, pressure, form, texture, edges	Touch
Stimulation Type	Skin motion	Skin motion and sustained skin deformation	Skin motion	Skin motion and sustained skin deformation	Hair motion
Spatial Resolution	Very poor (2 cm)	Poor (1 cm)	Fair (3 – 5 mm)	Good (0.5 mm)	
Stimulation Frequency Range (Hz)	100 – 1,000	0.4 – 100	2 – 40	0.4 – 10	
Interstimulus Interval	← Five ms to perceive separate stimuli; 20 ms to perceive stimuli order →				

	Kinesthetic Receptors			
Haptic Features	**Golgi Endings**	**Ruffini Endings**	**Golgi Tendon Organs**	**Muscle Spindles**
Location	Joint ligaments	Joint capsules	Tendons	Muscles
Stimulation Objective (physical parameters to be sensed)	Joint movement at end range of motion Extreme flexion/ extension	Joint movement, particularly at end range of motion Static and dynamic	Active position sense Link to limb position Force	Active movement of muscles Conscious experience of body movement and position Weight supported by limb
Stimulation Type	Joint tension at extreme positions	Capsule stretch	Muscle tension and force	Muscle stretch/rate of change Vibration
Feedback Loop Range	← 0.5 – 1.7 Hz →			

Figure 7.6: Haptic tactile and kinesthetic receptors. Figure modified from [5].

7.3 Experiments

Human perception experiments were performed under different force mapping conditions to evaluate the performance of the nonlinear force mapping design discussed in the previous section. The experimental paradigm chosen for the perception experiments was a two interval, two alternative forced choice procedure using an adaptive weighted up-down method (WUDM) [4], [69]. The task was to correctly identify in a virtual environment which interval the comparison stiffness was presented in a given trial. Two different scenarios were chosen, one with visual and haptic (VH) feedback and the other with haptic only (HO) feedback. These two scenarios were chosen since in the intended application, robotic surgery, the quality of visual feedback can vary greatly. When comparison stiffness values were greater than the standard base stiffness the subject was to select the stiffer environment. When the comparison had lower stiffness the subject was to chose the softer environment. Since environment force is a function of stiffness, it is hypothesized that force and stiffness sensitivity are directly coupled. The virtual environment forces obeyed Hooke's law resulting in a linear relationship between stiffness and force.

A base stiffness of 500 N/m was chosen for the standard stimulus. For upper DL measurements the comparison stiffness was always greater than the standard, for lower DL measurements the comparison stiffness was less. In a given session either the VH or HO scenario was chosen where either the upper DL or lower DL was measured. To reduce order bias the standard stimulus was presented randomly first in half of the trials and second in the other half. Performance in such a task yields a psychometric function that ranges from 50% guessing correct to 100%

correct. A difference threshold at 75% correct was chosen and measurements at this level were obtained using the WUDM by decreasing the stiffness difference between the comparison and standard by 16 N/m for each correct response, and increasing it by 48 N/m for each incorrect response. To reduce time effects and keep the trial time consistent, contact time with each box was at most three seconds. This was enforced by removing haptic feedback after 3 seconds had elapsed from initial contact.

The linear spring forces were mapped through three different mappings as shown in Fig. 7.7, with the mapping equations given in Table 7.2. To reduce subject bias, the enhanced and diminished mappings were scaled such that all three mappings felt similar to each other and that they shared a common point at 8 N to yield the same force range. The three mappings were interleaved in the same session and presented in random order to further reduce any bias errors. Each session consisted of a total of 120 trials where 40 trials of data was recorded for each mapping. With 40 trials, the WUDM yielded approximately 6 useful threshold measurements per mapping. The starting value for the comparison stiffness was chosen to be 692 N/m for upper DL measurements, 356 N/m for lower DL measurements and was the same for each force mapping in a given session. Eleven volunteers were recruited to participate in the psychophysics experiments with ages ranging from 22 to 26, of which eight were male and three were female. Each volunteer completed four sessions, two for the VH scenario and two for the HO scenario, for a total of 480 trials. Prior to each session each subject had a practice period to get familiar with the experimental procedures.

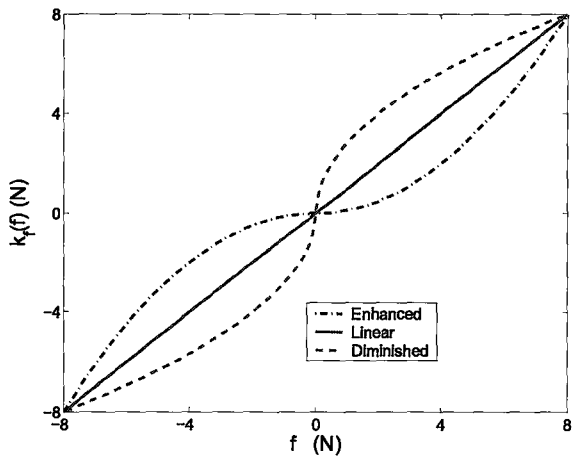

Figure 7.7: Mappings used for psychophysics experiments.

The experimental setup for the stiffness discrimination task is shown in Fig. 7.8. A Quansar planar twin-pantograph haptic device with maximum force output of approximately $8N$ was used as the user interface, and Matlab Virtual Reality toolbox was employed as the visual display. A virtual reality environment was chosen, as opposed to a real teleoperation task, for its ease and consistency in changing the stiffness of the environment, a virtual box in this case. The control software used was Matlab RTW/Tornado RTOS with a sampling frequency of 1024 Hz with visual feedback shown in the virtual reality display updated at a rate of 32 Hz.

The position of the haptic robot end-effector corresponded to the position of a small white sphere in the virtual reality display. The color of the first box was always red and the second was blue. The virtual box would automatically switch its color and stiffness provided that: i) three(3) seconds have elapsed from initial contact with the red box and ii) the small white sphere is not in contact with the red box. Subjects made their choice by double-clicking the button of the corresponding color that had the stiffer box for an upper DL session or the softer box

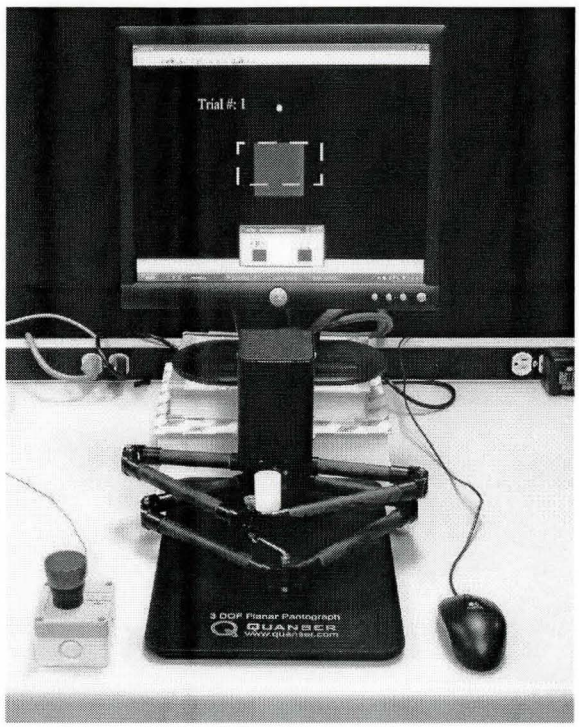

Figure 7.8: Setup for psychophysics experiments. Note: The dashed box represents the location of the selection dialog box under the haptics only experiments where visual feedback is removed.

for a lower DL session. To reduce spatial bias subjects where instructed to interact with only the top surface of the virtual environment. For the VH scenario, the selection dialog box was entirely below the virtual box as is shown in Fig. 7.8 by ignoring the dashed rectangle. For the HO scenario visual feedback was removed by placing the selection dialog box so that it blocked the top portion of the virtual environment, as illustrated in Fig. 7.8 via the dashed rectangle. The bottom portion of the box was left visible to enable the user to identify the color of the box. Since the position of the haptic device end-effector was still visible, the subjects were instructed to keep their attention on the computer monitor to strictly enforce the HO scenario.

Experimental results for the stiffness discrimination task are shown in Fig. 7.9, where for each subject the average of threshold measurements for each mapping is plotted for both VH and HO scenarios. Despite large variability among the subjects, a trend is seen to support the hypothesis that the proposed nonlinear force mapping enhances stiffness sensitivity regardless of the presence of visual feedback. Specifically under the VH scenario, nine out of eleven subjects had an improved upper DL and eight out of eleven had an improved lower DL under the enhanced force mapping. For the HO scenario nine out of eleven had an improved upper DL and another nine out of eleven an improved lower DL. This trend is also evident from Table 7.2 where the overall average DL and stiffness threshold among all subjects is given for each experimental condition. Comparing the VH and HO scenarios, visual feedback improves stiffness discrimination. This result is in agreement with previous reports in the literature, e.g. see [44]. All threshold measurements were statistically analyzed using Repeated Measures ANalysis Of VAriance (ANOVA) [71]. The Repeated Measures ANOVA method is discussed in Appendix A.2. The resulting analysis is summarized in Table 7.3 based on which it can be concluded that the experimental results are statistically significant.

Table 7.2: Average Difference Threshold for 75% Performance

Mapping Type	Enhanced	Linear	Diminished
$k_f(f)$	$\frac{1}{8}f^2 \cdot \text{sign}(f)$	f	$\sqrt{8\|f\|} \cdot \text{sign}(f)$
Upper DL HV (*)	116.1 (616.1)	158.8 (658.8)	189.5 (689.5)
Lower DL HV (*)	90.8 (409.2)	110.0 (390.0)	145.1 (354.9)
Upper DL HO (*)	235.3 (735.3)	292.8 (792.8)	345.9 (845.9)
Lower DL HO (*)	125.8 (374.2)	151.7 (348.3)	172.6 (327.4)

*the corresponding stiffness level is shown in parenthesis.

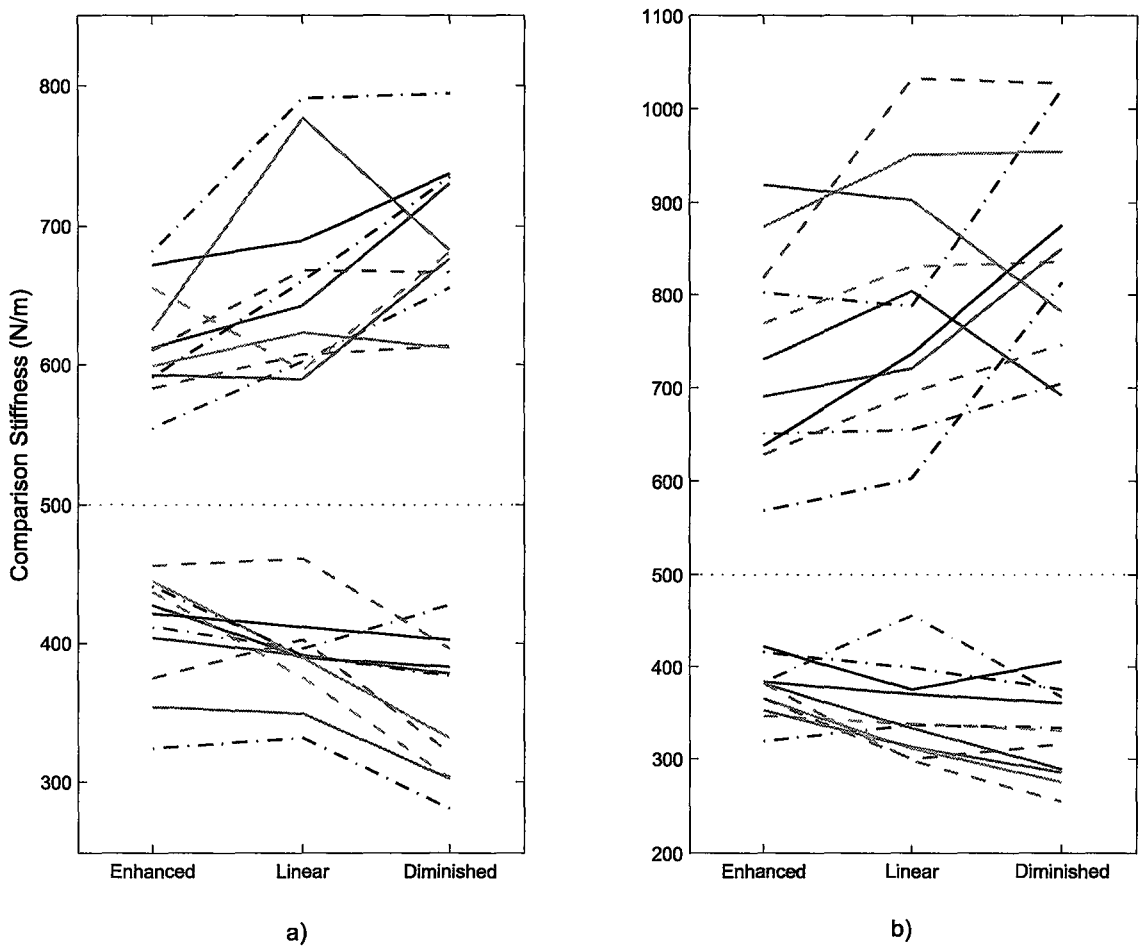

Figure 7.9: Subject comparison stiffness for 75% performance versus mapping a) Haptics with Vision (HV) scenario b) Haptics Only (HO) scenario

Table 7.3: Repeated Measures ANOVA analysis

Threshold	All mappings same	Linear/Enhanced same	Linear/Diminished same
Upper DL HV	$p < 0.001$	$p < 0.01$	$p < 0.05$
Lower DL HV	$p < 0.001$	$p < 0.05$	$p < 0.01$
Upper DL HO	$p < 0.001$	$p < 0.001$	$p < 0.01$
Lower DL HO	$p < 0.001$	$p < 0.05$	$p < 0.05$

Chapter 8

Teleoperation Experiments

Teleoperation experiments were performed to validate the generalized mapping adaptive controller presented in chapter 3. The first section in this chapter presents the experimental setup used for the telemanipulation experiments. The second section presents the assumed workspace dynamic model and gives details on how the controller was implemented. The final section shows experimental results where non-linear/filtered force/position mappings were utilized.

8.1 Experimental Setup

The master/slave experimental setup is shown in Fig. 8.1. Two Quanser pantograph mechanisms each with two active axes of motion in the x-y plane have been employed as master and slave robots. The pantograph devices are actuated by two direct-drive DC motors attached to the proximal links. Motor shaft torque is controlled via current controlling power supplies. The shaft angles are measured by optical encoders with $20,000$ counts per revolution. Two Mini40 force/torque sensors from ATI Industrial Automation have been attached to the mechanisms end-effectors to measure the hand and environment interaction forces. Sponge is used to create the effect of a soft tissue. The control code runs under Matlab RTW/Tornado VxWorks real-time operating system with a sampling frequency of 2048 Hz. Two PCs were utilized, a Windows based PC was used to program the controller using Simulink. This PC is connected to a second PC that ran the control code under VxWorks RTOS to control the master and slave devices.

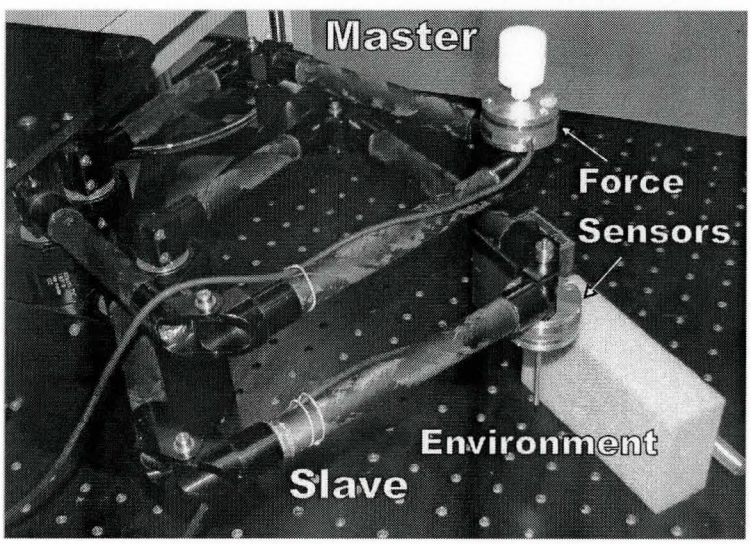

Figure 8.1: The two-axis experimental setup.

8.2 Controller Implementation

The pantograph devices are light, have low-friction and are easily backdrivable. The mass of the force sensor and end-effector attachments dominate the device dynamics, hence the master/slave subsystems are modeled as linear decoupled mass-spring-damper systems, with parametric uncertainty, in the workspace coordinates as shown in Fig. 8.2. Position-dependent variations in the device dynamics due to nonlinearities are adapted for by the local master/slave controllers. To deal with the human exogenous force F_h^*, the control law in (3.15) employs a switching term that can cause unwanted chattering in the control signal. For the experiment the master controller was modified such that it would adapt for F_h^* by adding it to the feedforward term (3.20). This is acceptable provided the adaptation is much faster than the rate of change in F_h^*. The resulting dynamic equation is shown in (8.1), where $\gamma = m$ and $\lambda = h$ for the master subsystem and $\gamma = s$ and $\lambda = e$ for the slave subsystem. Note, $x_{\gamma 0}$ and $y_{\gamma 0}$ are the contact points.

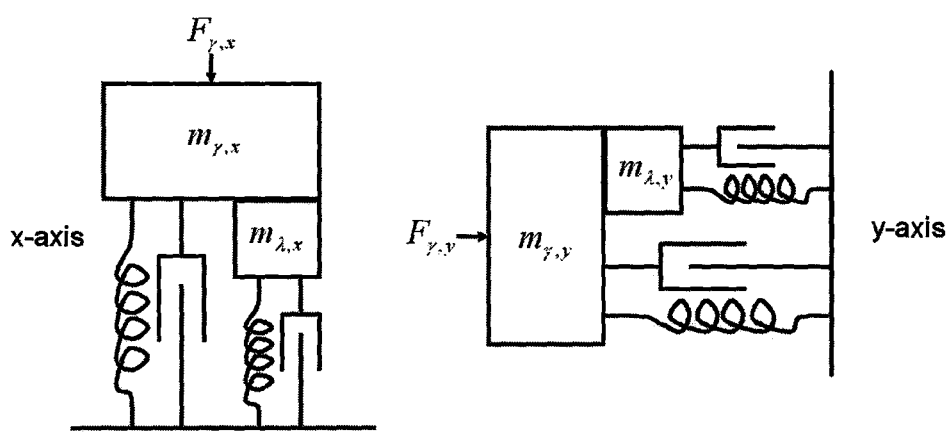

Figure 8.2: Dynamic model used for workspace controllers.

$$\begin{bmatrix} m_{\gamma,x}+m_{\lambda,x} & 0 \\ 0 & m_{\gamma,x}+m_{\lambda,x} \end{bmatrix} \begin{bmatrix} \ddot{x}_\gamma \\ \ddot{y}_\gamma \end{bmatrix} + \begin{bmatrix} b_{\gamma,x}+b_{\lambda,x} & 0 \\ 0 & b_{\gamma,x}+b_{\lambda,x} \end{bmatrix} \begin{bmatrix} \dot{x}_\gamma \\ \dot{y}_\gamma \end{bmatrix} + \begin{bmatrix} k_{\gamma,x}+k_{\lambda,x} & 0 \\ 0 & k_{\gamma,x}+k_{\lambda,x} \end{bmatrix} \begin{bmatrix} x_\gamma - x_{\gamma 0} \\ y_\gamma - y_{\gamma 0} \end{bmatrix} = \begin{bmatrix} F_{\gamma,x} \\ F_{\gamma,y} \end{bmatrix} = F_\gamma \quad (8.1)$$

The basic control block diagram for the teleoperation system is shown in Fig. 8.3, where the workspace variables are vector quantities. The force sensor and joint angles are filtered to reduce sensor noise and quantization noise. The effect of quantization noise is small since the encoder resolution is high, hence the position filter can be omitted. A second-order filter (8.2) was used with $\omega_n = 500\pi$ rad/s for the position filter and $\omega_n = 120\pi$ rad/s for the force filter. Angular velocity was obtained by filtering using (8.3) with $\omega_n = 100\pi$ rad/s. All filters used in the controller implementation were converted to discrete-time filters using the Matlab *c2d* function with the 'tustin' option where a bilinear transformation is utilized.

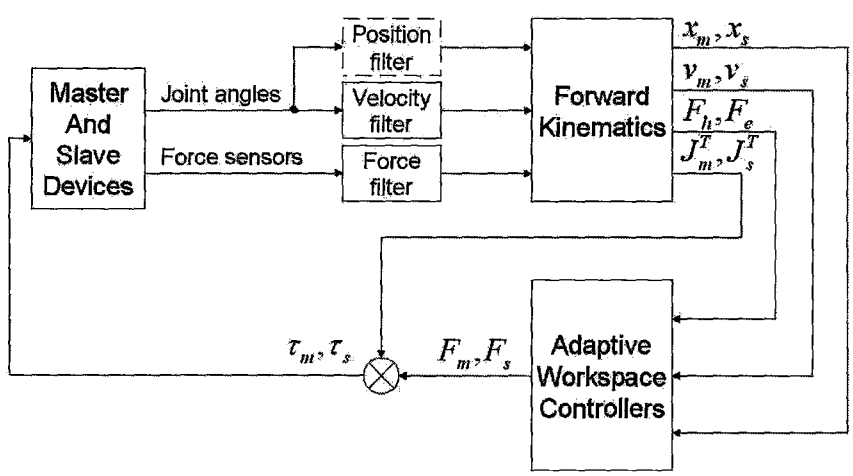

Figure 8.3: Control block diagram for teleoperation experiments.

$$\text{Pos./Force Filter}: \quad \frac{\omega_n^2}{s^2 + 2\zeta\omega_n s + \omega_n^2} \tag{8.2}$$

$$\text{Vel. filter}: \quad \frac{\omega_n^2 s}{s^2 + 2\zeta\omega_n s + \omega_n^2} \tag{8.3}$$

A forward kinematics block in (8.3) was used to obtain the workspace positions, velocities and forces for use in the adaptive workspace controllers. This block also obtains the Jacobian matrices to convert the workspace control forces into joint level torques, i.e. $\tau_\gamma = J_\gamma^T F_\gamma$ [26]. The force F_e measures the force the slave robot applies to the environment, whereas F_h measures the force the operator applies to the master robot. Hence the directions of positive F_e and F_h are opposite.

The master/slave teleoperation control and adaptation laws expressed in (3.15)-(3.19), (3.23) and (3.36)-(3.38) are implemented using the structure shown in Fig. 8.4, where without loss of generality only one workspace axis is considered. The strictly proper filters H_{fh}, H_{fe}, H_{xs}, H_{xm} and functions $k_f(\cdot)$ and $k_p(\cdot)$ are utilized to enforce the generalized mappings and are present in the v_{md} and v_{sd} blocks shown in Fig. 8.4. Also inside v_{md} and v_{sd} are blocks to implement the filter $\tilde{Q} = \frac{s}{s+C}Q$. The position dependent Jacobian J defined by $Jv_s = \dot{k}_p(x_s)$ requires an additional input of slave position (x_s) that is not shown for clarity.

The blocks Δx_m and Δx_s calculate the quantities $x_m - x_{m0}$ and $x_s - x_{s0}$ where a relay block is used to find x_{m0} or x_{s0}. They operate such that initial contact is assumed once the magnitude of force (from both dimensions) exceeds a value $C_{on} = 0.3$ N, contact is assumed to be maintained until the measured force magnitude drops below $C_{off} = 0.2$ N. The contact points are locked at the moment when the threshold C_{on} is initially exceeded. In the free motion condition $\Delta x_\gamma = 0$.

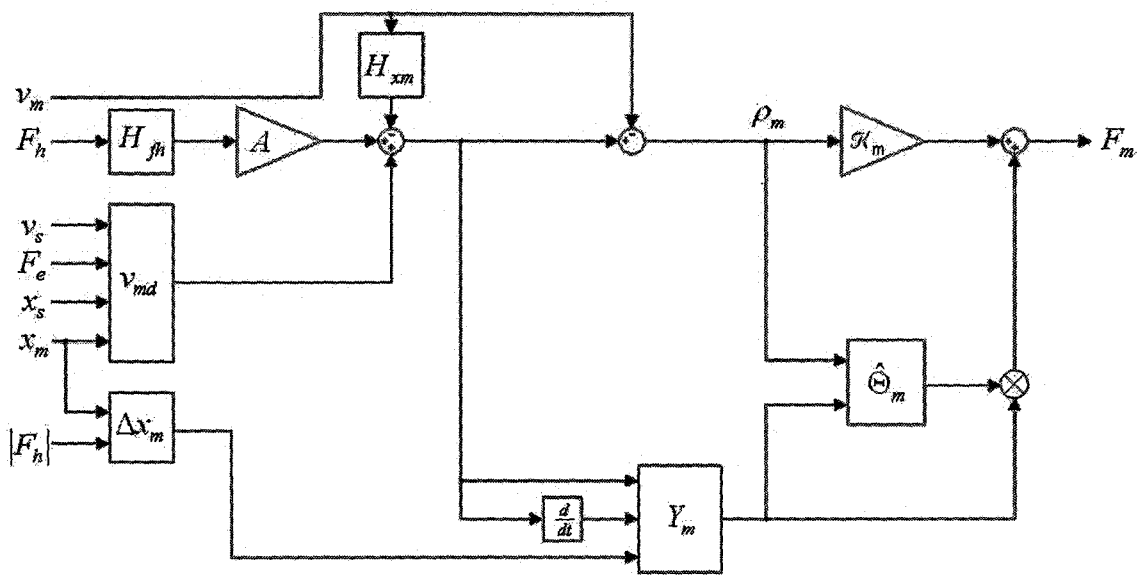

a)

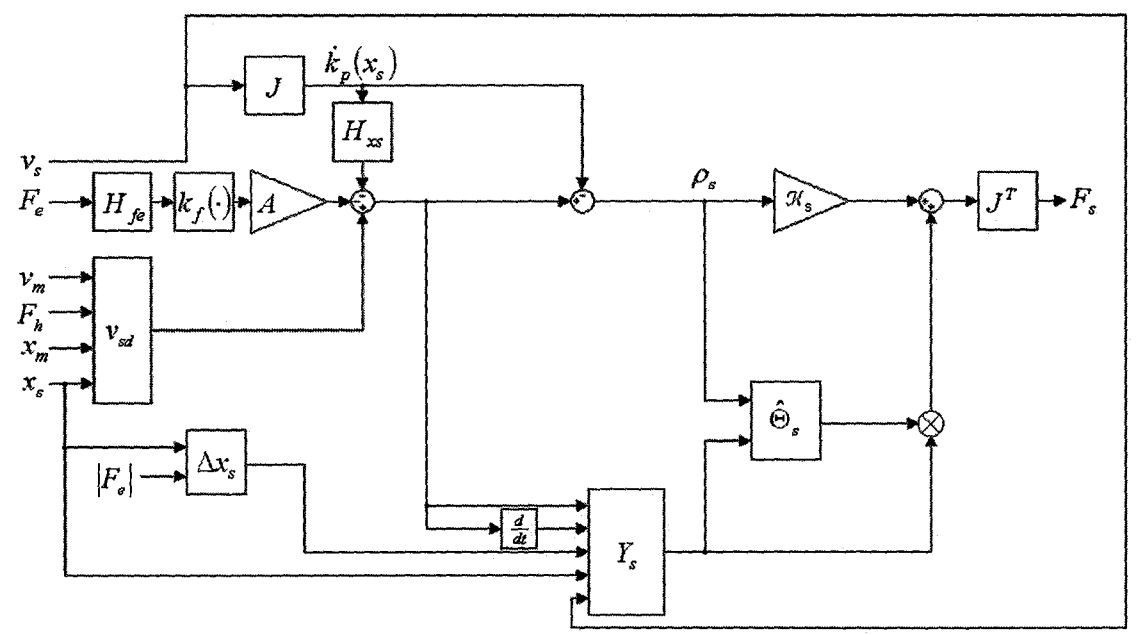

b)

Figure 8.4: Adaptive controllers a) master controller b) slave controller

The $\frac{d}{dt}$ blocks in Fig. 8.4 are not explicitly used. Instead, expressions $\dot{\rho}_m + \dot{v}_m$ and $\dot{\rho}_s + \ddot{k}_p(x_s)$ are found by defining filters $\dot{H}_{fh}$, $\dot{H}_{fe}$, $\dot{H}_{xm}$, $\dot{H}_{xs}$, defining force mapping Jacobian J_{kf} to satisfy $J_{kf}\dot{H}_{fe}F_e = \dot{k}_f(H_{fe}F_e)$, using position mapping Jacobian J and utilizing $\dot{\tilde{Q}} = CQ - C\tilde{Q}$ when necessary.

In a single axis implementation regressor Y_m is defined in (8.4), where the added fourth element in effect includes exogenous force F_h^* in the adaptation. The adaptation estimates of the combined mass/hand parameters are also given in (8.4). For slave adaptation the regressor Y_s and associated slave/environment estimates defined in (8.5) are used. Note here J is a scalar quantity and $J' = \frac{d}{dx_s}J$.

$$Y_m^T = \begin{bmatrix} \dot{\rho}_m + \dot{v}_m \\ \rho_m + v_m \\ \Delta x_m \\ -1 \end{bmatrix}, \quad \hat{\Theta}_m = \begin{bmatrix} \hat{m}_{m+h} \\ \hat{b}_{m+h} \\ \hat{k}_{m+h} \\ \hat{F}_h^* \end{bmatrix} \tag{8.4}$$

$$Y_s^T = \begin{bmatrix} J^{-2}\left(\dot{\rho}_s + \ddot{k}_p(x_s)\right) - J'J^{-3} \cdot v_s \cdot \left(\rho_s + \dot{k}_p(x_s)\right) \\ J^{-2}\left(\rho_s + \dot{k}_p(x_s)\right) \\ J^{-1}\Delta x_s \end{bmatrix}, \quad \hat{\Theta}_s = \begin{bmatrix} \hat{m}_{s+e} \\ \hat{b}_{s+e} \\ \hat{k}_{s+e} \end{bmatrix} \tag{8.5}$$

The form of Y_s in (8.5) is necessary to be consistent with (8.1) and the mapped slave dynamics expressed in (3.13), where it is noted $\dot{J} = \frac{d}{dt}J = \frac{d}{dx}J \cdot \frac{dx}{dt} = J' \cdot v_s$. This form of Y_s required signals x_s and v_s, which are explicitly shown in Fig. 8.4b). Finally the implementation of blocks $\hat{\Theta}_m$ and $\hat{\Theta}_s$ in Fig. 8.4 use Matlab discrete-time integrator blocks with upper/lower limits to implement adaptation rule (3.23).

This section is concluded by remarking that in a discrete-time implementation the local force feedback can cause instability in the system. This issue was explored by Zhu and Salcudean [24] for a controller with simple linear mappings where it is shown the product of AC must be small enough for stability in a discrete-time implementation. The stability conditions derived in this thesis are valid for the continuous-time domain. Using the results from [24], a value of AC small enough results in a stable discrete-time implementation. It has also been heuristically observed that other parameters that amplify local force-feedback should be kept low to maintain stability. Conditions for stability for the proposed generalized mapping controller in a discrete-time implementation requires further research.

8.3 Experimental Results

Experimental results for the adaptive controllers described in the previous section and chapter 3 were obtained using the control parameters given in Table 8.1. The specific limits and gains used for adaptation are given in Table 8.2. The resulting position and force experimental data were recorded at a rate of 256 Hz.

Table 8.1: Controller Parameters

A	C	Λ	$\mathcal{K}_s, \mathcal{K}_m$	Γ_s, Γ_m
0.01 $kg^{-1}s$	80π rad/s	10 s^{-1}	35 Nsm^{-1}	1000-25000000

Table 8.2: Adaptation Parameters

	Range	Gain ($\Gamma_{\gamma i}$)
$\hat{m}_{m+h}$	0.1–0.4 kg	1000
$\hat{b}_{m+h}$	1–20 Ns/m	2000
$\hat{k}_{m+h}$	0-1 N/m	10,000,000
$\hat{F}_h^*$	-10–10 N	2000
$\hat{m}_{s+e}$	0.1–0.4 kg	1000
$\hat{b}_{s+e}$	1–20 Ns/m	20000
$\hat{k}_{s+e}$	0-1000 N/m	25,000,000

8.3.1 Nonlinear force scaling with filtered position mapping

The first experiment was conducted using the linear position scaling (8.6) and nonlinear monotonic force scaling (8.7) with the filters defined in (8.8)-(8.10). These filters were previously seen in section 6.2.3. The chosen nonlinear force mapping was selected to have a narrower incremental sector than the psychophysics experiments enhanced mapping while having similar shape.

$$\kappa_p(x) = x \tag{8.6}$$

$$\kappa_f(f) = 0.75f \cdot \tanh\left(\left(\frac{f}{4}\right)^2\right) + 0.25f \tag{8.7}$$

$$H'_{xm} = 1 \tag{8.8}$$

$$H'_{xs} = 1 + \frac{(\frac{\omega_n}{Q_1} - \frac{\omega_n}{Q_2})s}{s^2 + \frac{\omega_n}{Q_2}s + \omega_n^2} = \frac{s^2 + \frac{\omega_n}{Q_1}s + \omega_n^2}{s^2 + \frac{\omega_n}{Q_2}s + \omega_n^2} \tag{8.9}$$

$$H_{fe} = H_{fh} = \frac{C}{s+C} \tag{8.10}$$

The position filter parameters used were $\omega_n = 18\pi$ rad/s, $Q_1 = 0.6$ and $Q_2 = 3$. The scalings result in the nonlinear teleoperation feedback element $\Phi(\cdot) = \kappa_p()^{-1}\kappa_f()$ to be in incremental sector $[0.25, 2.1]$. During the experiment, the operator moved the

master device in free motion and made several stable contacts with the environment. The teleoperation controller rapidly adapted to the environment stiffness variations and produced accurate mappings between the master/slave position and force signals, as shown in Fig. 8.5(a),(b). It should be pointed out that the force changes during contact have been deliberately performed by the operator to demonstrate force tracking. The non-zero operator forces in free motion are due to the intervening virtual tool dynamics. The resulting force mapping, during soft-environment contact, in the $(f_h - f_e)$ planes for the x and y axes are compared with the desired force mapping in Fig. 8.5(c). It is clear that the nonlinear force scaling objective has been achieved. Deviations from desired and actual nonlinear force scaling in Fig. 8.5(c) can be attributed to the intervening virtual tool dynamics.

In general, the application of nonlinear force mappings, separately along each coordinate axis, can alter the force direction. Since human perception sensitivity to the changes in the direction of force is about 20° [46], variations below this level are deemed acceptable. Alternatively, the nonlinear force mappings may only be applied to the force magnitude, hence preserving its direction.

To show frequency filtered position mapping, a separate experiment was conducted such that the operator would hold as still as possible the position of the slave end-effector for 64 seconds. This was done to best excite the teleoperation system at the desired tremor frequencies and obtain good frequency spectral data. An experimental frequency power spectrum of the position mapping was obtained by averaging 32 (16 from x, 16 from y) power spectral estimates of H'_{xs}. Each estimate results from the division of a 1024-pt Fast Fourier Transform (FFT) of 4 seconds of master position data by a 1024-pt FFT of 4 seconds of slave position data.

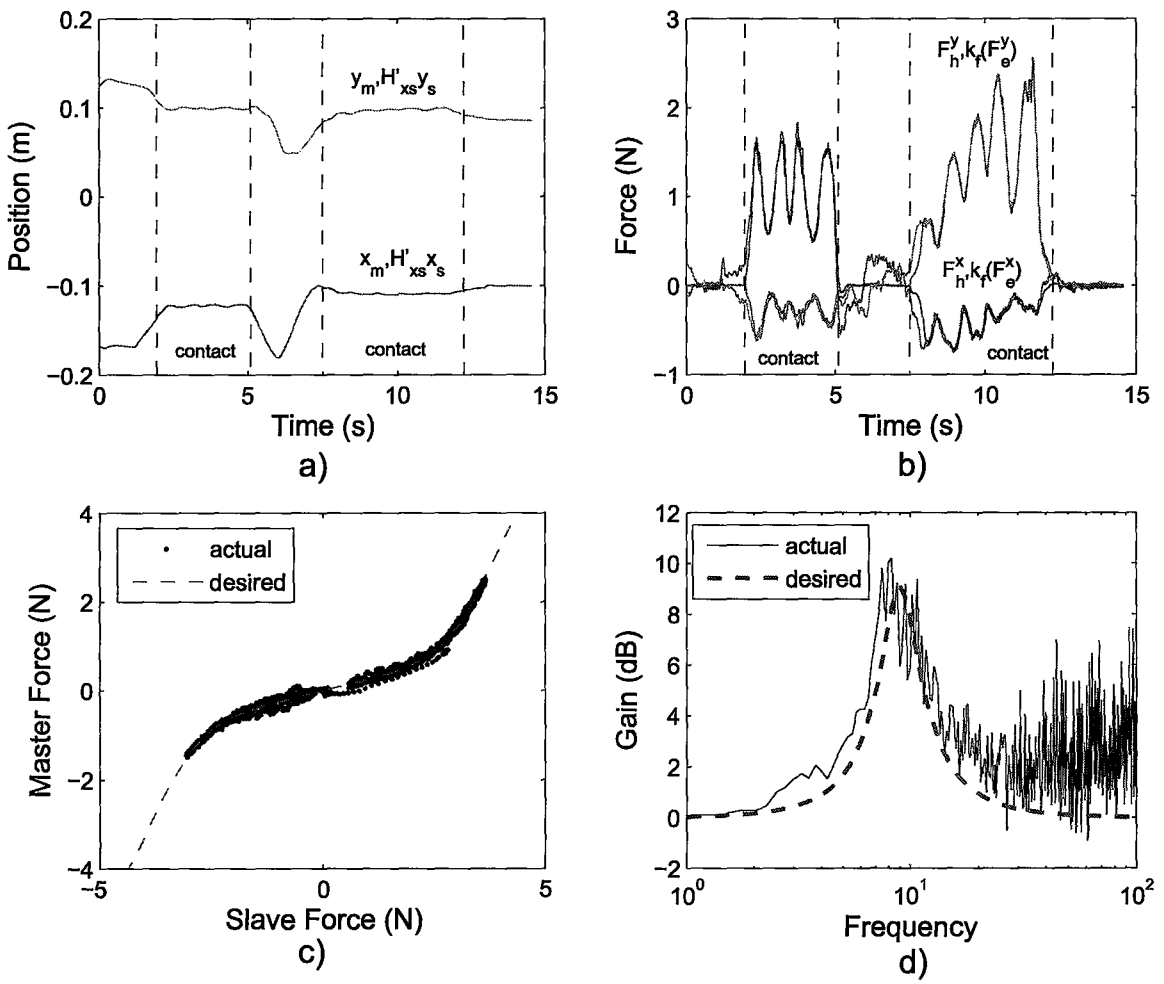

Figure 8.5: Teleoperation experimental results: nonlinear force scaling with filtered position mapping (a) position tracking (b) force tracking (c) nonlinear force scaling; d) filtered position mapping, estimate of $|H'_{xs}(j\omega)|$ obtained using 1024-pt FFT. Note: Position tracking graph a) actually contains four signals.

The resulting experimental position mapping frequency power spectrum is shown in Fig. 8.5(d), from which it is seen the position filtered mapping objective has been achieved. The chosen position filter acts on the slave position hence tremor reduction is realized since master position movements track slave position movements that are amplified by H'_{xs}. It should be noted that at higher frequencies the frequency data is greatly corrupted by noise.

8.3.2 Nonlinear position scaling with filtered force mapping

The second experiment set was conducted using the nonlinear monotonic position scaling (8.11) and a linear force scaling of (8.12) which result in $\kappa_p()^{-1}\kappa_f() \in [0.43, 1]$. The filters used where those defined in (8.13)-(8.15) with parameters $\tau_1 = \frac{1}{\pi}$ s/rad and $\tau_2 = \frac{1}{2\pi}$ s/rad. These filters were also seen in section 6.2.2. The chosen mappings result in a region of high precision with high-pass force filtered mapping. As in the previous case, the operator performed free motion maneuver and made stable contact with the environment. The position and force tracking objectives have been satisfied, as seen in Figs. 8.6(a), (b) and (c).

$$\kappa_p(x) = 0.05\tanh(20x - 1) + 0.75x + 0.05\tanh(1) \tag{8.11}$$

$$\kappa_f(f) = 0.75f \tag{8.12}$$

$$H'_{xm} = H'_{xs} = 1 \tag{8.13}$$

$$H_{fh} = \frac{C}{s+C} \tag{8.14}$$

$$H_{fe} = \frac{C}{s+C} \cdot \frac{\tau_1 s+1}{\tau_2 s+1} \tag{8.15}$$

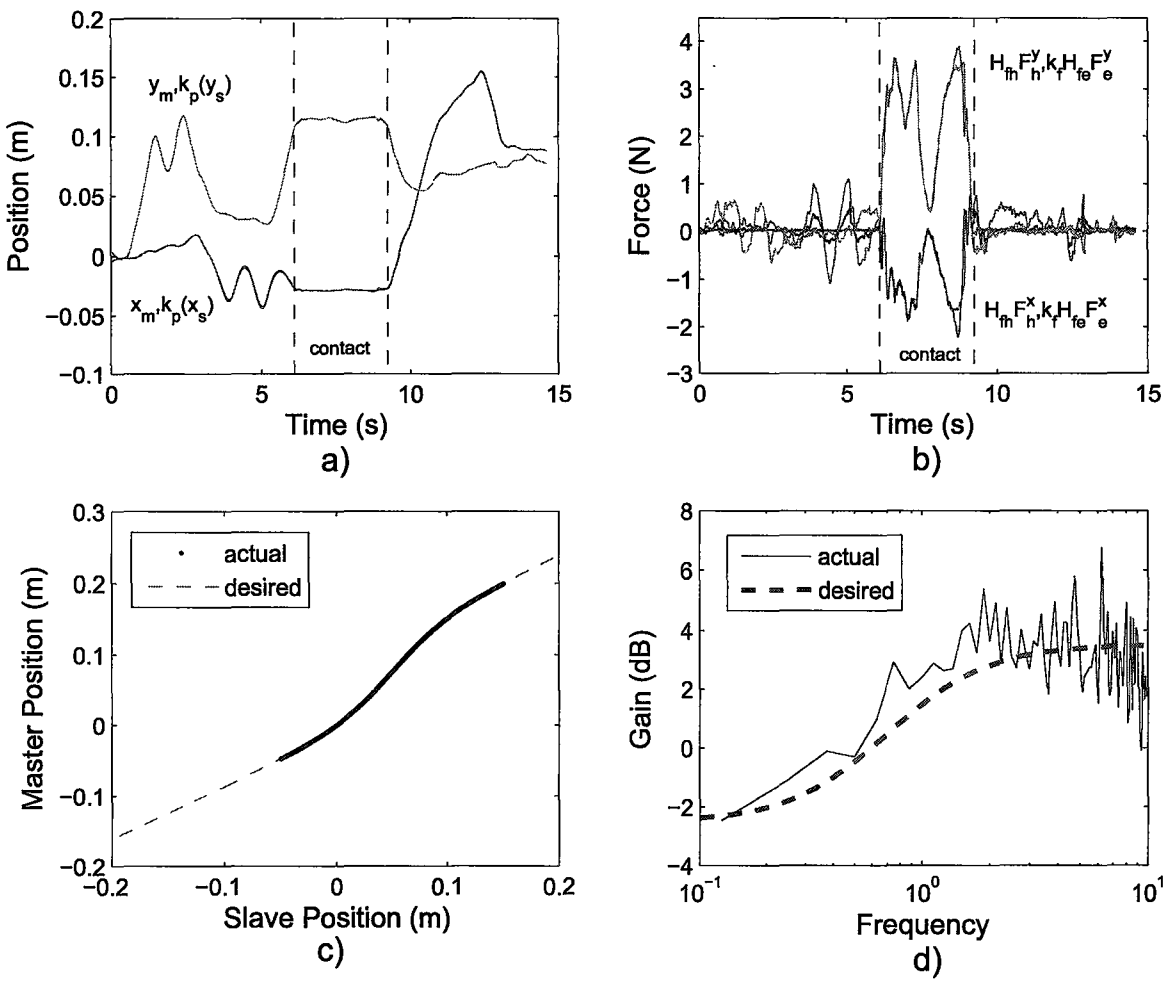

Figure 8.6: Teleoperation experimental results: nonlinear position scaling with filtered force mapping (a) position tracking (b) force tracking (c) nonlinear position scaling; d) filtered force mapping, estimate of $\kappa_f |H_{fe}(j\omega)/H_{fh}(j\omega)|$ obtained using 2048-pt FFT. Note: Position tracking graph a) actually contains four signals.

A separate experiment was also conducted to obtain force frequency mapping data. The operator maintained contact with the soft-environment for 128 seconds producing speed varying oscillatory force signals during that time. An experimental frequency power spectrum of the force mapping was obtained by averaging 32 (16 from x, 16 from y) power spectral estimates of $\kappa_f H_{fe}/H_{fh}$. Each estimate results from the division of a 2048-pt FFT of 8 seconds of master force data by a 2048-pt FFT of 8 seconds of slave force data. The resulting experimental force mapping frequency power spectrum is shown in Fig. 8.6(d), from which it is evident that the filtered force mapping objective has been achieved. It should be noted that the experimental power spectrum at higher frequencies is influenced by both noise and the intervening virtual tool dynamics.

Chapter 9

Conclusions and Future Work

A growing interest in robotic-assisted surgical applications has prompted researchers to explore new teleoperation control methods for enhancing the fidelity of haptic interaction with soft tissues. While previous relevant research has mainly focused on linear scalings of the positions, forces and impedances, in this thesis, nonlinear and LTI filtered mappings of positions and forces were proposed. It is anticipated that the greater flexility offered by such mappings can lead to the design of enhanced teleoperation controllers for soft-tissue telemanipulation. In particular through a set of psychophysics experiments, it was shown that using a nonlinear force mapping can enhance sensitivity in a stiffness discrimination task with and without visual feedback. Also, filtered mappings can be used to reduce hand tremor or sensor noise.

A modified adaptive motion/force teleoperation controller was proposed that can establish the desired monotonic nonlinear scalings and filtered mappings between the master and slave in the presence of dynamic parametric uncertainties.

Using a combination of an off-axis circle criterion for static monotonic nonlinearities and the Nyquist envelop of interval plants, sufficient regions of stability were obtained for a given range of hand/environment parameters which are far less restrictive than those obtained from the passivity and on-axis circle theorems. In the special case of linear filtered mappings of force and position, the exact regions of guaranteed stability were determined. The proposed method was validated in experiments with a 2DOF bilateral teleoperation system.

The major contributions of this thesis are thus summarized as follows:

- Generalized transparency objectives to include non-linear and LTI filtered mappings of position and force.
- Proposing an adaptive controller to achieve the generalized transparency objectives and implementing the controller on a 2DOF teleoperation system.
- Comprehensive robust stability analysis under three different sets of generalized mappings using interval plant systems and stability of Lur'e-Postnikov systems.
- Enhanced stiffness discrimination using a nonlinear force mapping with validating psychophysics experiments.

Future research should consider the effect of time delay on the stability and performance of the system for the application of the proposed generalized mappings to telesurgery. The proposed controller in this thesis can accommodate both nonlinear scalings of force/position, however, stability conditions were only presented for either non-linear force or position scaling. Therefore stability conditions for accommodating both nonlinear scalings should be investigated. In this thesis, it

was assumed that the hand/environment dynamics and non-linear scalings were decoupled on the different axes of motion. Relaxing this restriction can provide more flexibility in the nonlinear mapping design as well as accommodating more complex models of the hand and environment. Control methods for achieving this goal must be developed and their robust stability properties must be investigated. Although the proposed controller can be made to function in force-velocity mode, this is done so at the expense of teleoperation stability since virtual tool damping is removed. A robust modified controller should be designed that allows stable operation with generalized nonlinear velocity mappings. Ultimately a discrete-time implementation is typically performed on a digital computer, therefore precise stability conditions in the discrete-time domain should also be investigated. Although it has been discussed that altering the operator's perception has benefits, potential drawbacks may exist such as degraded performance and unnatural haptic perception. These drawbacks should also be explored. Finally, extensive human factors studies and psychophysics experiments are needed to create more specific and improved design criteria for the proposed generalized mappings proposed in this thesis.

Appendix A

Appendix

A.1 Strict positive realness of $G(s) = \mathcal{Z}_e/(\mathcal{Z}_h + \mathcal{Z}_t)$

Assuming

$$G(s) = \frac{m_1 s^2 + b_1 s + k_1}{m_2 s^2 + b_2 s + k_2} = \frac{\mathcal{Z}_e}{\mathcal{Z}_h + \mathcal{Z}_t} \tag{A.1}$$

where all the coefficients are positive, then $G(s)$ is SPR if

$$\inf_{\omega \in \Re} \mathrm{Re}\left(\frac{-m_1\omega^2 + b_1 j\omega + k_1}{-m_2\omega^2 + b_2 j\omega + k_2}\right) > 0 \tag{A.2}$$

which is equivalent to

$$\frac{\mathrm{Re}[(-m_1\omega^2 + b_1 j\omega + k_1)(-m_2\omega^2 - b_2 j\omega + k_2)]}{(-m_2\omega^2 + b_2 j\omega + k_2)(-m_2\omega^2 - b_2 j\omega + k_2)} > 0, \quad \forall \omega \in \Re \tag{A.3}$$

Inequality (A.3) is satisfied provided

$$m_1 m_2 \nu^2 + (b_1 b_2 - k_1 m_2 - k_2 m_1)\nu + k_1 k_2 > 0, \quad \forall \nu \in \Re^+ \tag{A.4}$$

where $\nu = \omega^2 > 0$. Taking the derivative of (A.4) w.r.t. ν and equating to zero yields

$$\nu = \frac{k_1 m_2 + k_2 m_1 - b_1 b_2}{2 m_1 m_2} \tag{A.5}$$

Plugging (A.5) into (A.4) and performing some algebra yield

$$(k_1 m_2 + k_2 m_1 - b_1 b_2)^2 < 4 k_1 k_2 m_1 m_2 \tag{A.6}$$

taking the square roots of (A.6) and noting (A.4) is positive if $b_1 b_2 - k_1 m_2 - k_2 m_1 > 0$, the limiting inequality assuming $b_1 b_2 - k_1 m_2 - k_2 m_1 < 0$ becomes

$$b_1 b_2 > m_1 k_2 + m_2 k_1 - 2\sqrt{m_1 m_2 k_1 k_2} \tag{A.7}$$

This is equivalent to

$$b_1 b_2 > \left(\sqrt{m_1 k_2} - \sqrt{m_2 k_1}\right)^2 \tag{A.8}$$

A.2 Repeated Measures ANOVA

ANalysis Of VAriance (ANOVA) is a statical technique for testing differences in the means of several groups. It can be viewed as a multiple group extension of an independent groups t-test. The technique tests the null hypothesis, whether all groups have the same mean. This is done by obtaining different estimates of the variances, if these estimates vary greatly the null hypothesis is rejected. ANOVA uses the F-statistic to give the probability of the null hypothesis. For details on ANOVA the reader is referred to chapter 16 of [71].

Repeated Measures ANOVA is a modification of ANOVA where it is assumed each group is a repeated measure of a subject, hence the groups are no longer independent. It can be used to perform a statistical test on a group of subjects, where these subject are exposed to different test conditions. Each test condition contains repeated measures. In such a scenario the differences causes in the test condition is of interest. In Repeated Measures ANOVA the statisical analysis removes the variability between subjects in the variance analysis. Ultimately this method also tests the null hypothesis, whether all repeated measures have the same mean. A chapter length treatment of Repeated Measures ANOVA is found in chapter 18 of [71]. The following example from [71] is given to illustrate the mechanics of this method.

Example: A group of migrane sufferers are tested to see whether the relaxation training they received yields statistically significant results. Each subject gave measures of number of hours of migraines before (weeks 1 and 2) and after training (weeks 3-5).

Table A.1: Example Data

Subject	Week 1	Week 2	Week 3	Week 4	Week 5	Subject Mean
1	21	22	8	6	6	12.6
2	20	19	10	4	9	12.4
3	7	5	5	4	5	5.2
4	25	30	13	12	4	16.8
5	30	33	10	8	6	17.4
6	19	27	8	7	4	13.0
7	26	16	5	2	5	10.8
8	13	4	8	1	5	6.2
9	26	24	14	8	17	17.8
Weekly Means	20.78	20.00	9.00	5.78	6.78	12.47

Grand mean $= 12.47$, Number of measurements $N = 45$

Number of weeks $n_w = 5$, Number of subjects $n_s = 9$

The following calculated quantities are needed:

$$SS_{tot} = \text{var(all data)} \cdot df_{tot} \tag{A.9}$$

$$SS_w = n_s \cdot \text{var}(\mu_w) \cdot df_w \tag{A.10}$$

$$SS_{sub} = n_w \cdot \text{var}(\mu_{sub}) \cdot df_{sub} \tag{A.11}$$

$$SS_{error} = SS_{tot} - SS_w - SS_{sub} \tag{A.12}$$

where var(all data) is the variance of all data with degrees of freedom $df_{tot} = N-1$, $\text{var}(\mu_w)$ is the variance of the week means with $df_w = n_w - 1$, $\text{var}(\mu_{sub})$ is the variance of the subject means with $df_{sub} = n_s - 1$. The subtraction of SS_{sub} in (A.12) is unique to repeated measures ANOVA and in effect removes subject variability. Regular ANOVA does not require SS_{sub} and df_{sub}.

Using the calculated SS values in (A.9)-(A.12) the following summary table is used to find the needed F value for obtaining the null hypothesis probability.

Table A.2: Example Summary Table

Source	df	SS	MS	F
Subjects	8	833.6		
Weeks	4	1934.5	483.63	21.46
Error	32	721.1	22.534	
Total	44	3489.2		

$$MS_{\sim} = \frac{SS_{\sim}}{df_{\sim}} \tag{A.13}$$

$$F(df_{weeks}, df_{error}) = \frac{MS_{weeks}}{MS_{error}} \tag{A.14}$$

Here MS_{error} and MS_{weeks} are variance estimates. The value $F(4, 32) = 21.46$ indicates the variances estimates differ greatly implying the weekly means are expected to be different. The associated probability for a null hypothesis is $p < 0.001$, which can be obtained by using F-statistic formulas or looking in F-statistic tables. This example concludes statistically significant results.

Bibliography

[1] K. Hashtrudi-zaad and S. Salcudean, "Analysis of control architectures for teleoperation systems with impedance/admittance master and slave manipulators," *Int. J. Robot. Res.*, vol. 20, no. 6, pp. 419–445, 2001.

[2] N. Tan and D. P. Atherton, "Frequency response of uncertain systems: A 2q-convex parpolygonal approach," *IEE Proc. Control Theory Appl.*, vol. 147, no. 5, pp. 547–555, 2000.

[3] C. V. Hollot and R. Temp, "On the nyquist envelope of an interval plant family," *IEEE Tran. Automat. Cont.*, vol. 39, no. 2, pp. 391–396, 1994.

[4] G. Gescheider, *Psychophysics The Fundamentals*. Mahwah NJ: Lawrence Erlbaum Associates, 1997.

[5] K. S. Hale and K. M. Stanney, "Deriving haptic guidelines from human physiological, psychophysical, and neurological foundations," *IEEE Comp Graphics and Applications*, vol. 24, no. 2, pp. 33–39, 2004.

[6] P. F. Hokayem and M. W. Spong, "Bilateral teleoperation: an historical survey," *Automatica*, pp. 2035–2057, 2006.

[7] S. Salcudean, *Control for Teleoperation and Haptic Interfaces.* Control Problems in Robotics and Automation; B. Siciliano and K.P. Valavanis (Eds.), Springer, 1997.

[8] P. Dario, B. Hannaford, and A. Menciassi, "Smart surgical tools and augmenting devices," *IEEE trans on Robotics and Automation*, vol. 19, no. 5, pp. 782–792, 2003.

[9] B. Hannaford, "A design framework for teleoperators with kinesthetic feedback," *IEEE Trans. Robot. Automat.*, vol. 5, pp. 426–434, August 1989.

[10] D. Lawrence, "Stability and transparency in bilateral teleoperation," *IEEE Trans. Robot. Automat.*, vol. 9, pp. 624–637, October 1993.

[11] G. Raju, G. Verghese, and T. Sheridan, "Design issues in 2-port network models of bilateral remote teleoperation," in *Proc. IEEE Int. Conf. Robot. Automat.*, pp. 1317–1321, 1989.

[12] H. Kazerooni, T. Tsay, and K. Hollerbach, "A controller design framework for telerobotic systems," *IEEE Trans. Contr. Syst. Technol.*, vol. 1, pp. 50–62, March 1993.

[13] G. Leung, B. Francis, and J. Apkarian, "Bilateral controller for teleoperators with time delay via mu-synthesis," *IEEE Trans. Robot. Automat.*, vol. 11, no. 1, pp. 105–116, 1995.

[14] Y. Yokokohji and T. Yoshikawa, "Bilateral control of master-slave manipulators for ideal kinesthetic coupling-formulation and experiment," *IEEE Trans. Robot. Automat.*, vol. 10, pp. 605–620, October 1994.

[15] G. Niemeyer and J.-J. Slotine, "Stable adpative teleoperation," *IEEE J. Oceanic Eng.*, vol. 16, no. 1, pp. 152–162, 1991.

[16] Y. Yokokohji, T. Imaida, and T. Yoshikawa, "Bilateral control with energy balance monitoring under time-varying communication delay," in *Proc. IEEE Int. Conf. Robot. Automat.*, pp. 2684–2689, 2000.

[17] K. Hashtrudi-Zaad and S. Salcudean, "Transparency in time-delayed systems and the effect of local force feedback for transparent teleoperation," *IEEE Trans. Robot. Automat.*, vol. 18, no. 1, pp. 108–114, 2002.

[18] S. Sirouspour and A. Shahdi, "Discrete-time linear quadratic gaussian control for teleoperation under communication time delay," *The Int. Journal of Robotics Research*, vol. 25, pp. 187–202, February 2006.

[19] S. Sirouspour and A. Shahdi, "Model predictive control for transparent teleoperation under communication time delay," *IEEE trans on Robotics*, pp. 1131–1145, 2006.

[20] A. Shahdi and S. Sirouspour, "Adaptive/robust control for enhanced teleoperation under communication time delay," in *Proceedings of IEEE conf. on Intelligent Robots and Systems*, Oct 2007.

[21] A. Shahdi and S. Sirouspour, "A multi-model decentralized controller for teleoperation with time delay," in *Proceedings of IEEE conf. on Intelligent Robots and Systems*, Oct 2007.

[22] J. Colgate, "Robust impedance shaping telemanipulation," *IEEE Trans. Robot. Automat.*, vol. 9, pp. 374–384, August 1993.

[23] S. Sirouspour, "Modeling and control of cooperative teleoperation systems," *IEEE Transactions on Robotics*, vol. 21, pp. 1220–1225, December 2005.

[24] W. Zhu and S. Salcudean, "Stability guaranteed teleoperation: an adaptive motion/force control approach," *IEEE Trans. Automat. Contr.*, vol. 45, pp. 1951–1969, November 2000.

[25] J.-E. Slotine and W. Li, *Applied Nonlinear Control*. New Jersey: Prentice-Hall Inc., 1991.

[26] L. Sciavicco and B. Siciliano, *Modeling and Control of Robot Manipulators, Second Edition*. Springer-Verlag, 2000.

[27] J. O. Perreault and C. G. L. Cao, "Effects of vision and friction on haptic perception," *Human Factors*, vol. 48, no. 3, pp. 574–586, 2006.

[28] M. Tavakoli, R. V. Patel, and M. Moallem, "Haptic interaction in robot-assisted endoscopic surgery: a sensorized end-effector," *Int. J. Medical Robotics and CAS*, vol. 1, no. 2, pp. 53–63, 2005.

[29] B. Deml, T. Ortmaier, and U. Seibold, "The touch and feel in minimally invasive surgery," in *Proceedings of IEEE Int. Workshop Haptic Audio Visual Envir. and Applic.*, pp. 33–38, Oct 2005.

[30] L. Zamorano, Q. Li, S. Jain, and G. Kaur, "Robotics in neurosurgery: state of the art and future technological challenges," *Int. J. Medical Robotics and CAS*, vol. 1, no. 1, pp. 7–22, 2004.

[31] A. Rossi, A. Trevisani, and V. Zanotto, "A telerobotic haptic system for minimally invasive stereotactic neurosurgery," *Int. J. Medical Robotics and CAS*, vol. 1, no. 2, pp. 64–75, 2005.

[32] C. N. Riviere, R. S. Rader, and P. K. Khosla, "Characteristics of hand motion of eye surgeons," in *Proc. Int. Conf. IEEE/EMBS*, pp. 1690–1693, 1997.

[33] C. N. Riviere and N. V. Thakor, "Suppressing pathological tremor during dextrous teleoperation," in *Proceedings of IEEE Engineering in Medicine and Biology*, pp. 1195–1196, Sept 1995.

[34] A. M. Okamura, "Methods for haptic feedback in teleoperated robot-assisted surgery," *Industrial Robot: An international journal*, vol. 31, no. 6, pp. 499–508, 2004.

[35] M. Çavuşoğlu, A. Sherman, and F. Tendick, "Design of bilateral teleoperation controllers for haptic exploration and telemanipulation of soft environments," *IEEE Trans. Robot. Automat.*, vol. 18, no. 4, pp. 641–647, 2002.

[36] G. D. Gersem, H. V. Brussel, and F. Tendick, "Reliable and enhanced stiffness perception in soft-tissue telemanipulation," *Int. J. Robot. Research*, vol. 24, no. 10, pp. 805–822, 2005.

[37] X. Wang, P. X. Liu, B. Chebbi, D. Wang, and M. Meng, "Design of bilateral teleoperators for soft environments with adaptive environmental impedance estimation," in *Proc. IEEE Int. Conf. Robotics Automation*, pp. 1127–1132, 2005.

[38] R. H. Lamotte, "Softness discrimination with a tool," *Journal of Neurophysiology*, pp. 1777–1786, 2000.

[39] M. K. O'malley and M. Goldfarb, "Comparison of human size identification and discrimination performance in real and simulated environments," in *Proceedings of IEEE Symp on Haptic interfaces for Virt. Envir. and Teleoperator systs.*, pp. 10–17, Mar 2002.

[40] M. K. O'malley and M. Goldfarb, "The implications of surface stiffness for size identification and perceived surface hardness in haptic interfaces," in *Proceedings of IEEE conf. on Robotics and Automation*, pp. 1255–1260, May 2002.

[41] M. K. O'malley and M. Goldfarb, "The effect of force saturation on the haptic perception of detail," *IEEE/ASME trans on mechatronics*, pp. 280–288, 2002.

[42] M. K. O'malley and M. Goldfarb, "The effect of virtual surface stiffness on the haptic perception of detail," *IEEE/ASME trans on mechatronics*, pp. 448–454, 2004.

[43] G. D. Gersem, H. V. Brussel, and F. Tendick, "A new optimization function for force feedback in teleoperation," in *Proc. Int. Conf. Computer Assisted Radiology and Surgery*, p. 1354, 2003.

[44] W. Wu, C. Basdogan, and M. A. Srinivasan, "Visual, haptic, and bimodal perception of size and stiffness in virtual environments," in *Proc. ASME Dynamic Systems and Control Division*, pp. 19–26, 1999.

[45] M. A. Srinivasan, G. L. Beauregard, and D. L. Brock, "The impact of visual information on the haptic perception of stiffness in virtual environments," in *Proc. ASME Dynamic Systems and Control Division*, pp. 555–559, 1996.

[46] F. Barbagli, K. Salisbury, C. Ho, C. Spence, and H. Tan, "Haptic discrimination of force direction and the influence of visual information," *ACM Trans. Applied Perception*, vol. 3, no. 2, pp. 125–135, 2006.

[47] V. L. Kharitonov, "Asymptotic stability of an equilibrium position of a family of systems of linear differential equations," *Differential Equations*, vol. 14, pp. 1483–1485, 1979.

[48] S. P. Bhattacharyya, H. Chapellat, and L. H. Keel, *Robust Control: the parametric approach*. Prentice Hall, 1995.

[49] B. R. Barmish, "A generalization of kharitonov four-polynomial concept for robust stability problems with linearly dependent coefficient perturbations," *IEEE Trans. Automatic Control*, vol. 34, no. 2, pp. 157–165, 1989.

[50] S. Boyd and L. Vandenberghe, *Convex Optimization*. Cambridge: Cambridge University Press, 2004.

[51] A. Barlett, C. V. Hollot, and H. Lin, "Root location of an entire polytope of polynomials: it sufficies to check the edges," *Math. Control, Signals. Syst.*, no. 1, pp. 61–71, 1988.

[52] N. Tan, "Robust phase margin, robust gain margin and nyquist envelope of an interval plant family," *Computers and Electrical Engineering*, vol. 30, no. 2, pp. 153–165, 2004.

[53] A. I. Lur'e and V. N. Postnikov, "On the theory of stability of control systems," *Applied mathematics and mechanics*, vol. 8, no. 3, 1944.

[54] A. van der Schaft, *L2-Gain and Passivity Techniques in Nonlinear Control 2nd Ed.* London: Springer-Verlag, 2000.

[55] M. Vidyasagar, *Nonlinear Systems Analysis*. Englewood Cliffs NJ: Prentice Hall, 1993.

[56] G. Zames, "On the input-output stability of time-varying nonlinear feedback systems-part i: conditions derived using concepts of loop gain, conicity, and positivity," *IEEE Trans. Automatic Control*, no. 2, pp. 228–238, 1966.

[57] G. Zames, "On the input-output stability of time-varying nonlinear feedback systems-part ii: conditions involving circles in the frequency plane and sector nonlinearites," *IEEE Trans. Automatic Control*, no. 3, pp. 465–476, 1966.

[58] Y.-S. Cho and K. S. Narendra, "An off-axis circle criterion for the stability of feedback systems with a monotonic nonlinearity," *IEEE Tran. Automat. Cont.*, vol. 13, no. 4, pp. 413–416, 1968.

[59] M. S. Ghausi and J. J. Kelly, *Introduction to Distributed-Parameter Networks with Application to Integrated Circuits*. New York: Holt, Rinehart and Winston Inc., 1968.

[60] V. V. Kulkarni and M. G. Safonov, "Incremental positivity nonpreservation by stability multipliers," *IEEE Trans. Automatic Control*, vol. 47, no. 1, 2002.

[61] K. S. Narendra and Y. S. Cho, "Stability of feedback systems containing a single odd monotonic nonlinearity," *IEEE Trans Automatic Control*, vol. 12, no. 4, pp. 448–450, 1967.

[62] D. Materassi, M. Salapaka, and B. Basso, "A less conservative circle criterion," in *Proceedings of the American Control Conf.*, pp. 824–827, June 2006.

[63] T. Mori, T. Nishimura, Y. Kuroe, and H. Kokame, "Off-axis circle criteria for lur'e systems with interval plants," in *Proceedings of IEEE conf. on Decision and Control*, pp. 585–586, Dec 1994.

[64] N. Tan and D. P. Atherton, "New approach to assessing the effects of parametric variations in feedback loops," *IEE Proc. Control Theory Appl.*, vol. 150, no. 2, pp. 101–111, 2003.

[65] S. S. Stevens, "On the pyschophysical law," *Psychological Review*, pp. 153–181, 1957.

[66] H. Levitt, "Transformed up-down methods in psychoacoustics," *J. Acoustical Society of America*, vol. 49, pp. 467–477, 1970.

[67] G. Békésy, "A new audiometer," *Acta Oto-laryngology*, pp. 411–422, 1947.

[68] L. G. Brown, "Additional rules for the transformed up-down method in psychophysics," *Perception and Psychophysics*, pp. 959–962, 1996.

[69] C. Kaernbach, "Simple adaptive testing with the weighted up-down method," *Perception and Psychophysics*, vol. 49, pp. 227–229, 1991.

[70] T. H. Rammsayer, "An experimental comparison of the weighted up-down method and transformed up-down method," *Bulletin of the Psychonomic Society*, pp. 425–427, 1992.

[71] D. Howell, *Fundamental Statistics for the Behavioral Sciences 5th Ed.* Belmont CA: Brooks/Cole, 2004.